Frictional Behaviour of Elastomer Seals

Eduardo Francisco Yanes Nunez

Submitted in partial fulfilment of the requirements of the Degree of Doctor of Philosophy

The School of Engineering and Materials Science

Queen Mary University of London

Mile End Road

London E1 4NS

January 2022

Declaration

I, Eduardo Francisco Yanes Nunez, confirm that the research included within this thesis is my own work or that where it has been carried out in collaboration with, or supported by others, that this is duly acknowledged below, and my contribution indicated. Previously published material is also acknowledged below.

I attest that I have exercised reasonable care to ensure that the work is original and does not to the best of my knowledge break any UK law, infringe any third party's copyright or other Intellectual Property Right, or contain any confidential material.

I accept that the College has the right to use plagiarism detection software to check the electronic version of the thesis.

I confirm that this thesis has not been previously submitted for the award of a degree by this or any other university.

Signature: 

Date: 31st January 2022

Abstract

Previous investigations of rubber friction have focused around the automotive/motorsport industry, where contact pressure levels are typically less than 1 MPa and the sliding velocity is a key variable. The current project endeavours to better understand what controls the level of rubber friction at higher pressure levels (above 10 MPa) and at higher temperatures (>100°C). The thesis outlines the design of a new rig. An explanation of how the apparatus was used to measure the sliding friction is described.

The rubber materials characterised in this report were all commercially available compounds, typical of those used in the oilfield. The rubber compounds were characterised for their mechanical and thermal properties to help characterise and model their behaviour. The coefficient of friction was derived by dividing the measured friction force by the normal force, which was determined using a Finite Element Analysis (FEA) modelling approach. Testing was carried out at three different temperatures, with two types of materials in two different liquid environments. From these tests, the frictional force at the interface between the metal surface and the rubber was characterised at different sliding speeds. Different types of surface analysis techniques were used to characterise the sliding surface. The surface analysis was then related through the sliding velocity to a characteristic frequency of deformation during sliding of the rubber seals. Using independently measured dynamical mechanical analysis (DMA) data, the frictional behaviour was related to the viscoelastic properties of the rubber. Using the experimental friction results and characterisation techniques, different friction models from the literature were tested against the measured data sets to observe which were best suited to this type of application. The final chapter outlines the best way to model rubber surface interactions in FEA under these demanding conditions and compares the results of this investigation with the recognised industry standards.

Details of collaborations:

This entire body of research was done under the sponsorship of Schlumberger Ltd. All tested materials and developed equipment were also obtained under Schlumberger Ltd. Sponsorship.

Details of publications:

Yanes, E., Pugno, N.M., Ramier, J., Berryhill, B. and Busfield, J.J., 2021. Characterising the friction coefficient between rubber O-rings and a rigid surface under extreme pressures. *Polymer Testing*, *104*, p.107378.

Details of conference proceedings:

E Francisco Yanes Nunez, N Pugno, JJC Busfield, Queen Mary University, J Ramier, Schlumberger Cambridge Research Ltd, UK., 2020. Characterisation of Friction behaviour for dynamic O-ring seals during cyclic testing under extreme pressure and temperature conditions. In *25th International Conference on Fluid Sealing*, Manchester, UK, March 4th–5th, 2020. Ed. A. Bickley. BHR Group, Bedfordshire, UK.

Nunez, E.Y., Busfield, J.J.C., Pugno, N., Manson, R., Chen, H.L. and Ramier, J., 2019. Application of rubber friction to FEA models of rubber sealing. In *Constitutive Models for Rubber XI* (pp. 491-494). CRC Press.

Details of conference presentations:

Characterisation of Friction Behaviour of Rubber. PhD seminar on Rubber Chemistry and Technology. Lodz, Poland. April 23-25, 2018.

Characterisation of Friction Behaviour of Rubber. 194th Technical Meeting of the Rubber Division, ACS. Louisville, Kentucky. October 9-11, 2018.

Characterisation of Friction behaviour for dynamic O-ring seals during cyclic testing under extreme pressure and temperature conditions. Student poster (1st prize). International Rubber Conference 2019. London, United Kingdom. September 3-5, 2019.

Characterisation of Friction behaviour for dynamic O-ring seals during cyclic testing under extreme pressure and temperature conditions. In *25th International Conference on Fluid Sealing*, Manchester, UK, March 4th–5th, 2020.

Acknowledgements

-*Who are those dressed as harlequins?*

-*…those are the PhD graduates mom.*

-*I'd sure like to see you in one of those…*

I would like to thank Prof. James Busfield for taking a tremendous chance with an international student without any real scientific writing experience, for his guidance during my entire PhD, and for loads of patience with my delivery timing. The first day I came to Queen Mary I asked another PhD student "what is the boss like?" to which he answered, "he is the best bloke I know". He was right.

I express a very special thanks to my colleague Travis, without his help and guidance, this thesis would have not been finished on time. He is also a good friend, who opened the doors of his house for me to meet his wonderful family. I will be forever grateful for this last part specially.

The entire Schlumberger team from both Houston (Ron, Hoi Ling, Ben and Ken) and the Cambridge Research Centre (Gary, Harry, Louise, Mandy). Since my first day, I had complete support from them. A very special thanks amongst the team has to go to Dr. Julien Ramier. Julien made me a part of the Cambridge team, even when I was not involved with his research group in any way, he provided support and guidance through the last two years of my project.

To all my soft matter group friends. Richard who taught me the ropes as I started. Anureet, who I leave in charge of the group as I take my leave, I could always trust her with anything I needed.

To my family. My mother and brother who were always very proud of my academic achievements, they have always pushed me forward. Lastly, but certainly not least, to the only family I chose:

-*You know that if I do this, we will put our life on hold for 3-4 years.*

-*Yes, as long as it is what you want, I'm happy.*

My wife, my proudest achievement and my favourite person. Thank you, all of this is better because of you.

Contents

List of Figures

List of Tables

List of Symbols and Abbreviations

A_{D}	constant in the Doolittle equation
A_{H}	Hertz area of contact
A_{o}	apparent contact area
a_{T}	shift factor in time-temperature superposition
B_{D}	constant in the Doolittle equation
c_1	constant in the WLF equation
c_2	constant in the WLF equation
c_{A}	a velocity-dependent coefficient
$C_{\mathrm{HDC}}(\lambda)$	height difference correlation function
C_{ijk}	coefficients in a Rivlin SEF expansion
c_{m}	constant in the Hertz equation
cm	centimetre
$C(q)$	power spectrum density of a surface
$C(\lambda)$	height difference correlation function
D	fractal dimension
$\mathrm{d}Q$	differential amount of heat energy
$\mathrm{d}S$	differential amount of entropy
$\mathrm{d}U$	differential amount of internal energy
$\mathrm{d}W$	differential amount of work energy
E	elastic (Young's) modulus
E_0	static modulus at a crack tip in rubber
E_{w}	complex modulus at a crack tip in rubber
E^*	the complex modulus of stiffness for a viscoelastic material in tension
$E^{'}$	in-phase (or purely elastic) stiffness component of a viscoelastic material in tension
$E^{''}$	out-of-phase stiffness component of a viscoelastic material in tension
E_∞	high frequency modulus at a crack tip in rubber
f	frequency
F_{A}	adhesion friction
F_{a}	adhesional friction force
F_{h}	hysteretic friction force
F_{o}	normal force
F_{N}	normal force
f_{V}	fractional free volume
$G^{'}$	in-phase (or purely elastic) stiffness component of a viscoelastic material in shear
$G^{''}$	out-of-phase stiffness component of a viscoelastic material in shear
H	Hurst exponent, a measure of surface irregularity
Hz	Hertz
I_1	first invariant of the strain tensor
I_2	second invariant of the strain tensor
I_3	third invariant of the strain tensor
$h(x)$	sinusoidal amplitude in a PSD
i	numerical index
j	numerical index
K	Kelvin
k	Boltzmann's constant
k	numerical index
kg	kilogram
l	minimum contact length
mm	millimetre
MPa	Megapascal
N	number of links in a polymer chain
n	model order in a strain energy function
n	a material-dependent exponent
nm	nanometre
q	wavenumber
q_0	roll-off wavenumber
q_1	cut-off wavenumber
P	pressure
$P(q)$	the ratio of real contact area to apparent contact area
Ra	root mean square average surface finish
Rq	root mean square

$r(0)$	crack tip radius for a crack sliding at nearly zero velocity
$r(V)$	crack tip radius for a crack sliding at velocity V
S	entropy
s	second
$S(q)$	correction factor in Persson's friction model for the elastic constant
$S(q)$	correction factor in Persson's friction model for the elastic constant
$S(\omega)$	power spectrum density based on height difference correlation
T	temperature
T_{g}	glass transition, or glass transition temperature
t_{i}	tension in direction i, with $\mathrm{i} = 1,2,3$
T_{ref}	a reference temperature for horizonal shift in the WLF equation
V	volume, or sliding velocity
V_{c}	critical velocity at which adhesive friction is maximum
V_{o}	volume
W	work energy
x	horizontal position along a surface profile
z	height of a surface profile
$\mathrm{z_p}$	a descriptor of the layer of rubber that deforms during a sliding interaction
ΔS	change in entropy
ε	strain
$\dot{\varepsilon}$	strain
γ	stretch or extension ratio (a measure of strain), or an empirical constant
$\dot{\gamma}_{\mathrm{eq}}$	slip rate in a contact interaction in FEA
γ_{o}	shear strain amplitude
$\gamma(t)$	shear strain as a function of time
δ	the angle between in-phase and out-of-phase moduli for a viscoelastic material
λ	horizontal distance between peaks along a surface profile, or wavelength, or stretch
λ_{i}	stretch in coordinate direction i, with $\mathrm{i} = 1,2,3$
μ	coefficient of friction
μ_{A}	adhesional component of friction
μ_{adh}	adhesional component of friction
μ_{adhesion}	the adhesional component of friction in the Unified Theory of Rubber Friction
μ_{cohesion}	the cohesive component of friction in the Unified Theory of Rubber Friction
$\mu_{\mathrm{deformation}}$	the hysteretic component of friction in the Unified Theory of Rubber Friction
μ_{hyst}	the hysteretic component of friction
μm	micrometre
μ_{s}	static coefficient of friction
μ_{k}	kinetic coefficient of friction
μ_{total}	the total friction in the Unified Theory of Rubber Friction
μ_{viscous}	the viscous (lubricating) component of friction in the Unified Theory of Rubber Friction
ν	Poisson's ratio
$\xi_{\parallel}$	horizontal cut-off length of a surface
$\xi_{\perp}$	vertical cut-off length of a surface
σ	stress
σ_0	apparent contact pressure
τ	shear stress
τ_{crit}	critical shear stress at which sliding contact occurs in FEA
τ_0	shear stress amplitude in a sinusoidal shear loading
τ_{s}	interfacial shear strength
$\tau_{\mathrm{s,0}}$	interfacial shear strength at very low velocities
ω	sinusoidal excitation frequency
℃	degrees Celsius
<∘>	average square operator

Abbreviations:

CoF	coefficient of friction
DMA	dynamic mechanical analysis
DoE	design of experiments

DSC	dynamic scanning calorimetry
TGA	thermogravimetric analysis
FEA	finite element analysis
FKM	vinylidene hexafluoropropylene rubber
HDC	height difference correlation
HNBR	hydrogenated nitrile butadiene rubber
PSD	power spectrum density
RMS	root mean square
Ra	Surface roughness (average)
SEF	strain energy function
WLF	Williams-Landel-Ferry

1. Introduction

Oilfield industry elastomers are well researched in terms of their stress response, swelling resistance, crack growth behaviour and temperature specifications. These variables are looked at when designing sealing components for field operations and each failure of a sealing element carries a heavy monetary and environmental cost.

One variable that has typically been left out is the frictional behaviour of these seals, how they interact with different grades of steel at different velocities, temperatures and pressure levels is not well known, simulations and designs can fail because of this lack of knowledge.

Previous research into the friction behaviour of elastomers has typically focused around the automobile industry where surfaces are rough, and pressure levels are typically kept below 1 MPa. Given that rubber seals in the oilfield can undergo pressures up to 100 MPa, temperatures above 150°C and are not visible for most of the time, it is imperative to understand the tangential behaviour of seals during setting and working conditions.

The current research project is aimed at creating a way to test the frictional behaviour of elastomers typically used in the oilfield industry. The process of friction analysis, testing and modelling is looked at through five different chapters.

Chapter 2 is a look at the theory of polymer science and basis for elastomer formation, the different types of elastomers and how they are made. It moves on to analyse why the properties of elastomers are so unique, both in terms of mechanical and chemical properties. For this research, to be able to shift these mechanical properties with variables such as temperature and frequency is of great importance, so the time-temperature superposition is explained and performed. A brief overview of rubber as sealing materials is then shown, with particular focus on why friction studies are key. The finite element analysis (FEA) technique is reviewed to better understand how to model these mechanical properties. Afterwards, the frictional behaviour of rubber and its research from the past 80 years are analysed to set the groundwork to design a proper friction testing protocol. Lastly, tribological analysis is also covered to step away from the "universal" frictional parameters attributed to rubber.

Chapter 3 goes over the characterisation process for all materials tested for frictional behaviour. Uniaxial tension and compression results are shown for all materials at the desired friction testing temperatures, and a table with strain energy density function coefficients is derived from this. Dynamic Mechanical Analysis (DMA) results for a single elastomer is performed, and the mastercurve at a reference temperature is then shown (and later used for the frictional analysis). Differential Scanning Calorimetry (DSC) results are shown, mainly to verify the glass transition temperature. Finally, profilometry analysis is done in two different ways to carefully measure the testing surfaces.

Chapter 4 develops the initial testing methods (and explores the testing failures) to study rubber friction, the challenges of high temperature and high-pressure testing environments, and the reasoning for developing the proposed novel test rig. The novel rig schematic is developed and the outputs from it are explained and then verified for literature compliance. In the final section of chapter 4, there is a small section mentioning the possible problems that can occur with this novel testing method and how to detect them. Chapter 4 has been partially published recently in the journal of Polymer Testing.

Chapter 5 looks at the experimental results and analyses major contributing factors to rubber friction including: pressure, temperature and velocity (related to surface roughness). The analysis of each factor is looked at separately to better understand it, and finally they are compiled to observe trends and the validity of theoretical models. A simple model is then derived for all elastomers at different testing conditions, and the required constants are output in tables.

Chapter 6 is a study case of the importance of frictional analysis in to develop more accurate models that can be used for FEA simulations. Industry standard models are compared to experimentally determined ones, that are later tested for three different outputs: contact pressure, which is key when it comes to leak prevention in seals; strain energy density, which is related to crack growth and failure in elastomers; shape during seal setting, which can cause excessive deformation at points and seal failure. Finally, guidelines for better elastomer FEA simulations are given, to replicate the results of the experiments and to help improve industrial design practice.

Chapter 7 will conclude the work by exploring the lessons learned. First, an analysis of the validity of current friction theories and their limitations, the necessity for empirical data and what physical properties can provide. Secondly, the novel rig design is explored in terms of its advantages and disadvantages. The safety, environmental and practical values are highlighted, and then advice for a better, more efficient method are provided. Third, a small modification to frictional adhesion contribution is presented. Finally, the changes during FEA simulation for elastomers with different friction models are summarised. Some industry guidance is given, as to how close to the “true” model a simulation has to be in order to provide reliable results.

2. Rubber Theory

2.1 The Molecular Structure of Polymers

The term polymer is used to describe a class of macromolecules that consist of repeated chemical units of the same type. These units are joined end to end in order to form a chain molecule[1]. The most basic of these molecules is the one with a single repeating chemical unit, called a homopolymer. Figure 2.1 presents a diagram of what would be a polymer chain using the homopolymer "A" connected by hydrogen bonds. The simplest of polymers is when the homopolymer methylene is chained in order to form polyethylene. Polyethylene is very flexible; the chains are joined by what are called backbone bonds. These are single bonds with a joint angle close to 112°; the energy required for rotation of the molecule is very little. Other polymer backbones are not so simple, and the rotation of the chain is limited by more complex side groups, double bonding between monomers or side chains.

Figure 2.1: Polymer chain placeholder. From[1]

Some notations for polymer description are shown in figure 2.2 with polyethylene as an example. Modern polymers are rarely comprised of one repeating unit, when there are two or more units, these molecules are called copolymers. Copolymers can be classified into two cases. The first one of these is through statistical coupling of two different monomeric units, governed by the probability of attachment of the two different units, generating **statistical copolymers**. The other case is the one for block copolymers, where long sequences of one monomer are prepared and then mixed with the other monomer sequence. Figure 2.3 presents two sketches for how an ethylene-propylene copolymer may be organised.

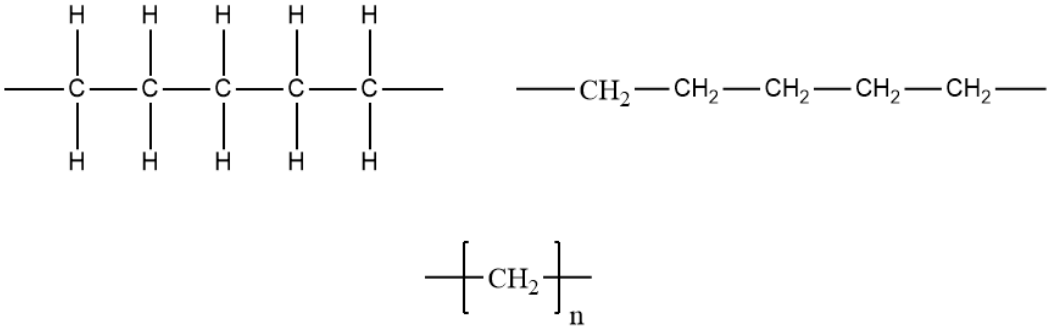

Figure 2.2: Different polymer notations for the same polyethylene molecule.

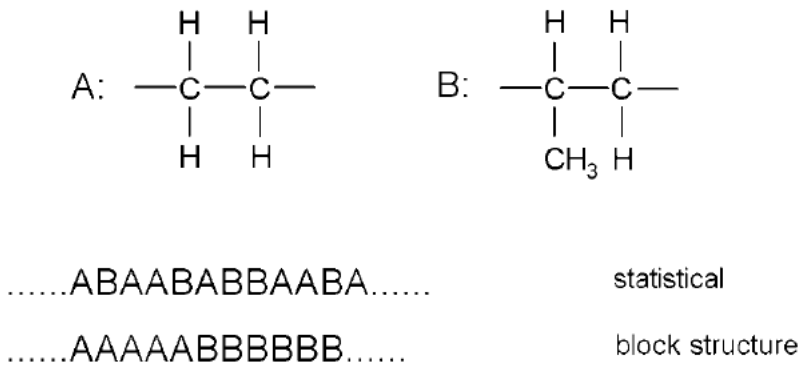

Figure 2.3: Illustration of different types of organisations of copolymers. Taken from [2]

When polymer chains are linked to each other (crosslinking) forming a three-dimensional network, their properties change. Rubbers, also known as elastomers, could be defined as a very large macromolecule whose dimensions reach the macroscopic scale. Rubber was originally a term used to describe materials that were derived from the latex that comes from the *Hevea Brasiliensis* tree[3]. The sap from the tree is a polymer dissolved in a water-based liquid, also known as a latex. This sap is collected and dried to generate blocks of natural rubber (NR).

Not all polymers can be reconfigured to form three-dimensional networks in order to create elastomer structures. To crosslink polymer chains, the crosslinking bond must be more stable than the one in the polymer chain. In the case for polyethylene there are no unsaturated carbons and no side groups that could be used as crosslinking points. This is where copolymerisation becomes relevant. Adding an extra monomer that has non-saturated carbons can be used as a crosslinking point. Figure 2.4 uses ethylene propylene rubber (EPM) as an example. An ethylene-propylene backbone is fully saturated in all of its carbons, not allowing for crosslinking, when diene monomer ethylidene norbornene (ENB) is introduced into the chain, the double bond in the unit becomes the crosslinking point. Because of the addition of another monomer, EPM rubbers are considered terpolymers (containing three monomer units).

This is just one example of how can rubber materials can be created. In the previous case, synthetic materials were used to create a polymer network that could be classified as an elastomer. Elastomers are comprised of natural and synthetic rubbers. They are amorphous polymers mixed with compounding agents and then vulcanized to give them stability, strength and their well-known elasticity.

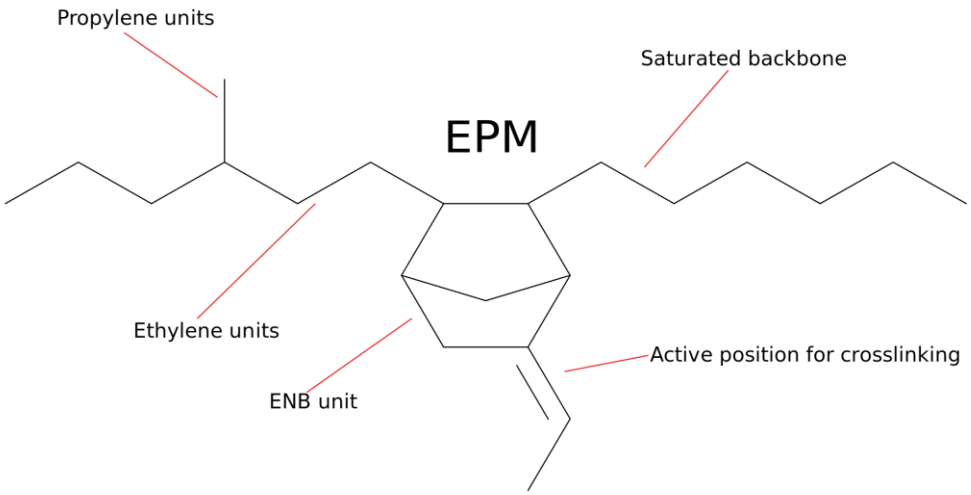

Figure 2.4: Diagram of the propylene and ethylene units connected through the ENB units. The ENB double bond becomes the crosslinking position in order to create the full 3D network. Image from Wikimedia commons.

2.2 Types of Rubber Commonly Used in the Oilfield

Most consumption of rubber worldwide is in the transportation sector, in the form of rubber tyres. Tyres' main component is the natural rubber found in rubber trees, although modern tyres also use styrene butadiene rubber (SBR). Silicone rubber is very common in-house appliances and low-pressure seals. The aforementioned rubber materials have various applications in several industries. In the oilfield industry, rubbers are mostly used as sealants. Typical oilfield industry conditions include exposure to high temperatures, high pressures, large strains and a resistance to gas permeation. For these applications, there are two rubber materials that stand out, Hydrogenated Nitrile Rubber (HNBR) and fluorocarbons (FKM).

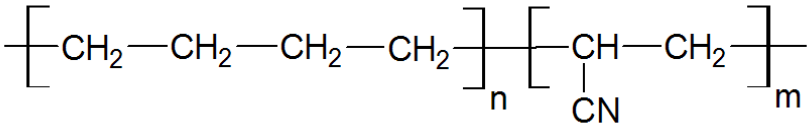

Fig. 2.5: HNBR rubber structure.

Nitrile rubber is a copolymer of acrylonitrile and butadiene rubber. The introduction of acrylonitrile gives the rubber increased strength when compared to butadiene rubber and better heat resistance. The butadiene portion of the rubber can be saturated with hydrogen, further increasing the heat resistance and lowering the susceptibility to oxygen and ozone attack. The structure of HNBR is shown in figure 2.5. The four-methylene chain on the left side (tetramethylene) can be tightly packed, allowing for strong mechanical properties. Acrylonitrile (ACN) content (left side of the polymer chain) gives it better resistance to oil and fuels. Because of the large CN side group, the higher this ACN content, the higher the glass transition temperature (T_g) of the HNBR, which can vary between -40°C and -10°C

[93]. With the inclusion of acrylonitrile, the polarity of the compound increases, generating higher interactions between the rubber and other surfaces. Increased interactions between the rubber and the surface will mean higher frictional forces. HNBR can also crystallise at higher strains [94] depending on the ACN content, but the ranges of deformation are beyond the ones typically observed in seals under normal loading conditions, and not within the scope of this investigation.

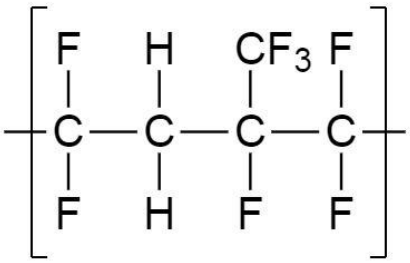

Fig. 2.6: Typical molecular structure of a FKM rubber.

There is a large group of fluorocarbon rubbers in the FKM family, the common theme is that they all have fluorine side groups on the backbone chain to impart greater chemical stability. Service temperatures exceed 250°C and they are more stable than most other rubbers when immersed in solvents, acids or bases.

The chain backbone of FKM rubber (figure 2.6) alternates between CF_2 and CH_2 groups, with a very large CF_3 side group in between them. The sheer size of the side group will increase the T_g of the FKM by a significant amount when compared to the HNBR rubbers. The typical HNBR glass transition (T_g) temperature for oilfield seals ranges between -40°C and -30°C, for FKM it is usually around -20°C. With higher T_g materials typically having higher temperature operating ranges.

Another important effect of the steric hindrance for FKM rubbers are their lower mechanical properties when compared with HNBRs. Since the chain is not so tightly packed, the structure is much more amorphous. Finally, CF bonds of FKM are covalent in nature, meaning that the molecule has very low polarity. With lower polarity, there is less interaction between the rubber and any counter surface, generating lower friction.

2.3 Vulcanisation

In the early 1800s rubber's usefulness as a material was limited due to poor creep resistance resulting from its viscous behaviour. Since they are comprised of amorphous polymer chains, the base form of rubber is not structurally stable. The entanglement of these chains is what causes polymer melts to appear solid. Even with these chains, the inability to maintain a stable geometric shape meant it had almost no use outside of erasers and stopper for sealing liquids. Once the process of vulcanisation was discovered, rubbers became much more versatile [3].

Vulcanisation originally involved mixing elemental sulphur into the rubber compound. When heated, this sulphur forms chemical bridges known as crosslinks between polymer chains where there is some degree of unsaturation to create a crosslinked network. Figure 2.7 illustrates how crosslinking points between polymer chains can be comprised of multiple sulphur atoms in a chain. With the creation of sulphur bridges, the amount of permanent deformation remaining after large strain is reduced. When rubber is deformed the sulphur bridges stretch, once stress is removed, these bridges naturally return the long chain rubber molecules more closely to their original random conformation and they therefore help maintain the network elasticity. This means that after vulcanisation, the elasticity of the rubber is increased, and its plasticity reduced[82]. This solved the long term geometric or flow stability problems of rubber materials and paved the way for the more specialised rubbers we use today.

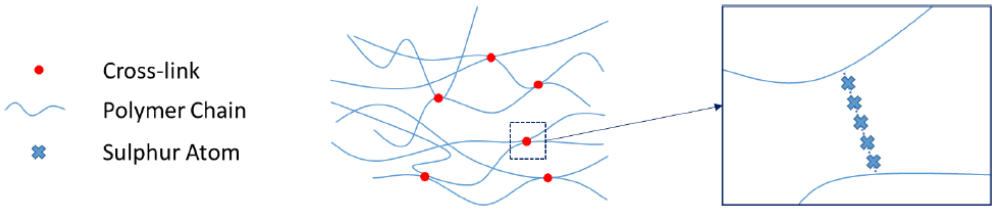

Fig. 2.7: The cross linking of polymer chains with Sulphur vulcanisation. (Adapted from Windslow[4]).

After vulcanisation, the macromolecular network formation makes the rubber almost insoluble in most organic solvents and makes it impossible to reshape. This means that it can no longer be inserted into extruders, mills or mixers. Therefore, vulcanisation must take place after the rubber product has been shaped or moulded into its final form. The elastic modulus of the rubber also increases with vulcanisation, this is because the elastic component of rheological behaviour is related to the degree of crosslinking, whereas the dynamic modulus (which is discussed in section 2.5) is a combination of the elastic and viscous behaviour of the rubber.

Elemental sulphur is still the most widely used crosslinking agent during vulcanisation. The solubility of sulphur in natural rubber, approaches 1% at room temperature[81] but is much higher (at around 7%) when the rubber is at 100°C. Because of this reduction in solubility at lower temperatures, after the rubber goes through the curing process and is cooled, a bloom of any unreacted sulphur is often seen to form on the moulded surface over extended time. This slow migration of sulphur from the bulk compound to the surface after the solubility has been exceeded is known as “sulphur-bloom”.

Sulphur curing is not the only method for crosslinking rubber, peroxide crosslinking methods have also become widely adopted. Peroxide curing is typically used for elastomer compounds that are not crosslinkable using conventional crosslinks with sulphur. One

example would be for a fully saturated polymer which has no double bonds for a sulphur crosslink to attach onto. The peroxide component breaks down into free radicals that attach themselves to polymer chains, the radicals then form crosslinking sites. Sulphur and peroxide curing are the most commonly encountered crosslinking reactions used in the manufacture of rubber products, other systems exist that include metal oxides or diamines, which are also used for specific rubbers, but these are beyond the scope of this work.

These days the traditional vulcanising system includes other chemicals that can act as crosslinking reaction accelerators and activators and other chemicals are also included in the elastomer compound including plasticisers and antidegradants. Accelerators are used to speed up the reaction of rubber with sulphur. Even at high temperatures, the reaction would require hours before the component becomes fully vulcanised. Speeding up the process by reacting with sulphur to create polysulfide bridges that will then react with the rubber. Activators of vulcanisation are used both in sulphur and peroxide vulcanisation. Their main job is to increase the crosslinking efficiency during the vulcanisation process. Zinc oxide is the most used, but it requires a fatty acid to transform the zinc into a rubber soluble form. With stearic acid the zinc oxide is transformed into zinc stearate which is soluble in rubber. Plasticisers are organic materials that help with the workability of the rubber during the compound process, help establish good filler dispersion which helps to enhance properties such as improved fatigue resistance. Antidegradants help with rubber product durability by protecting the elastomer from chemical degradation from agents such as oxygen, ozone, heat, light and mechanical deformation. These chemical degradation effects are referred to as chemical ageing[82]. There are other additives used during vulcanisation, such as peptising, bonding agents and pigments. The explanation of these agents is beyond the scope of the work discussed here.

2.4 The Glass Transition Temperature and Crystallisation

When an external load is applied, the rotation of the polymer chain around the backbone is restricted by either neighbouring molecules, or from groups within the same molecule[5]. Freedom of rotation is related to the thermal energy of the rotating group. The value of this thermal energy (and the resulting ease of movement) increases with increasing temperature. Because of the irregularity of chains in polymers, as a polymer melt is cooled, no polymers can arrange themselves into a perfect fully crystalline structure. However, many polymers can arrange themselves into semi-crystalline structures. For polymers with a relatively low amount of crystallisation, the amorphous polymer chains in the polymer will exhibit at a temperature somewhat below the liquid-solid transition temperature another thermal transition, known as the glass transition. The glass transition (T_g) is the pressure-dependent temperature above which the polymer segments can more readily undergo structural

relaxation [5] . When below the glass transition point, the amorphous (non-crystalline) part of polymers has reduced free volume ratio, thus giving them a “glassy” type of behaviour. This glassy behaviour manifests itself by making the polymer much stiffer as a result of the constraints inhibiting any long-range movement of the polymer chains.

Many rubber materials have a negligible or only limited ability to crystallise. In order to form crystals, the polymer chains must be aligned with each other in a tightly packed structure. The randomness of polymer chains within the system [15], along with stearic hindrance from side groups, may inhibit (under unstrained conditions) for the alignment of the polymer chains to form crystals. Under certain conditions, such as very high strains, natural rubber can form crystals. When natural rubber is strained, the entropy of the system diminishes, the energy is released in the form of heat. At this point, the polymer chains are aligned with each other in a more orderly fashion. With a lower energy state, crystals are formed. Once the strain is removed, entropy is inserted back into the system, with this energy input, the crystals melt and the rubber cools down. Other rubber materials can have a range of crystallisation, under particular conditions, ranging between 30-60%[24]. The rubbers mentioned in section 2.2 show no crystallisation at all in the ranges of deformation used in sealing environments.

Unvulcanised Natural Rubber has a glass transition temperature around -71°C. This is only slightly increased after vulcanisation. More specialised rubbers such as hydrogenated nitrile butadiene rubber (HNBR) and vinylidene hexafluoropropylene rubber (FKM) typically also still have a T_g well below zero degrees Celsius. The precise temperature depends upon the detailed conformation of the different segments in the polymer chain. Meaning that, in most practical operating conditions rubber materials such as those used in elastic seals are designed to operate above the glass transition. With such a large portion of amorphous structure, rubbers above T_g exhibit two particular, very useful properties, hyper-elastic behaviour: meaning deformation ranges above 100% strain (up to 700% in some cases) with full recoverability, although non-linear behaviour, and viscoelasticity.

In the case of seals used at sub-zero temperatures, it is common to set the seal at temperatures well above T_g to ensure full compliance against the surface, and then proceed to reach the lower operating temperature. When this is not practical, a case-by-case approach is common in the industry to observe is the seal can mechanically deform into the sealing position at the setting temperature. The current research does not actually deal with cases with sub T_g seal-setting environments.

High elasticity can be summed into the ability of the polymer to recover from large strain thanks to its flexible chains. This property is what allows rubbers to be used for sealing applications, since they can readily assume different shapes, for example when squeezed between a gland and a mating surface. Viscoelasticity is simply the time-varying

response that the rubber has to external forces. Similar to liquids, this is a frequency-dependent response. Both properties are further discussed in the following section.

The viscous dissipation behaviour of a rubber material is maximised around T_g. This is particularly relevant for rubber friction, as these viscous energy losses make a very significant contribution to the hysteretic component of friction (as discussed in Section 2.9 of this chapter).

Determination of T_g can be done by various methods. The most common ones in industry are calorimetry and dynamic mechanical analysis (DMA). In calorimetry, changes in the specific heat capacity of a polymer are observed as it changes temperature. At the point of glass transition, there is a noticeable jump in the specific heat of the material. Calorimetry experiments test the necessary heat flow that needs to be injected into the system in order to maintain balance with a reference sample. Because glass transition is an endothermic process, there is an increase of the necessary heat flow. The heat flow curve can be analysed in different forms (Fig. 2.8). The preferred method is at the discretion of the analyst. In DMA, the material is subjected to small deformations (typically less than 1% strain) whilst changing the temperature of the rubber being tested. By measuring the polymer behaviour expressed as the in-phase elastic response (G') and the out of phase lagging response of the rubber (G'') it is possible to identify the changes that happen around the glass transition. The ratio of these properties is known as the tan delta (tan δ). At the glass transition, tan δ reaches a maximum value (as shown by curve 3 in Fig 2.9).

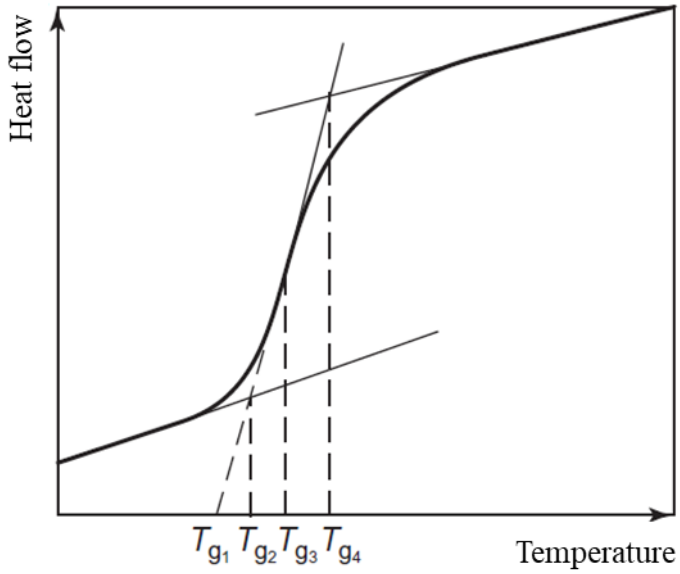

Fig. 2.8: Changes in heat flow with temperature, Methods to obtain T_g are shown as T_{gn}. T_{g1} is the extension of the slope where caloric capacity changes. T_{g2} is where the initial slope crosses the slope of the change. T_{g3} is the midpoint of the slope. T_{g4} is the cross of the slope after the change and the caloric capacity change. All of these are methods of analysing the T_g. It is up to the observer which one will work best. Modified from [6]

It is worth noting that different methods for characterising the T_g can yield different

results. Cooling and heating rates, frequency of loading and other variables can cause small shifts between different test methods. The decision of which one to use comes down to repeatability, time, cost and the specific application.

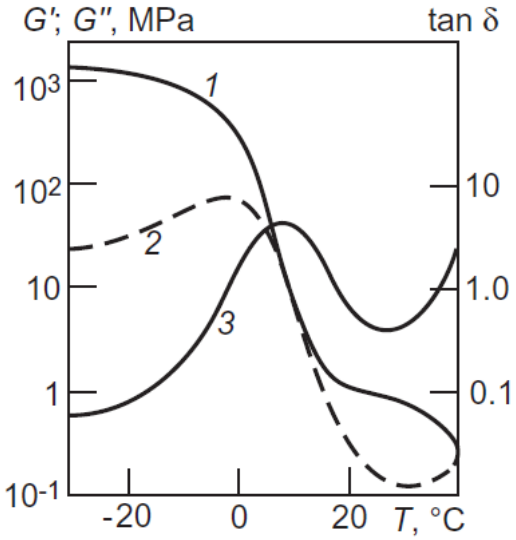

Fig. 2.9: Curves representing G' (1), G''(2) and tan δ (3). T_g is the temperature where the tan δ peak is ~8°C. Taken from [6]

2.5 Mechanical Properties of Rubber

Robert Hooke proposed in 1678 that the force (F)required to extend or compress a spring by a distance x, increases linearly with an elastic constant k ($F = kx$). This behavior can replicate (to a certain extent) what is observed in materials during the initial stages of deformation. When analysed in terms of cross-sectional area of materials, we obtain the equation

$$\sigma = E\varepsilon \tag{1}$$

Where σ is the stress that is applied on the body, E is the Young's (or elastic) modulus and ε is the strain. This is known as "Hooke's law" and it is still commonly used when understanding the stiffness of the material in its elastic zone[7].

Analogously, a viscous behaviour can be analysed through the movement of a dashpot. The force (F) required to move the liquid past the piston at a velocity v increases by a constant c ($F = cv$) when we look at it in terms of force per unit area, the equation becomes

$$\sigma = \eta\dot{\varepsilon} \tag{2}$$

Both of these equations represent the ideal conditions of a perfectly elastic material, and a perfectly viscous material. There is no material that has these conditions, they will have behaviours outside of this range. Rubbers' most well-known property is their high elasticity and their ability to "bounce back" into shape even after large (>300%) extensions[11]. There are, however, viscous components to the mechanical response of

rubbers when exposed to external forces, most important, creep and stress relaxation.

Creep is the slow flow of polymer chains when a constant external stress is applied. In an elastic material, strain will increase only after stress is applied. If we hold the stress at a constant value, there will be no more changes in the material's extension. Polymer structures do not behave in such a way. When an external stress is kept at a constant, polymer chains will slowly flow past each other and allow for the material to further deform in the direction of the stress. Figure 2.10 describes this effect with a simple diagram. Although there is a section of the polymer that behaves in an elastic fashion, there are also viscous effect such as creep taking place.

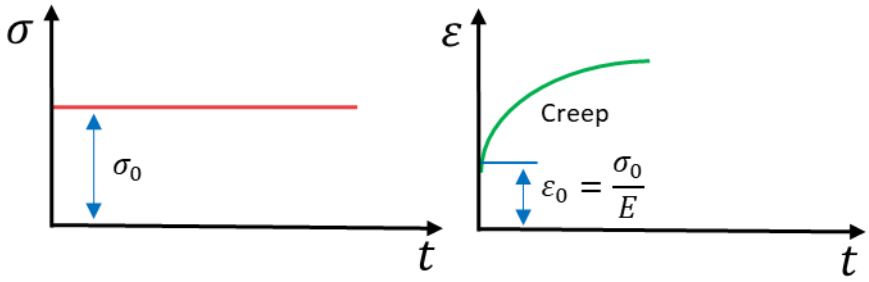

Figure 2.10: Constant stress σ_0 being applied for a time t (left). After the initial strain ε_0, the constant stress causes the strain to increase (left).

Stress relaxation is the other viscous behaviour that polymers exhibit. The root of this behaviour also lies in the realignment of polymer chains. When instantaneous strain is applied to the material, there is a stress response that slowly decays over time. Since strain will pull on polymer chains' entanglement, the initial stress is high. If this level of strain is kept constant, the polymers will slowly slither past each other, reducing the total stress the system is subjected to.

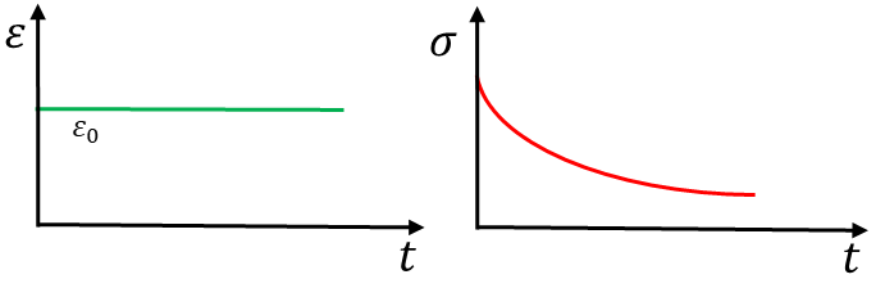

Figure 2.11: Initial strain ε_0 is applied to the polymer (left). Stress response decays over time after polymer chain realignment(right).

Figure 2.11 illustrates the stress relaxation phenomenon. Stress will decay in an exponential way after the strain is kept constant. Polymers exhibit both creep and stress relaxation, in order to model the mechanical behaviour of them, integrating both of these effects is key. The spring and the dashpot models will be essential in describing the polymer's response to an external stress.

In 1867, James Clark Maxwell set out to describe the elastic and viscous component that govern the behaviour that materials have when placed under strain[13]. It is represented as a dashpot, which has purely viscous behaviour, and a spring, with purely elastic behaviour. He assumed that connecting both elements in series would lead to a full description of polymer behaviour.

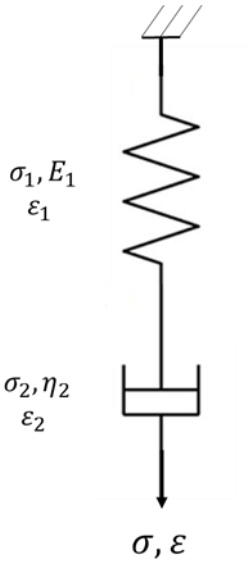

Fig: 2.12: The model James Clark Maxwell proposed to describe material behaviour.

The diagram in figure 2.12 is subjected to an external stress σ, the spring and dashpot contributions can be described by the equation

$$\frac{d\varepsilon}{dt} = \frac{1}{E} \cdot \frac{d\sigma}{dt} + \frac{1}{\eta} \cdot \sigma \tag{3}$$

After applying the conditions $\sigma = \sigma_0$ (creep) and $\frac{d\varepsilon}{dt} = 0$ (stress relaxation) the model resolves to the results in figure 2.13

An initial, constant stress is applied, causing an instantaneous strain response. After the stress is held, strain increases linearly until t_1(Newtonian flow). This is unrealistic for a polymer. After t_1 and until t_2 the strain is kept constant and the stress decays exponentially, this is a good description of polymer behaviour. After t_2 the remaining stress (σ') is completely removed and the material recovers only the elastic portion of the strain, unlike real polymer behaviour.

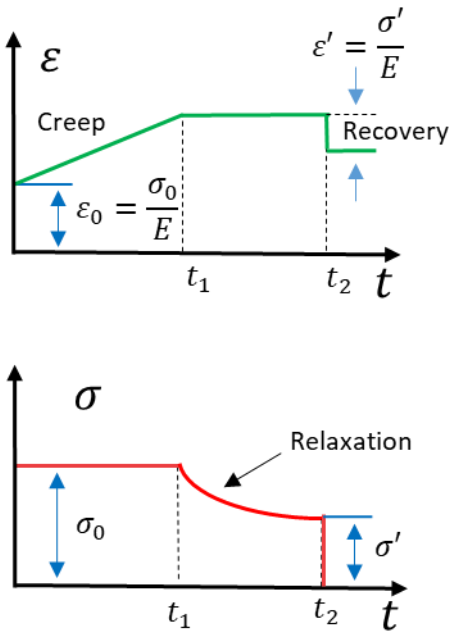

Figure 2.13: Behaviour of the Maxwell model after the initial stress σ_0 until time t_1. Strain is then kept constant until t_2, after which, stress is immediately removed.

Whilst a Maxwell material does not completely recreate polymer behaviour, it does get closer to it than a dashpot or a spring model. In order to do a complete description, another model arose in the late 1800s, the Kelvin-Voigt model, described in figure 2.14.

The Kelvin-Voigt model was like the Maxwell model, in that it comprised a spring and a dashpot to show both the elastic and the viscous component of the material. The difference in this model, is that the elements are connected in parallel, not in series.

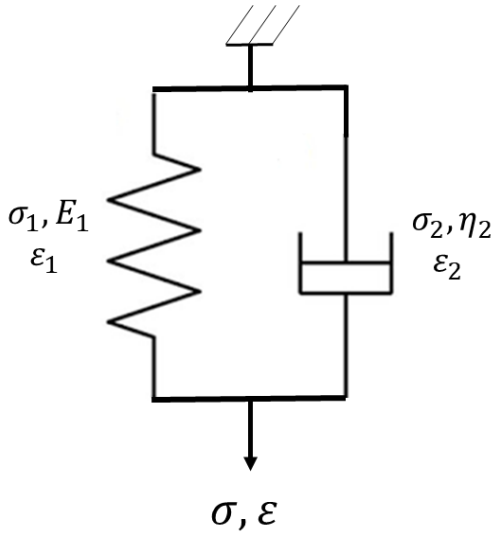

Figure 2.14: The Kelvin-Voigt model.

Following the previous method of boundary conditions for both creep and stress relaxation, the Kelvin-Voigt model (fig 2.14) can be described with the following equation

$$\frac{d\varepsilon}{dt} = \frac{\sigma}{\eta} - \frac{E\varepsilon}{\eta} \tag{4}$$

The outputs of this model are presented in figure 2.15

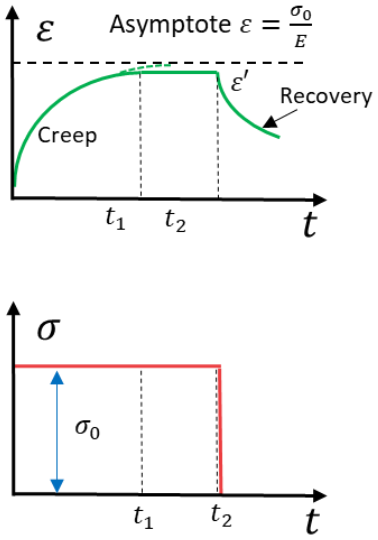

Figure 2.15: Kelvin-Voigt model showing a constant stress applied to the material.

In this new model, the creep behaviour is similar to the one observed in polymers, however, there is no instantaneous response of strain during loading or unloading. The Maxwell model and the Kelvin-Voigt model, both describe a part of polymer behaviour, but none of them do it completely. When combined, they transform into the standard linear solid model (fig 2.16)

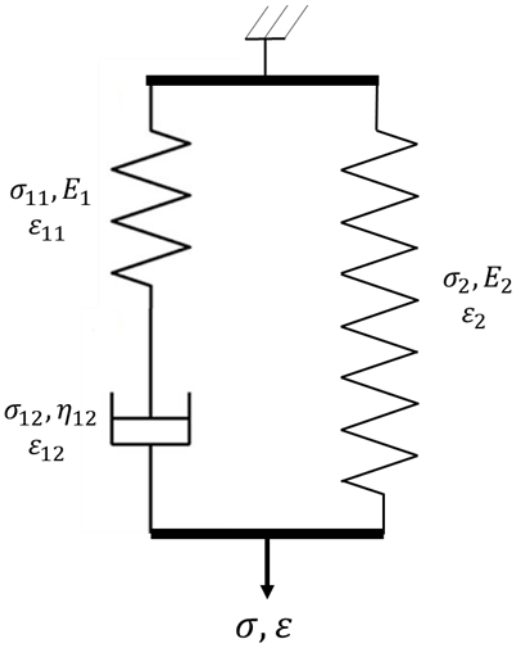

Figure 2.16: Standard linear solid model. Combination of the series and parallel arrangements of a dashpot and springs.

When analysed, the standard model outputs the equation

$$\sigma + \frac{\eta}{E_1}\frac{d\sigma}{dt} = E_1\varepsilon + \frac{\eta_{12}(E_1+E_2)}{E_2}\frac{d\varepsilon}{dt} \tag{5}$$

After boundary condition analysis, the output of equation is evaluated and presented in figure 2.17

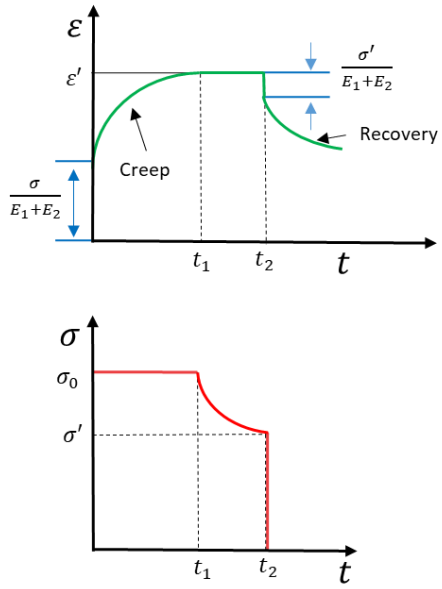

Figure 2.17: The Standard linear solid model presenting creep (t_1), stress relaxation (t_2) and recovery (>t_2)

From the start, up to t_1 there is a constant initial σ_0 which generates an instantaneous strain response. After that, there is an exponential increase in the strain, as it corresponds to polymer behaviour. Between t_1 and t_2, strain is kept constant, causing an exponential decay in stress, a good representation of stress relaxation. After removing stress completely ($t > t_2$) there is an instantaneous recovery of the strain, and a slow progressive recovery of the amorphous part of the solid. The standard linear solid model properly describes the phenomena of polymer deformation. Both viscous and elastic effects are covered.

Even though polymer behaviour could be well described by the previously mentioned models, the response from elastomers has some added difficulty. At the monomer level, polymer melts behave similarly to liquids. The packing of the polymers is so tight, that changes in volume are very difficult. During experimental testing, rubber has been observed to have minimal volume changes during deformation[15]. This allows for some mathematical play when analysing three-dimensional strains under complex stress conditions. Besides the previously mentioned models, elastomers are not linearly elastic and fairly dependent on strain rate, and that does not cover the effects of the filler networks. The approach for rubber models that represents their hyperelastic and viscoelastic behaviour is a thermodynamic one. Once fillers are involved, this condition may not be always fulfilled. Since large amounts of strain could create voids for example by separating fillers from the rubber matrix, creating a vacuole, leading to an increase in volume.

2.5.1 Thermodynamic Approach

If we observe a block of rubber as a small thermodynamic system, we can relate its physical properties to internal energy and entropy [15]. From the first law of thermodynamics, the change that the internal energy of the system (dU) is given by:

$$\mathrm{d}U = \mathrm{d}Q + \mathrm{d}W \tag{6}$$

$\mathrm{d}Q$ and $\mathrm{d}W$ are defined as: the heat absorbed by the system and the work done on it by external forces, respectively. Looking at the entropy parameter S in a reversible process is described in the second law as:

$$T\mathrm{d}S = \mathrm{d}Q \tag{7}$$

Combining Eqs. 6 and 7 we can see that for a reversible process:

$$dU = TdS + dW \tag{8}$$

The deformation of rubber at a constant temperature is related to a reduction of entropy. Polymer chains are aligned, and the disorder of the system reduces. Since rubbers are incompressible solids, there is no change of internal energy in the system. Knowing this we can change $\mathrm{d}U = 0$. Rearranging Eq. 8:

$$\mathrm{d}W = -T\mathrm{d}S \tag{9}$$

Substituting from Eq. 7:

$$\mathrm{d}W = -\mathrm{d}Q \tag{10}$$

We can conclude that by stretching a rubber ($W > 0$), the $\mathrm{d}Q$ (or heat absorbed) is negative. If this is true, then when rubbers undergo deformation, the heat absorbed is equal to the work done. This is observed at any scale and can easily be tested by stretching a rubber band. more it When you stretch the rubber band it gets warmer to the touch.

James and Guth [13], Flory and Rehner [14] and Treloar [15] refined a theory proposed by Kuhn [16] that tries to determine the elasticity of a molecular network based on the deformation of the polymer chains. It relates the entropy of the rubber with the deformation in the axial directions.

$$\Delta S = -\frac{1}{2}Nk(\lambda_1^2 + \lambda_2^2 + \lambda_3^2 - 3) \tag{11}$$

where N is the number of rubber chains and k is the Boltzmann constant. Fig. 2.18 shows the source of $\lambda_1, \lambda_2, \lambda_3$ which are strain ratios in the x, y and z axes, caused by the t_1, t_2 and t_3 tensions, respectively.

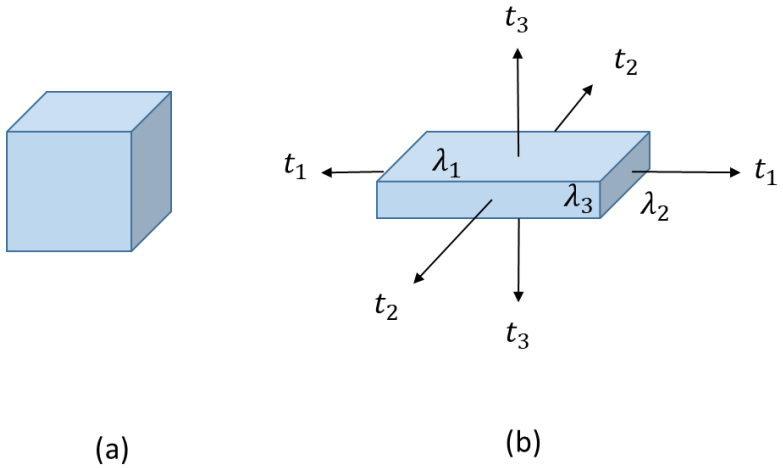

Fig. 2.18: A block of rubber is deformed in all directions by external forces, strain ratios are parallel to these external forces. (Adapted from Treloar [58]).

2.5.2 Strain Energy Functions

Assuming once again that there is no change in internal energy, we can combine Eqs. 9 and 11 into:

$$W = \frac{1}{2}NkT(\lambda_1^2 + \lambda_2^2 + \lambda_3^2 - 3) \tag{12}$$

where W is the work of deformation, which can translate into elastically stored free energy per unit volume of rubber. This form of studying the work of deformation is known as a *strain-energy function* (SEF).

Rivlin made a general polynomial expression, represented by:

$$W = \sum_{i,j,k=0}^{n} C_{ijk}(I_1 - 3)^i(I_2 - 3)^j(I_3 - 1)^k \tag{13}$$

where C_{ijk} are fitting parameters, i, j, k are positive integers, and I_1, I_2 and I_3 are called the strain invariants. The invariants can be calculated from principal stretches by

$$I_1 = \lambda_1^2 + \lambda_2^2 + \lambda_3^2 \qquad I_2 = \lambda_1^2\lambda_2^2 + \lambda_2^2\lambda_3^2 + \lambda_1^2\lambda_3^2 \qquad I_3 = \lambda_1^2\lambda_2^2\lambda_3^2 \tag{14}$$

Maintaining the assumption that natural, unfilled rubber is an incompressible material, $I_3 = 1$ and the equation is simplified into

$$W = \sum_{i,j=0}^{n} C_{ij}(I_1 - 3)^i(I_2 - 3)^j \tag{15}$$

For filled rubbers, the concept of incompressibility (Poisson's ratio = 0.5) is still valid for deformations where no strain-induced microstructure changes occur[95]. A SEF with a single coefficient is known as neo-Hookean [17]. In 1990, Yeoh [18] proposed a SEF that is generated using only terms of I_1, which makes it extremely convenient, since I_1 is directly correlated with λ_1 during uniaxial testing for tension and compression. During uniaxial deformation testing, it is assumed that λ_2 and λ_3 are equal to $1/\sqrt{\lambda_1}$ because of the incompressibility principle. Yeoh curve fitting for all modes of deformation is made easier by using I_1 exclusively:

$$W = C_{10}(I_1 - 3) + C_{20}(I_1 - 3)^2 + C_{30}(I_1 - 3)^3 \tag{16}$$

This SEF is adopted throughout this entire work.

2.5.3 Viscoelastic and Hysteretic Effects

Rubber's mechanical behaviour goes beyond the nonlinear stress-strain relation. One of their main descriptors is the frequency dependent response to dynamic and cyclic stress. This type of behaviour is called viscoelasticity, and it can be summarised as the stress response σ to a strain ε at a certain strain rate $\dot{\varepsilon}$.

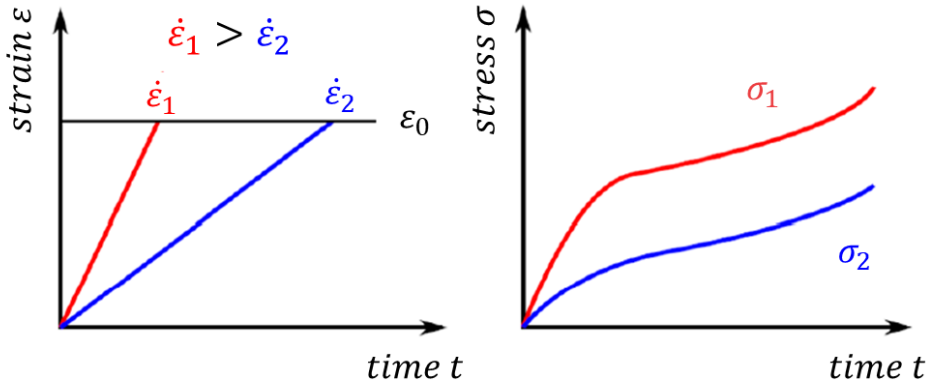

Fig. 2.19: Strain rate dependence of stress response. Since ε has the same magnitude for both cases, but ε_1 takes place in a shorter time interval, the rate of deformation is higher, leading to a larger stress response.

Fig. 2.19 illustrates how there is a higher stress response to the same magnitude of strain if it is done in a shorter amount of time. If a body undergoes dynamic oscillatory excitation, where strain behaves as a sinusoidal wave and the stress response is recorded, the energy applied to the material is modelled as:

$$\gamma(t) = \gamma_0 \sin(\omega t) \tag{17}$$

where $\gamma(t)$ is the shear deformation and ω the angular frequency. A sinusoidal deformation that has the amplitude γ_o and an excitation frequency $\omega = 2\pi f$ (f is frequency in Hertz) results in a response of the material shear stress τ that is time dependent:

$$\tau(t) = \tau_0 \sin(\omega t + \delta) \tag{18}$$

The material response phase angle being δ and the amplitude τ_0. Fig. 2.20 is a diagram of the different type of responses materials can have to this deformation. The time delay between the oscillatory excitation and the material's response can be presented as the angular phase difference between the signals. A perfect elastic body has an instantaneous response, $\delta = 0°$; meaning that all the energy is elastically stored in the body during the loading phase, and it is completely released during unloading. An ideal fluid will have a response of $\delta = 90°$; this indicates a total release of the supplied energy in form of heat due to the internal friction of the fluid. There are elastic and viscous parts in all materials, but there is typically a dominant part. In viscoelastic materials such as rubbers, both parts are equally represented.

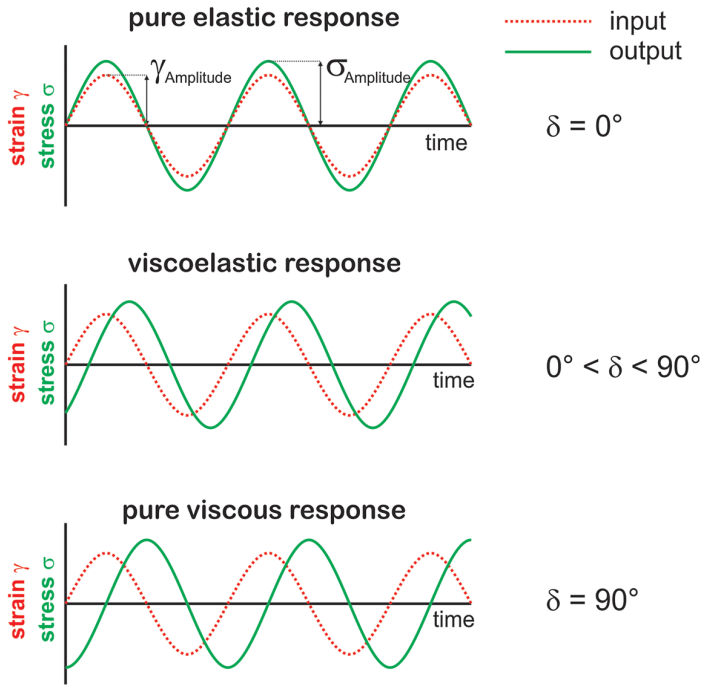

Fig. 2.20: Definition of elastic, viscoelastic and pure viscous responses to oscillatory excitation of materials, illustrated in terms of angle phase between stress and strain. (Adopted from [8]).

The shear stress signal $\tau(t)$ can be then divided into two different contributions. The first one is in phase with the strain $\tau_0 \cos \delta$. A second one is 90° out of phase with the strain $\tau_0 sin\ \delta$. These contributions are defined as two different moduli by

$$G' = \frac{\tau_0}{\gamma_0} \cos(\delta) \tag{19}$$

$$G' = \frac{\tau_0}{\gamma_0} \sin(\delta) \tag{20}$$

$$G^* = G' + iG'' = \frac{\tau_0}{\gamma_0} \cos(\delta) + i\frac{\tau_0}{\gamma_0} \sin(\delta) \tag{21}$$

where G' is the elastic or storage modulus (the in-phase component) and G'' is the viscous or loss modulus (out-of-phase component). G^* is the complex modulus, and the ratio between the loss and the storage modulus is called the loss factor or loss tangent. This is essentially the ratio of dissipated to elastic energy.

$$\tan(\delta) = \frac{G''}{G'} \tag{22}$$

One of the main consequences of energy losses is what is known as hysteresis, which is a measure of the energy dissipated during any given loading cycle. The rubber's energy loss is not equal for every cycle of deformation, each time the rubber is loaded and then unloaded, there is an appreciable difference in the stress response for the same level of strain (Fig. 2.21). This behaviour is known as cyclic stress softening. This effect is accentuated by the rubber's filler network. Filler-filler interactions play a major role in the energy storage and dissipation when under stress. When under strain, elastomer filler networks begin to break down, when unloaded, the stress response is much lower than during loading. When plotted on a stress-strain graph, this area under the curve is the loss

of energy per cycle, named hysteretic losses, which are known as the Mullins effect [20]. As long as filler-rubber interface is not broken, when the rubber matrix goes back to its initial state, the filler network can make a slight recovery in the conductivity**Error! Reference source not found.**, but a mechanical recovery is unlikely

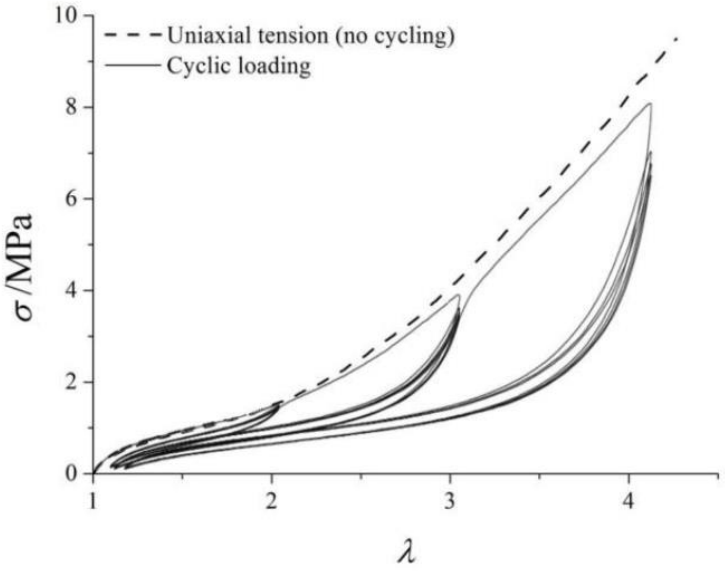

Fig. 2.21: Cyclic stress/strain behaviour of SBR. Areas under loading/unloading curves are hysteretic energy losses. (Adopted from [21]).

Another important filler network breakdown consequence is what is known as the Payne effect [22]. At very low strains, the filler network is unchanged by the application of the strain, and thus, the modulus remains intact. When the strain amplitude becomes larger, the stiffness is effectively reduced, but there is a maximum of the loss modulus. This is what is known as the Payne effect . Figure 2.22 denotes the change of $G_0{}'$ to $G_\infty{}'$ as the strain amplitude is increased. The same thing is true for G'' but it passes through a small window where it reaches G''_{max}.

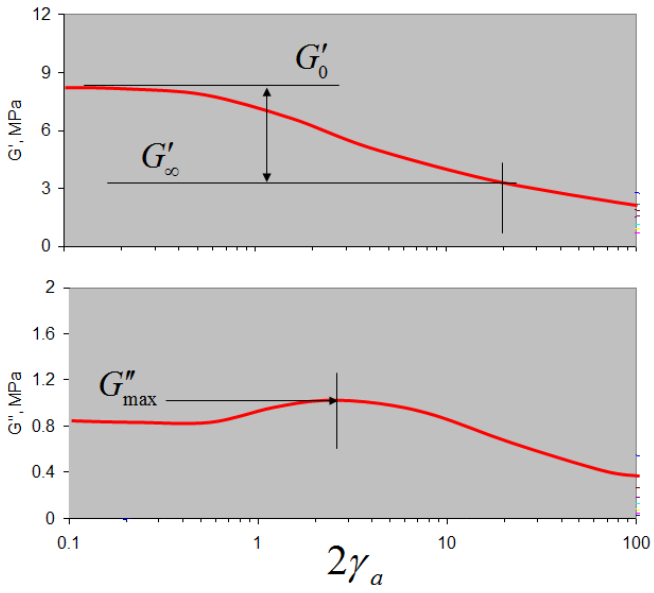

Fig. 2.22: Illustration of loss modulus peaking during the breakdown of the filler network as strain is increased (Payne effect). (Adopted by Endurica LLC and Wang, M.J., 1999 [23]).

2.6 Time Temperature Superposition (The WLF Shift)

The time-temperature superposition principle is based around a simple idea. If a property of the rubber is governed by its viscoelastic behaviour or the rate of relaxation of the polymer chain, then the property must be controlled by the proximity of the polymer to the T_g. In practice with viscoelastic properties such as G' the measured property is dependent upon both the temperature and the rate at which the polymer is tested. There is an equivalence whereby doing a test at a higher rate is equivalent to doing the test at a lower temperature, as both result in a material that has a higher modulus. This approach can be mapped to other properties controlled by the viscoelastic behaviour such as the frictional coefficient. In this case a change in temperature can be considered as being equivalent to a change in the sliding rate[24].

Let us use a commonly understood property, such as elastic modulus. At low temperatures (sub T_g), chain mobility and free volume are minimal. Any form of strain of the rubber requires a large intake of energy, which results in a large E'. If we were to deform a rubber above its T_g at very low frequencies, the chains have time to fully respond to the deformation, and this quasi-static deformation is what is commonly defined as the modulus at a particular temperature. By increasing the testing frequency of any deformation, the polymer chains will not have some time to catch up with the applied force causing them to move. This constraint on the deformation acts to increase the E'[24].

With this principle, time-temperature shift factors (a_T) can be derived for a corresponding reference temperature in order to create a mastercurve that shows material property changes across a very wide frequency range. The Doolittle equation [8] derives these shift factors by assuming that the rate of molecular motions is determined by the free

volume.

$$\log_{10}\eta(T) = \log_{10}\eta A_{\mathrm{D}} + \frac{B_{\mathrm{D}}}{f_{\mathrm{V}}(T)} \tag{23}$$

where A_{D} and B_{D} are constants, relating the viscosity of molecular liquids to the fractional free volume. f_{V} is the fraction of specific volume by the occupied volume normalised by total mass $(V/V_{\mathrm{o}} - 1)$.

Assuming a linear expansion of the free volume with temperature, $\mathrm{d}f_{\mathrm{V}}/dT|_{\mathrm{P}} \propto T$, we obtain the Williams-Landel-Ferry (WLF) equation[10].

$$\log_{10} a_{\mathrm{T}} \equiv \log_{10}\left(\frac{\eta(T)}{\eta(T_{\mathrm{ref}})}\right) = \frac{-c_1(T-T_{\mathrm{ref}})}{c_2+T-T_{\mathrm{ref}}} \tag{24}$$

Here T_{ref} is an arbitrary temperature chosen for the translation of the property. Constants $c_1$and c_2 are the so-called "universal" constants used in the WLF experiments, frequently used with values of $c_1 = 8.86$ and $c_2 = 101.6$ K. More realistically, these constants change with rubber types and should be more like empirical fitting parameters that need to be determined.

The time-temperature superposition has been applied to various properties such as creep compliance and tearing energy of rubbers [11]. More important for this work, is the application of this shift parameter to non-linear properties, such as the frictional resistance to sliding. Research by Grosch in 1963 [12] demonstrated the validity of the superposition principle being applied to rubber frictional sliding. By measuring how the frictional sliding force encountered by different types of rubber at specific test temperatures, varied with sliding velocity, frictional values were created that could be translated into a single master curve at a reference temperature (as shown in Fig. 2.23).

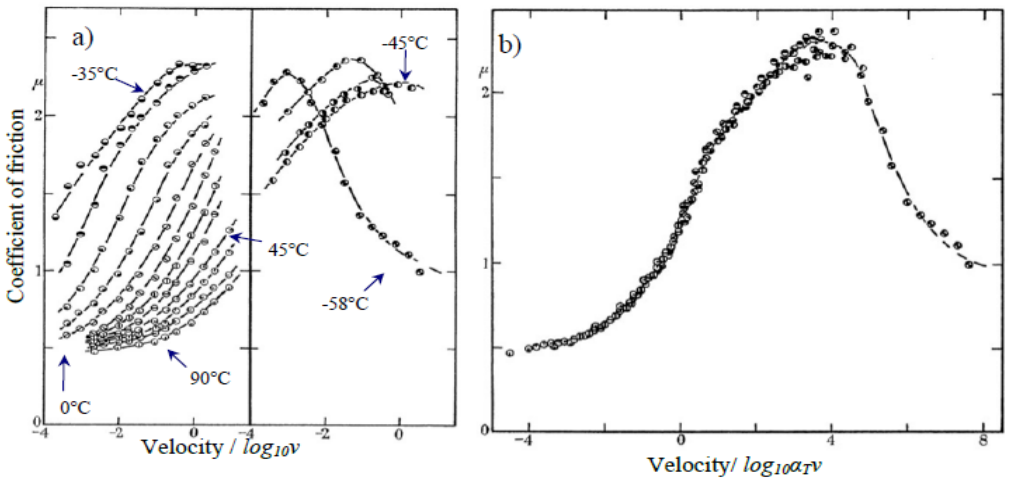

Fig. 2.23: Coefficient of friction as function of sliding velocity for different temperatures (left). Mastercurve of coefficient of friction as a function of sliding velocity after a WLF shift with T_{ref} = 20°C (right). (Adapted from [12]).

2.7 Rubbers and Sealing

When reviewing the performance of rubber seals, the frictional behaviour of the elastomer comes into place by increasing the tangential force that the fluid penetration needs in order to go through the sealing face. Fig. 2.24 demonstrates the case for fluid penetration when relating the contact pressure to the friction interaction between the surfaces. The dotted line represents the applied pressure on the seal. If the contact pressure is lower than the applied pressure, the seal will leak. Different coefficients of friction will change the contact pressure profile, which in turn changes the leak pressure.

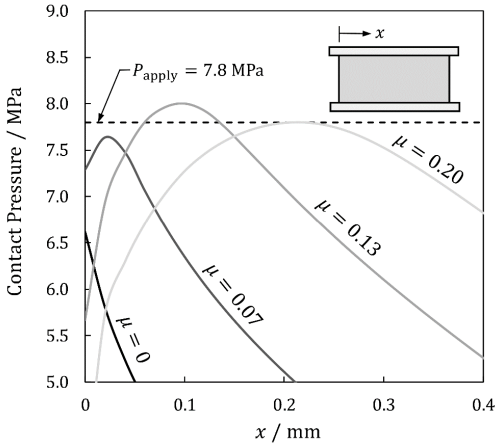

Fig. 2.24: The contact pressure after an application of 7.8 MPa fluid pressure with different friction coefficients. (Adopted from Hohenberger [59]).

In terms of sealing elements, O-ring rubber seals are one of the most common seals for many industries, from low pressure appliances to high temperature/high pressure oilfield downhole applications. The O-ring seal is what is used as a model for the research project.

2.8 Finite Element Analysis of Elastomers

2.8.1 Introductory Concepts

In order to reduce costs when testing key material components, computational based strain energy calculations are commonplace in the industry. Finite element analysis (FEA) is an approach to solving complex engineering problems that would create extremely intricate analytical solutions.

FEA breaks down large components into small shapes, those shapes are known as elements, elements then combine into a mesh. The corners of each element contain a node, the node has a set of coordinates that indicate its position. This entire process is known as meshing, or discretization. Dividing the complex problem like this, makes a large intricate analysis into tiny little partial differential equations. Using computational power, FEA solvers Using computational power, the partial differential equations for the nodes are then solved with the user-inputted conditions.

If we consider each element as its own small material model, then each element's

behaviour must be compatible with the material model. Each element also shares the node of each of its corners, with the other neighbouring elements. Therefore, the complete geometry can be represented as the sum of all elements. The number of elements included in the mesh increases the precision of this sum. The downside to this increase is that computational power necessary to solve the differential equations will also increase.

For this particular study, elements are provided with rubber material behaviours through strain energy function (SEF) curve fitting. Using Yeoh SEF (Eq. 16) we can observe the stress response after applying a uniaxial stretch λ. We will differentiate Eq. 16 into

$$\sigma = 2C_{10}\left(\lambda - \frac{1}{\lambda^2}\right) + 4C_{20}\left(\lambda - \frac{1}{\lambda^2}\right)\left(\lambda^2 + \frac{2}{\lambda} - 3\right) + 6C_{30}\left(\lambda - \frac{1}{\lambda^2}\right)\left(\lambda^2 + \frac{2}{\lambda} - 3\right)^2 \quad (25)$$

For a complex geometry, that equation would be extremely difficult to resolve. There are no linear paths for force applications, geometric components of stress and strain need to be calculated for each point of inflexion, rotational moments are not equal for all parts of a body. If the body is broken down into small square elements, one can assume that the behaviour between but when broken down into small elements, we simply need to do that equation for many small, elements, and add the results..

Figure 2.25 shows how a geometry that has angular moments, circular voids and curved corners can be fitted using tetrahedral elements, these elements are connected at junction points known as nodes. Equations of stress response, heat and electrical conductivity and more can be solved for each node using linear or quadratic equations. The solution of elements adjacent to each other uses the solution of the previous element as boundary conditions. This process is repeated until the entire system of equations is solved.

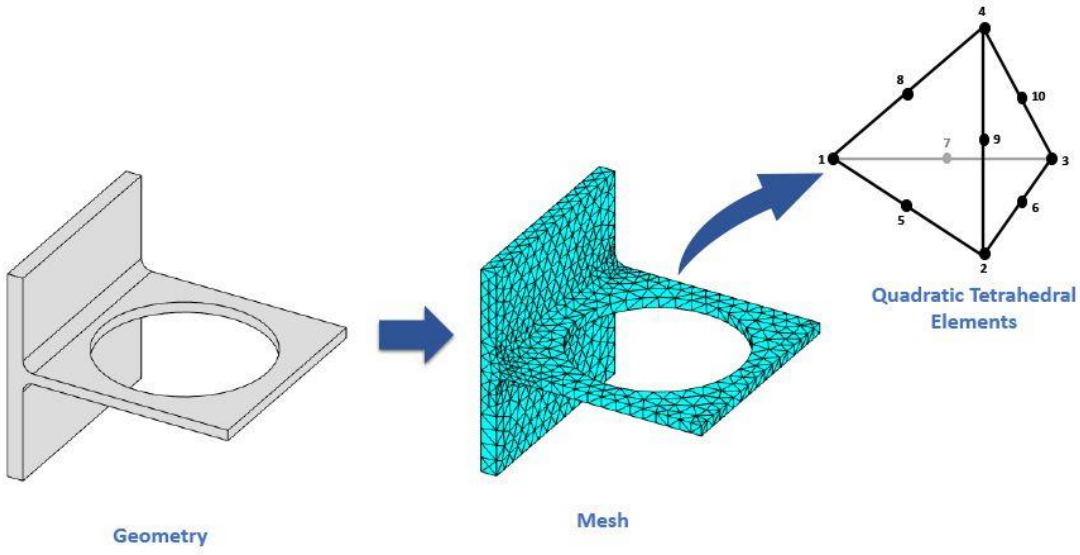

Figure 2.25: Development of a mesh composed of tetrahedral element from a complex geometry (taken from MatLAB MathWorks)

2.8.2 Curve Fitting and Abaqus

Using Abaqus curve fitting method, stress/strain values from the material characterisation results (chapter 3) are used as inputs in the material manager section. Since only uniaxial tension and compression results are available, the Yeoh strain energy function is selected as the polynomial fit. Abaqus will find the coefficients C_{10}, C_{20} and C_{30} and from them obtain strain energy per unit of reference volume.

It is worth noting that all the calculations that Abaqus does when it comes to volumetric results (such as strain energy *density*), it is using a single unit value of thickness. Abaqus does not require units as an input, so the thickness will be whatever length unit one uses for the geometry (1 mm, 1 inch, etc). All units must be in the same system to avoid calculation errors.

2.8.3 Friction Modelling in Abaqus

Abaqus has various methods to model surface-surface interaction between two defined bodies, in order of appearance they are:

- Frictionless interaction: this is the default method selected by Abaqus, it implies no tangential forces are generated by the contact between surfaces. Although the simplest one, this method is not realistic, since there is no such thing as frictionless contact.

- Penalty: with a user defined μ, and the calculated contact pressure, Abaqus will calculate the contact area (using the default 1.0 cross sectional area per node) and obtain a critical shear stress τ_{crit}. After the tangential forces overcome the critical shear stress, the element will move past the current contact surface.

This μ can be defined by the Coulomb type of friction, a single constant value. A pressure dependent μ which changes with changing contact pressure on the element's face. Or slip rate dependence, which uses velocity components to determine the frictional behaviour.

- Static-kinetic exponential decay: Although it might seem like a complex method of estimating rubber friction, it is simply a separation of kinetic (μ_k) and static (μ_s) friction coefficients, the μ is defined by:

$$\mu = \mu_k + (\mu_s - \mu_k)e^{-d_c \dot{\gamma_{eq}}} \tag{26}$$

Where d_c is the decay rate of the static coefficient and $\dot{\gamma_{eq}}$ the slip rate. This model (Figure 2.26) does not allow for pressure or temperature dependency.

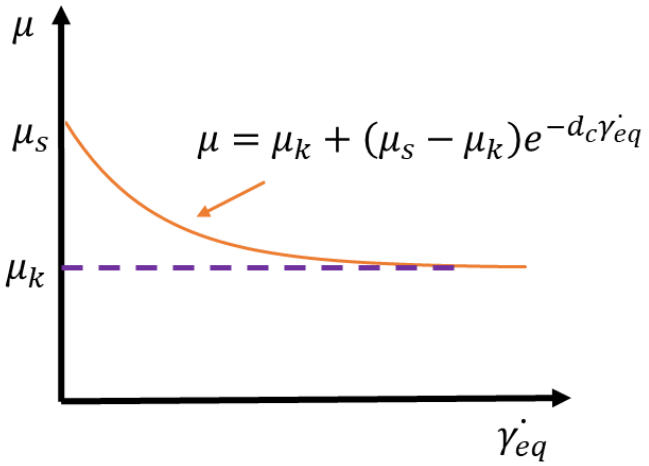

Fig. 2.26: The decay rate model of coefficient of friction. (Adopted from Dassault Systemes (2018)).

One could also specify a maximum shear stress method, where if a τ_{max} is reached, the surface will slide regardless of contact pressure. This is more akin to an adhesion phenomenon.

- Rough: the rough method simply prevents any slipping between two surfaces, essentially $\mu = \infty$.

Section 2.9 explains the typical behaviour of rubber friction and what type of contact penalty to select.

2.8.4 Modelling Pressure Penetration

In order to simulate high pressure levels required in seals, the pressure penetration method allows us to cover a geometrical surface with increasing fluid pressure until it makes contact with another body. Leak prediction could be calculated with this method. By analysing the interfacial pressure between a node and a surface, if the node has a lower pressure than the fluid pressure, then the node will be detached from the surface. Since this research is related purely to the characterisation of friction and the validation of models typically used in the tyre industry, the pressure penetration model is simply used to simulate the friction rig pressurisation effects. Further research is required to evaluate how friction models change the fluid penetration prediction.

2.8.5 Finite Element Mesh

The smaller our elements (higher quantity) the higher the precision. There are ways in which one can augment the number of elements without drastically increasing the computational power required.

If a component to be simulated has an axis of symmetry, one could simply model a section of it, instead of the entire 3D model. For the type of seals used in this investigation (O-rings), an axisymmetric model covers the entire 360° of rotations, whilst using the computing power for only 1°. Clever sectioning of the elements can save a lot of time and

resources if several models are to be run.

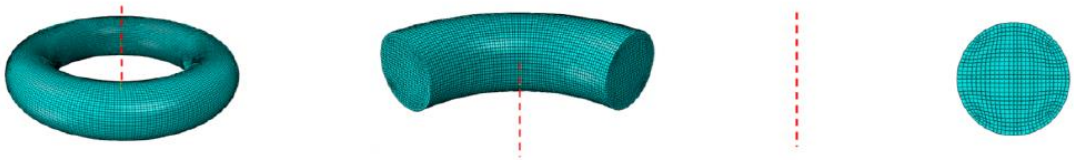

Fig. 2.27: Meshing of a full 3D O-ring reduced to a single circle.[4]

The final mesh used in the O-ring analysis models is presented in chapter 4. The basic concepts of finite element analysis have been presented in this section. Only the stress response from a pressurised O-ring is required from this technique, as such, it was not discussed at great length.

2.9 Friction of Rubber

"*Would you be OK to work with me?...a Jew?"*
...asked Schallamach
"I should be the one asking you professor, if you'd be OK working with me...a German"
...responded Grosch

2.9.1 An Overview of Friction

Frictional behaviour of materials is often simplified to a relationship between the perpendicular forces acting on a body (normal force) and the forces opposite to movement (frictional force). This behaviour is then condensed into a single value (coefficient of friction) that is commonly used independently of the working conditions of the material and the tribological characteristics of the substrate. The approach may have been appropriate when first used in the year 1493 by Leonardo Da Vinci [25] but it no longer holds water in any respectable engineering development. Rubber is particularly non-conforming when it comes to linear frictional behaviour, and the viscoelastic effects make it difficult to predict key engineering conditions such as break-away friction, energy dissipation during dynamic friction and wear.

The coefficient of friction (CoF) versus displacement graph (Fig. 2.28-left) is the first (and for some, the only) conceptual introduction of frictional behaviour. This behaviour is known as Coulomb friction [26]. The theory is presented with four axioms:

1. The friction force is proportional to the normal load.
2. The coefficient of friction is independent of apparent contact area.
3. The static coefficient of friction is greater than the kinetic coefficient of friction.
4. The coefficient of friction is independent of sliding speed.

The first point is just basic physics of the layout of forces acting on a body; thus, it is true. Point number two is only true for materials with a clear elastic-plastic behaviour, which is not the case for rubber. Number three is not true for viscoelastic materials because of stress-relaxation that could cause an increase in friction due to hysteresis energy losses as the rubber element is moving. Lastly, number four is false for every type of material. A change in the sliding velocity will change the local deformation magnitudes, temperature and material stiffness.

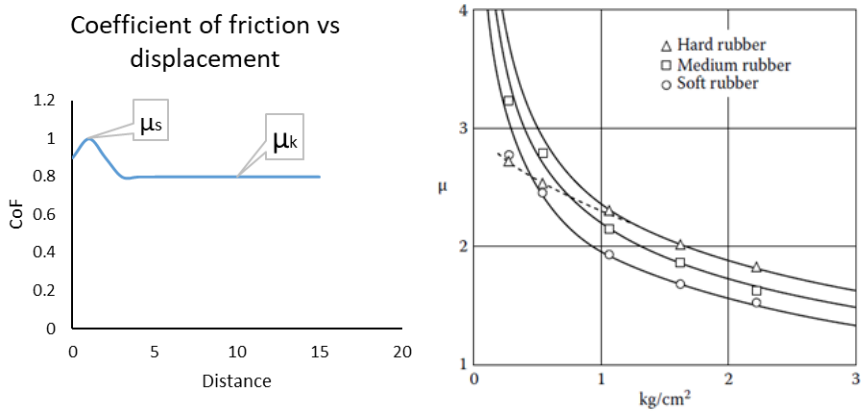

Fig. 2.28: Typical Coulomb friction behaviour separating the greater static value, compared to the lower kinetic value (left). The relationship between contact pressure and coefficient of friction for rubbers (right).

With a specific focus on elastomers as is the case in this thesis, there is a basic principle that was observed during the first laboratory-controlled tests to observe rubber friction behaviour: **Rubber friction coefficient decreases with increasing load** (Fig. 2.28-right). This holds true as long as there are no extraordinary events occurring such as tearing, extrusion, crack growth and seal failure.

Although this seems counterintuitive, it can be easily explained once the contributing factors for friction are considered:

- Normal force
- Contact area
- Surface roughness
- Temperature
- Speed
- Lubrication*

These factors are then compiled into what is known as: **The Unified Theory of Rubber Friction** [27] (Eq. 27).

$$\mu_{\text{Total}} = \mu_{\text{adhesion}} + \mu_{\text{hysteresis}} + \mu_{\text{viscous}} + \mu_{\text{cohesion}} \tag{27}$$

The theory splits the total frictional force into four contributing terms:

- The adhesion term: that stems from the bonding of polymer chains against the surface, influenced by the surface energy of the polymer and present when there is no lubrication.

- The deformation term: dependent on the localised strain of the rubber against the substrate, which is governed by the hysteretic behaviour of the material and the viscoelastic losses during dynamic deformation.
- Viscous term: comes from the shearing stresses required to slide the rubber on top of a layer of lubricant. This is not present on dry friction.
- Cohesion term: energy losses that stem from rubber wear and crack growth, and which is only present when there is a significant amount of material loss and/or crack propagation.

Viscous contributions stem mostly from the specific type of lubricant and its properties at the operating conditions. They do not reflect the specific elastomer properties as much as the other three. For that reason, it will not be covered in this particular investigation. Lastly, when there is no significant crack growth and the material does not wear significantly, which is often the case when there the number of cycles is low, the last term can be ignored. The focus of the current research is with the first two terms and how they vary under specific typical loading conditions.

It is important to start this review by explaining why an inverse relationship between rubber friction and applied pressure exists. If the example of sticky tape is used, this is clear. A small amount of sticky tape has almost no mass, yet the adhesion between the tape and the surface is quite high, in turn this can show a near infinite coefficient of friction. If extra weight is added on top of the tape (small dead weight) the friction forces will increase, but the relationship between the normal load against friction forces will decrease. It is this initial adhesion force that causes the observed inverse trend when it comes to rubber friction. It is simply how the balance of forces work when the rubber is moved in very low contact pressure environments (< 1 MPa).

2.9.2 The Adhesion Contribution to Friction

Although it may seem irrelevant, the adhesion between solid bodies is a (key) contributing force towards the totality of rubber frictional effects. First noted in 1946 by Thirion [28] when studying the frictional behaviour of two slabs of the same elastomer of different sizes but under the same pressure loads (Fig. 2.29 - left). Two key things were observed in the experiments; high velocity will cause chattering of the rubber against a smooth surface, so in order to produce repeatable results, the velocity needed to be reduced to 0.0176 cm/s. Secondly, the larger block of rubber had a much larger coefficient of friction for the same applied load.

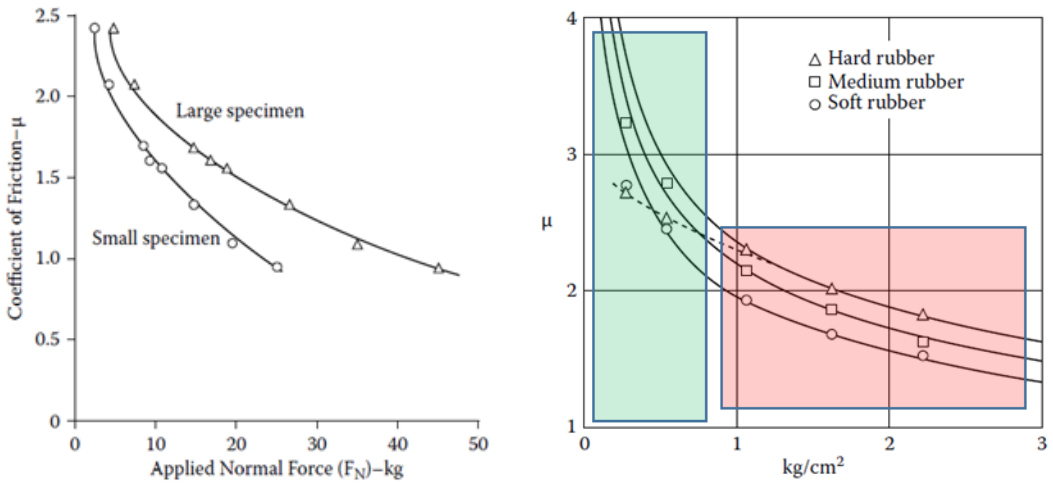

Fig. 2.29: Thirion's experiment of rubber friction against smooth glass (left). Coefficient of friction vs. Pressure load for different hardness rubbers. Highlighted in green is the adhesional friction dominant area, red zone represents the hysteretic friction dominant area. Modified from (right) [55].

Further research took place in 1952 by Schallamach [55]. He managed to relate the coefficient of friction to the total area of contact of the rubber. In order to avoid chattering at higher velocities, Schallamach roughened the elastomer surface before sliding against smooth glass and introduced the possibility that the friction force developed by rubber is proportional to the real area of contact against the surface.

Assuming that the glass surface is perfectly flat and that the rough rubber surface has an ideal shape of hemispheres, the Hertz equation [30] can be used to approximate the real area of contact. The original Hertz equation is:

$$A_{\mathrm{H}} = c_{\mathrm{m}}(F_{\mathrm{N}})^{\frac{2}{3}} \tag{28}$$

where A_{H} is the Hertz area of contact, c_{m} is the associated constant for the two materials involved (rubber and glass in this case) and F_{N} is the normal load. Assuming that the area of contact is directly related to the adhesional forces of the rubber, A_{H} can be replaced with μ once it is all divided by the contact area, Eq. 29 can be derived:

$$\mu = c_{\mathrm{A}}(\sigma_0)^{\mathrm{b}} \tag{29}$$

where c_{A} is a coefficient that depends on the velocity of displacement and the hardness of the rubber. A rubber with higher hardness will have a lower contact area since the ideal hemispheres will not deform as much, thus ending with lower area of contact and a lower effect of adhesional frictional forces (Fig. 2.29).

To understand the reasoning behind the surface area relationship, Schallamach proposed the idea that the polymer chains of the elastomer attach themselves to the surface asperities of the substrate. When movement begins, this chain is then stretched, and once the shear forces are greater than the adhesional forces on the chain, it detaches from the surface and reattaches to the next asperity. Fig. 2.30 depicts the effect of displacement on the elastomer chains. Time can also cause this movement due to stress relaxation and chain

reptation effects. This stick-slip type of motion is affected by velocity and temperature, and it is the cause of the chattering that is experienced at higher velocities of displacement. If the motion is slow, the chains can undergo reptation, eliminating the sudden jumps in the motion. When velocity increases, the chattering begins to happen until a point where extreme velocity causes the chains to float over the asperities and this reduce the friction.

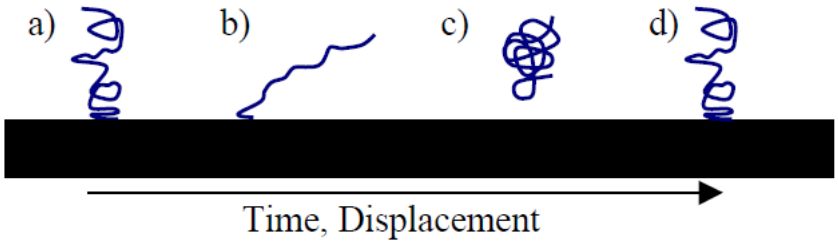

Fig. 2.30: Depiction of the chain motion against flat substrates. (a) The chain attaches itself to the surface, (b) stretching occurs in the same direction of displacement, (c) shear force overcomes the adhesive forces, (d) chain reattaches and the cycle restarts (adopted from [27]).

Because of this stick-slip type of movement, rubber friction experimental data against dry surfaces can be difficult to measure. Fig. 2.31 shows a pulley type system, similar to that of Leonardo da Vinci for a rubber sample.

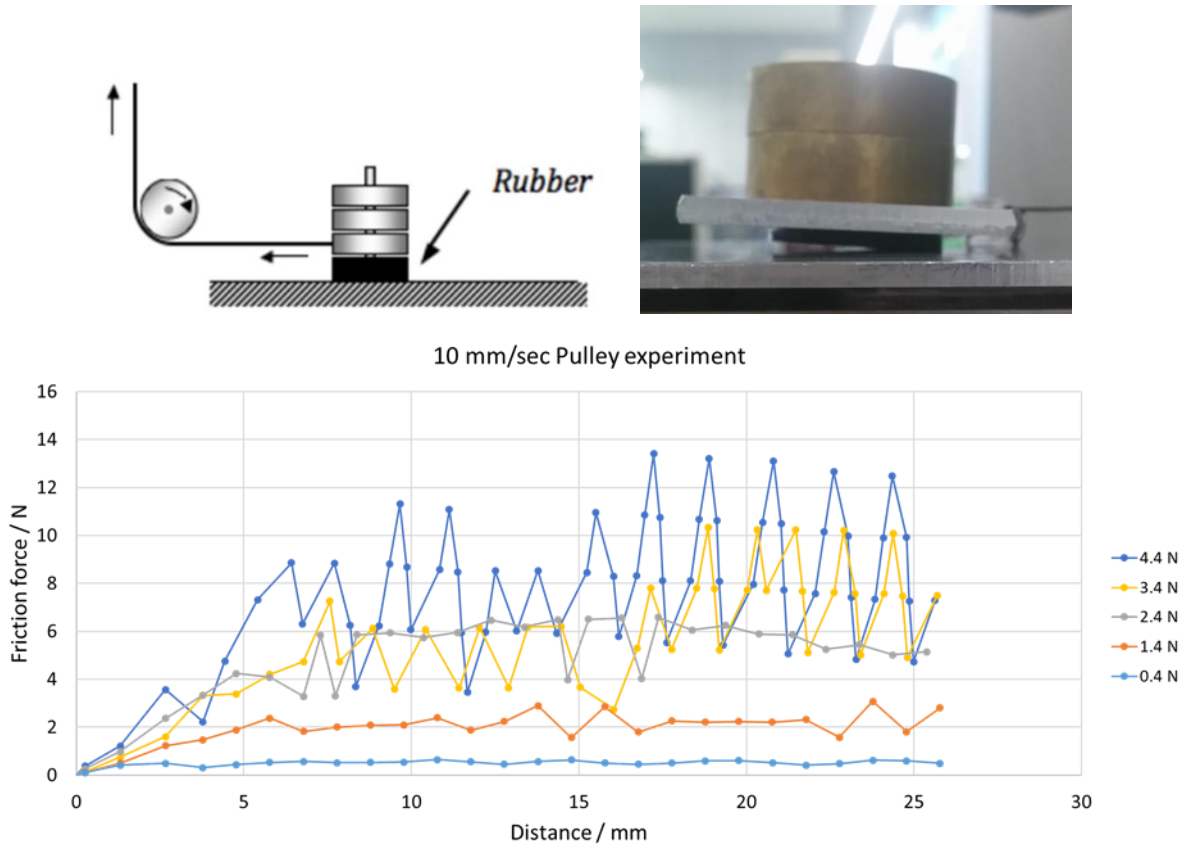

Fig. 2.31: Pulley system used for friction testing (top left). A pulley system being used on a rubber block. Notice the jumping of the sample as it moves. This makes it difficult to calculate contact area during motion (top right). Results for different normal loads on a pulley system of a rubber block. The force variability is very large (bottom).

The relationship between rubber friction and contact area is well established by now. For example, when seeking to maximise vehicle safety, car tyre designers focus on this aspect. Maximising the area of contact depends most significantly on the following three things:

- The nominal contact area.
- Lack of lubrication.
- Hardness of the elastomer.

The first one is simple. The real contact area is directly related to the nominal contact area, with the relationship depending upon the contact pressure and the detailed topography of the two interacting surfaces. The larger the nominal contact area then the more polymer chains will be able to attach themselves to the surface and higher friction is achieved. If one uses the example of Formula 1 tyres, the dry weather ones are known as slicks, and these are completely smooth. Lubrication that results in a boundary layer being formed across the interface nearly eliminates rubber adhesion. Fluid between the elastomer and the surface will stop the chains from attaching themselves to the surface. Using the same previous example, tyres that must operate under wet road condition must have small channels to allow water to be displaced away from the contact patch. Finally, the softer the elastomer is, the better it can deform into the detailed surface topography of the road surface, which creates a higher area of contact. Rubber tyres typically have a better grip if they use silica reinforcement instead of carbon black. A higher wear resistance, an ability to dissipate and conduct away any static charge and enhanced UV protection are all achieved by using carbon black particles as a filler material. These are the significant reasons for carbon black's continued use as a significant reinforcing filler in tyres, and it is not specifically about increasing the tyre friction.

2.9.3 The Hysteretic Contribution to Friction

When perfectly elastic materials are subject to deformation, the energy stored in them is fully recovered once the straining forces are removed. Because rubber has viscoelastic behaviour, some of this energy is dissipated, being released as heat and this energy dissipation is one of the largest contributors to rubber friction. This energy that has been dissipated from straining and relaxing the material is known as the hysteresis loss [32]. A way of illustrating this is presented in Fig. 2.32, where a common uniaxial strain is placed on an elastomer, the sample is then returned to its original length. The area that lays between the curves is a measure of the as the hysteretic loss.

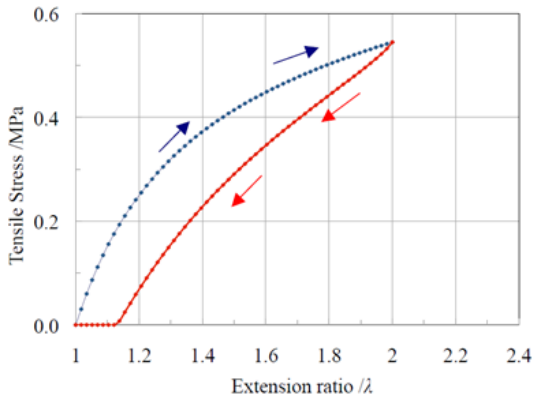

Fig. 2.32: Description of the typical stress-strain response of a cycle of deformation for rubber. The area between the curves is what is known as the hysteretic loss.

To help understand viscoelastic behaviour during cyclic loading, the concept of dynamic mechanical modulus can be used. A complex elastic tensile modulus known as E^* is what determines the response to dynamic loading. This modulus is defined by:

$$|E^*| = \sqrt[2]{E'^2 + E''^2} \tag{30}$$

where E' is the elastic storage modulus, a measure of the elastically stored energy during the deformation, and E'' is a measure of the out of phase energy that is dissipated or converted into heat. To calculate the magnitude of the complex conjugate E^*, it is possible to adopt a Pythagoras approach to derive the absolute value $|E^*|$. Let us call the angle that is formed between E^* and E' as δ so that E'' divided by E' is tan δ. This tan δ value is of great importance to the understanding of rubber viscoelastic behaviour since it can determine the ratio of loss energy during cyclic deformation at different frequencies. Frequency dependent deformation is important because of its relation to sliding velocity and surface topography.

All surfaces, even those that appear optically smooth, contribute to rubber friction by small local deformations generated by the asperities in the contact area. These small local deformations are then returned to their original unstrained state and energy is dissipated. This dissipation of energy contributes to losses of energy that are transmitted into the system and thus, affects the work negatively, countering the sliding motion. Fig. 2.33 illustrates a case where a rubber block slides on top of small rocks to better demonstrate the effects of surface roughness.

Whenever a rubber surface encounters a small bump in the more rigid surface, there is a local deformation. As the rubber moves forward, the small section once again relaxes, and energy losses arise. The process repeats with every surface bump in the way of the rubber and the total amount of energy loss becomes significant [33]. Statistically speaking, surfaces can be measured to determine their topological features such as the average width. When it comes to these small bumps, making it easier to speak in terms of frequency of

deformation rather than in velocity of motion. Frequency is easily translatable between surfaces of different roughness, whereas velocity is not. To fully explore the friction behaviour, it is necessary to characterise the dynamic behaviour of the rubber using for example a dynamic mechanical analyser (DMA) to predict the viscoelastic losses at different frequencies and at different temperatures.

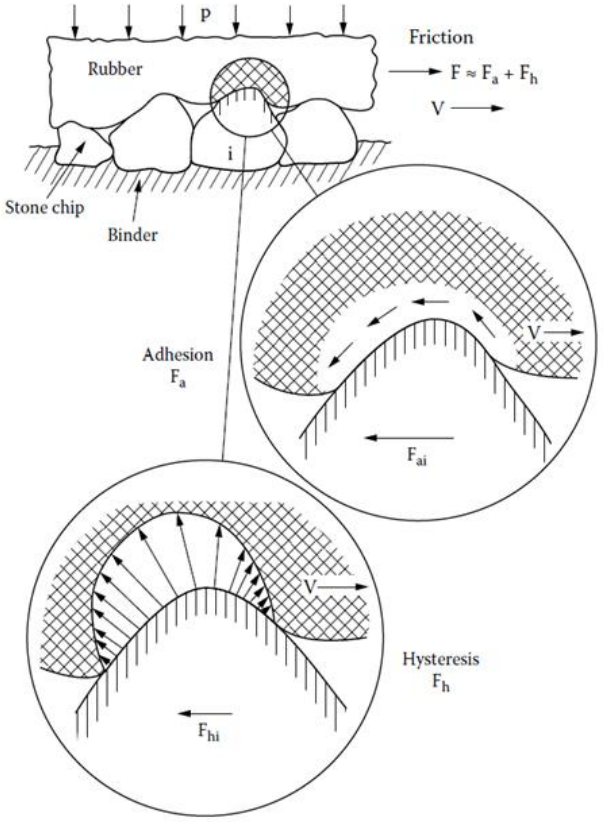

Fig. 2.33: Description of the rubber moving through the asperities in a surface. Contributions from adhesion and hysteretic friction are describe as F_a and F_h. Localised contact area, and the small section of rubber deformed where the hysteretic energy losses occur are observed. (Adopted from [33]).

Studying the surface roughness is key for both hysteresis and adhesion terms. A complete surface roughness study should provide us with two very important variables:

- Peak to valley distance.
- Wavelength magnitude.

Once these are obtained, we can know the local strain values and the frequency of these deformations. Since viscoelastic properties are significantly affected by the strain rate, frictional behaviour of rubber is highly dependent on sliding velocity for the hysteretic term.

Whilst lubrication practically eliminates the adhesion component, the hysteretic component remains present. Effects like layers of liquid between the rubber and the roughness peaks, or the pockets of lubricant formed in the valleys that will not allow the rubber to fill into the gap completely do exist, but overall hysteretic friction is the main

contributing factor during wet contact. The friction contribution will be almost exactly equal to the viscoelastic loss in the elastomer at the frequency of deformation.

We understand that these viscoelastic losses are related to the magnitude of the loss modulus, which is in turn related to tan δ, which is related to frequency (w), $F_{\mathrm{h}} \propto \tan(\delta)$. Under these conditions it is possible to understand the balance of the major contributions to rubber friction. A smooth surface would yield lower hysteresis losses but greater adhesion, whereas a roughened surface diminishes the real contact area but increases the local deformation of the elastomer and the hysteresis losses. In the following chapter, we will observe some effects of rubber sliding velocity under lubricated conditions at different speeds to better understand the effects of deformation frequency.

2.9.4 Modern Theories of Rubber Friction

For roughly 2 decades, since the 1998 Persson paper [33], two main quantitative theories have dominated the study of rubber friction: those of Klüppel and Heinrich [35] and Persson [37], developed about one year apart from each other. Both have one thing in common. They concentrate on the multiscale nature of surfaces and their fractal roughness [38].

Persson's theory quantifies the surface roughness scale using power spectrum density (PSD), and the values come mostly from two contributing elements. The cut-off wavelength q_1, which comes from the PSD analysis, is selected by the value of the cumulative root mean squared (RMS or Rq) slope [39]. The other contributing factor is the mechanical behaviour of the rubber depending on the frequency of deformation (in radians). Persson's equation for the hysteretic contribution is presented in Eq. 31:

$$\mu_{\mathrm{hyst}} = \frac{1}{2}\int_{q_0}^{q_1} q^3 C(q) S(q) P(q)\mathrm{d}q \times \int_0^{2\pi} \cos(\phi) * \mathrm{Im}\left(\frac{E(qV\cos(\phi))}{(1-\nu^2)\sigma_0}\right)\mathrm{d}\phi \qquad (31)$$

where q is the wavenumber with q_0 being the roll-off wavenumber and q_1 the cut-off wavenumber for the surface roughness level used, whether it is micro-roughness or macro-roughness. E is the elastic modulus, V is the sliding velocity, ν is the Poisson's ratio, and σ_0 is the apparent contact pressure, defined as normal force over contact area ($F_{\mathrm{o}}/A_{\mathrm{o}}$). The first integral deals with the effects of the contact mechanics, with $C(q)$ as the surface PSD, $S(q)$ a correction factor for elastic contact and $P(q)$ the real contact area to apparent contact area ratio. The following relations apply:

$$P(q) = \mathrm{erf}\left(\frac{1}{2\sqrt{G(q)}}\right) \qquad (32)$$

$$G(q) = \frac{1}{8}\int_{q_0}^{q} q^3 C(q)\mathrm{d}q \times \int_0^{2\pi} \left|\frac{E(qV\cos(\phi)}{(1-\nu^2)\sigma_0}\right|^2 \mathrm{d}\phi \qquad (33)$$

$$S(q) = \gamma + (1-\gamma)P(q)^2 \qquad (34)$$

where γ is an elastic deformation empirical constant (≈0.5). The selection of both $q_0$and q_1

can be seen as arbitrary sometimes since they depend on variables such as the equipment resolution and the maximum wavelength that should be used for a specific surface.

Klüppel's theory for the hysteretic contribution of friction uses the height difference correlation (HDC) function instead of the PSD in order to determine the contact area and deformation rate of the rubber. Eq. 35 shows the hysteretic contribution of rubber friction, which is very similar to that of Persson, but Klüppel's theory describes the layer of rubber that actually undergoes deformation with the term z_{p}. $S(\omega)$ is the power spectral density based on the quantities determined by HDC.

$$\mu_{\mathrm{hyst}} = \frac{1}{2(2\pi)^2} \frac{<z_{\mathrm{p}}>}{\sigma_0 V} \int E''(\omega) \cdot S(\omega) \mathrm{d}\omega \tag{35}$$

In terms of the adhesion contribution, Persson has developed two models that describe the behaviour of adhesion on hard substrates. The first one is the crack opening model [40]. In this model, he applies an energetics approach to determine the energy required to advance a fracture plane by one unit area, calling this term the effective energy, or γ_{eff}. This is directly proportional to the ratio of the elastic modulus of the rubber in the glassy state compared to the rubbery state. If we look at Fig. 2.34, we can see how the crack of the rubber moves along in the material. At the very tip of the crack, movement is very rapid at high frequencies and characterised by a high frequency modulus E_∞. It then passes through the complex viscoelastic modulus (E_{w}) zone, and finally through the zero-frequency modulus zone, represented with E_0.

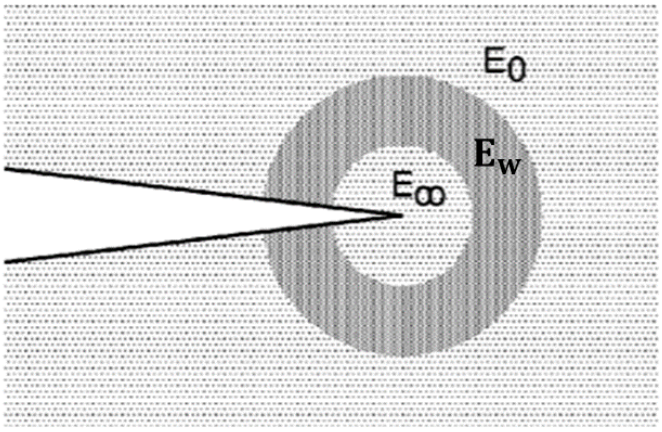

Fig. 2.34: An advancing crack tip and diagram describing all three zones of rubber behaviour. (Adopted from [40]).

With this effective energy, Persson relates the separation of a rubber and a substrate as a crack between the two.

$$\gamma_{\mathrm{eff}} = \frac{\gamma_0 E_\infty}{E_0} \tag{36}$$

$$\mu_{\mathrm{adh}} = \frac{\Delta\gamma_{\mathrm{eff}}(V) P(q)}{\sigma_o l} \tag{37}$$

$$\frac{\Delta\gamma_{\mathrm{eff}}(V)}{\Delta\gamma} = \left[1 - \frac{2}{\pi} E(0) \int_0^{\frac{2\pi V}{r(V)}} \frac{F(\omega)}{\omega} \mathrm{Im}\left(\frac{1}{E(\omega a_{\mathrm{T}})}\right) \mathrm{d}\omega\right]^{-1} \tag{38}$$

where $r(V)$ and $r(0)$ are respectively the tip radius for a crack moving at the sliding velocity V and the tip radius of a very slowly moving crack. l is the minimum contact length, that is the wavelength at the largest q (q_1). These values could be obtained with crack growth experiments, but this is beyond the scope of this work. They are derived using values taken from the literature.

$$\frac{r(V)}{r(0)} = \frac{\Delta\gamma_{\text{eff}}(V)}{\Delta\gamma} \tag{39}$$

The second theory of frictional adhesion comes from a collaboration between Tiwari and Persson [41]. It denotes the effects of a shearing transfer film between the rubber and the substrate. This only happens at very high speeds. Since this is not encountered in our applications, it was considered beyond the scope of our research.

The Klüppel theory of adhesion is examined from the perspective of interfacial shear strength. When the rate of movement is very small, the interfacial energy corresponds to the static surface energy [42]. As we increase the rate of separation, surface energy $\Delta\gamma_{\text{eff}}$ follows a power law relationship until the critical velocity V_{c}. This critical velocity is the velocity of maximum adhesion friction. Interfacial shear strength is then related to surface energy. Eq. 40 shows the shear strength behaviour.

$$\tau_{\text{s}}(V) = \tau_{\text{s,0}}\left(1 + \frac{E_\infty/E_0}{(1+V_{\text{c}}/V)^n}\right) \tag{40}$$

τ_{s} is the true interfacial shear strength, n is a material dependent exponent ($0.7 < n < 1$), $\tau_{\text{s,0}}$ is the shear strength at the limit of very low velocities, and E_∞/E_0 is the ratio of the elastic modulus at high rate of deformation, divided by the modulus at very slow speeds of deformation. Once the shear strength is obtained, the contribution from adhesion μ_{adh} is determined by:

$$\mu_{\text{adh}} = \frac{\tau_{\text{s}}}{\sigma_{\text{z}}} \cdot P(q) \tag{41}$$

Where σ_z is the pressure acting on the moving body, perpendicular to the movement trajectory. All these theories were mostly directed toward understanding tyre friction, where velocity is one of the most important elements of study. For static sealing elements, the sliding velocity is typically much slower than that encountered in tyre applications. Dynamic seals, however, can reach these higher sliding velocities depending on their application.

2.10 Tribology

If an object is placed on top of a surface, when observing the surface interaction from the macro-scale, the contact area can simply be considered as a two-dimensional projection of the shape touching the surface. Under closer examination, the object in question only contacts the surface at certain key points. With an even closer look, those key points are a

collection of even smaller contact points that separate the object from the surface.

When seals are being considered then the real contact area becomes the barrier between two zones that are meant to be isolated from each other. If there is a channel between these zones, then a leak occurs[87]. In addition to this well-known behaviour, contact area studies have a particular interest to the study of rubber friction. For example, when a rubber slides across any other surface, there exists a local deformation that changes the mechanical and adhesional behaviour of the rubber [37]. To model the friction occurring between two surfaces, the real contact area is required to fully understand the influence of the adhesional component of the friction and the local deformation. One of earliest models that was derived for solid contact mechanics is the Hertz theory. Developed by H. Hertz in the 1880 [30], where the assumption is that interacting surfaces can be represented as two spherical asperities of different size and modulus, that are both smooth and elastic.

Using the Hertz theory to analyse the contact a sphere generates when pressed against an infinitely large flat body, we obtain Eq. 42. Where A_c is the contact area of the circle profile that is formed by the sphere of radius a, modulus E_2(shown in figure 2.35) that deforms the solid a distance h after coming into contact with the elastic solid of E_1 modulus. When approaching the contact between rubbers and stiff materials such as steel and asphalt, the value of E_1 is much smaller than E_2, this can simplify the approximation of h into Eq. 43

$$A_c = \pi R h \tag{42}$$

$$h = R^{-\frac{1}{3}} \left(\frac{\frac{9}{16} F_n}{E_1} \right)^{\frac{2}{3}} \tag{43}$$

From this equation, the real contact area between the two spheres has a $F_n^{2/3}$ load dependence. This expression conveniently demonstrates (assuming that the contact area is proportional to frictional force) that the coefficient of friction does not increase linearly with the applied normal force.

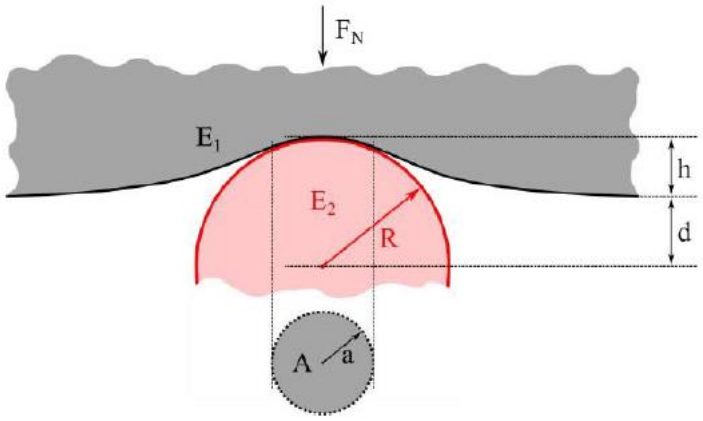

Figure 2.35: Hertz theory of contact area. The elastic solid of E_1 modulus is deformed by the sphere of E_2

modulus. With the distance h known, the area of the circle-shaped contact zone can be determined (taken from [36])

Hertzian theory assumes contact from ideal spheres at the same height profile, which is unrealistic. In the 60s, Greenwood & Williamson(figure 2.36) came up with a modification for this theory, they would [88] still assume the Hertz theory of a surface made up of small spheres. In this case, the height of the spheres would follow a Gaussian distribution across the mean height of the profile. This model can describe the contact between surfaces at low squeezing-pressure levels, most real surfaces are made of materials with multiple decades of length scale.

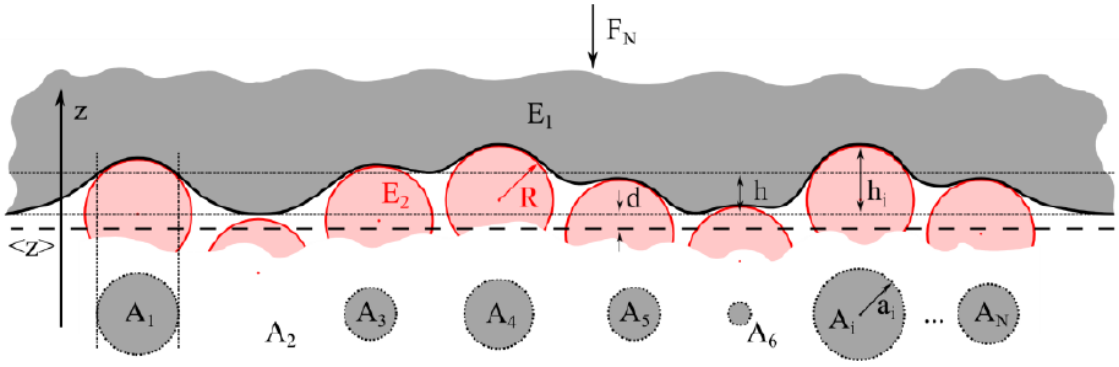

Figure 2.36: Greenwood & Williamson theory where the Hertz theory is applied to a Gaussian distribution of spherical deformities coming into contact with the surface (taken from [36])

The assumption of spherical surfaces does not provide a realistic match to most surface topographies that often exhibit fractal-like surfaces. To account for roughness on all relevant scales, two possible theories of surface roughness descriptions are used. Surface roughness power spectrum $C(q)$ and height difference correlation function. These methods are explained in this chapter.

When studying friction theories, the adhesional component is governed by the real area of contact between the surfaces. The energy loss component is controlled by the local deformations of the rubber when it slides against the surface. These deformations are controlled by a relationship between the sliding (or slip) velocity between the surfaces and a characteristic horizontal length in the plane of the surface geometry. The dimension of this variable is known as the cut-off length. When considering the roughness or coarseness of a particular surface, then asphalt and granite are at the higher end of the scale, with polished steel, glass and surfaces with smooth coatings at the other end. Even with this difference in the coarseness scale, there is also the difference in the sharpness of any given asperity. A common mistake when describing the contact surface geometry is to confuse roughness with the “sharpness” of the surface, as can be identified from the ratio of vertical to horizontal descriptors of the surface as shown in Fig. 2.37. This investigation adopts two separate methods of analysing the surface roughness. Each has a specific application in practice when it comes to simulating friction behaviour. Both methods can describe the

Hurst-exponent H, which is simply a measure of the surface irregularity. Surfaces can also be self-affine, meaning that the aspect of the roughness remains the same at a macro or micro scale (Fig. 2.38). The Hurst-exponent can then be linked to the fractal dimension D, which observes how a surface topography can change dependent upon the scale at which it is measured [44].

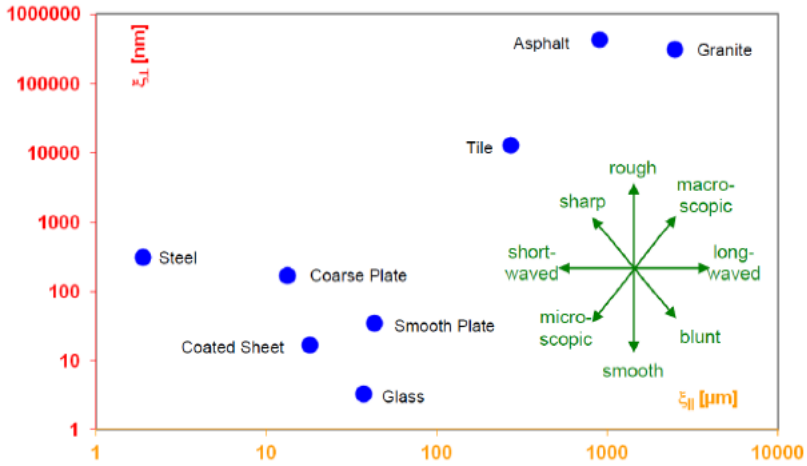

Fig. 2.37: Horizontal ($\xi_{\parallel}$) vs vertical ($\xi_{\perp}$) cut-off lengths for different surfaces. (Adapted from [43]).

The first methodology is known as the height difference correlation (HDC) function, which analyses the horizontal ($\xi_{\parallel}$) and vertical ($\xi_{\perp}$) cut-off lengths using Eq. 2.10.1. This method is commonly used for random surface characterisation such as roads or chemically abraded surfaces [45][28]. HDC function equation is presented as:

$$C(\lambda) =< (z(x+\lambda) - z(x))^2 > \tag{44}$$

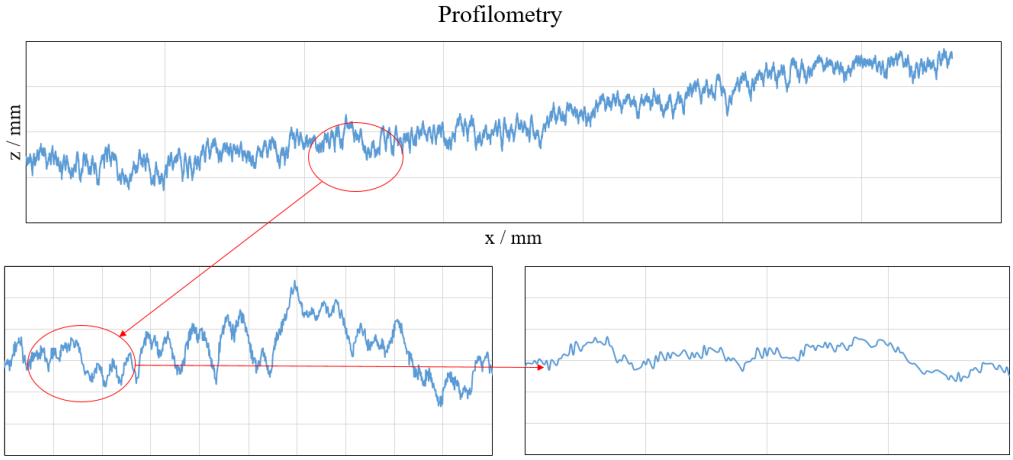

Fig. 2.38: A self-affine surface showing the similarities at different scales of the same surface.

where z is the height of the surface profile along a horizontal position x. λ gives the horizontal distance between the points observed as shown in Fig. 2.39. The results are averaged and λ is further increased. Eq. 44 evaluates the height profile $z(x)$ by evaluating the average square ($< \cdots >$) height difference for different horizontal wavelengths. For self-affine surfaces, the function $C_{\mathrm{HDC}}(\lambda)$ can be described using Eq. 45:

$$C_{\mathrm{HDC}}(\lambda) = {\xi_{\perp}}^2 \left(\frac{\lambda}{\xi_{\parallel}}\right)^{2H} \tag{45}$$

When the $C(\lambda)$ versus λ is plotted on a log-log graph, the slope of the curve before the plateau is related to the Hurst parameter H by a factor of 2. Fig. 2.40 denotes the change from surface analysis to the cut-off lengths estimation and procedure to calculate the $C(\lambda)$.

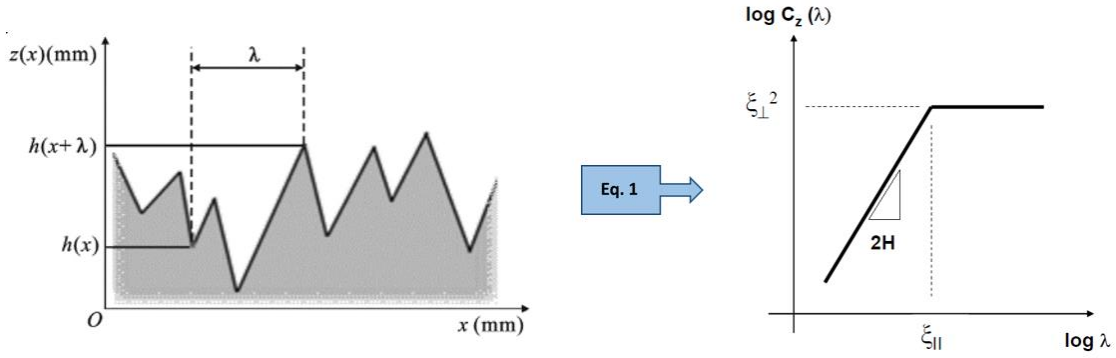

Fig. 2.39: Objective of the HDC to translate a surface profile into characteristic parameters.

An initial value of lambda (λ) is used and the difference in vertical value (z) is calculated. As we increase λ the separation of the wavelength and the separation of vertical value z increases. There will come a point, where this change stops, where the average height of the peaks does not change with increasing wavelength. The moment this value tapers off is the one we are interested in to determine the cut-off lengths. Figure 2.41 shows the typical output of an HDC analysis.

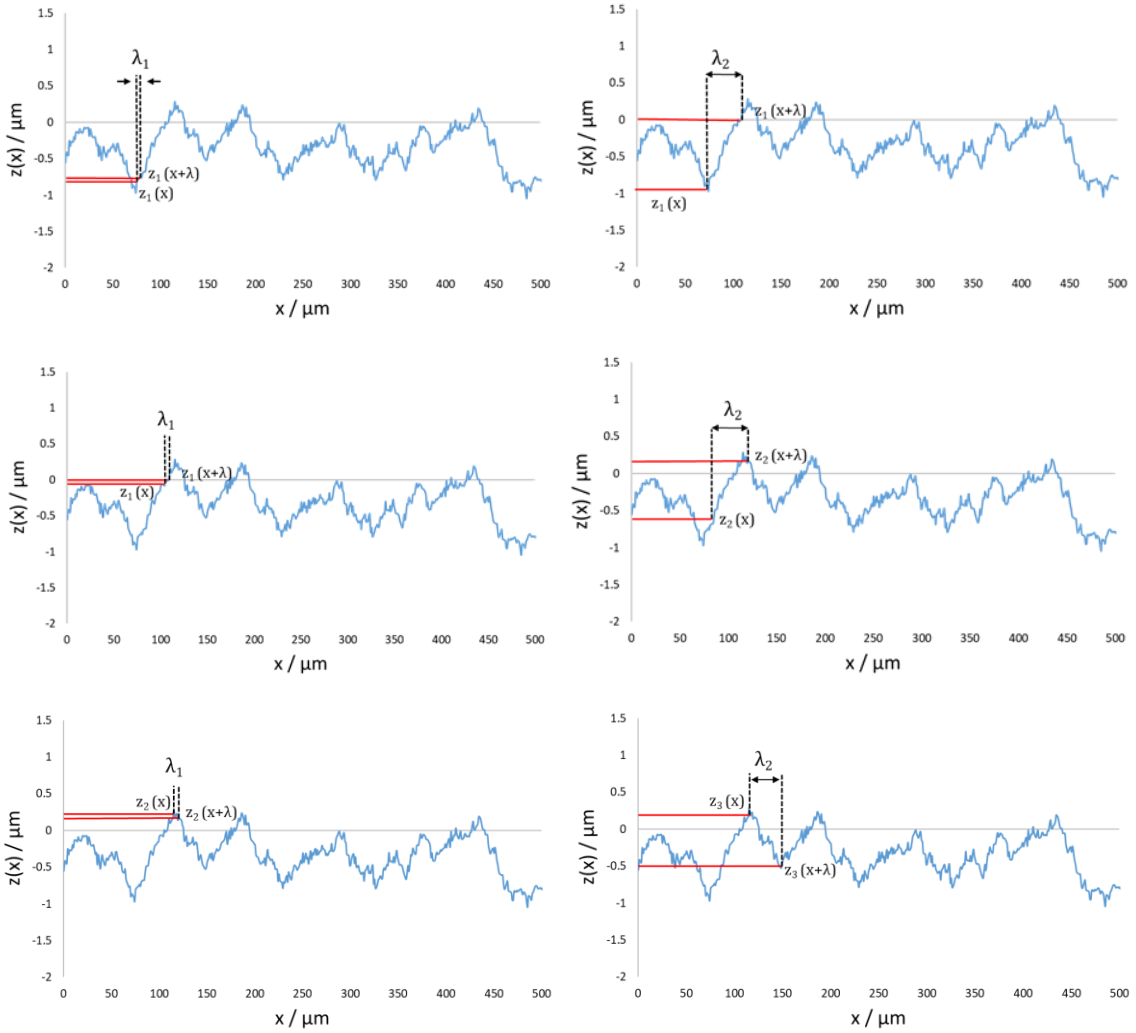

Fig. 2.40: Raw data from piston profilometry analysed with HDC function. Left side shows the first lambda to be used for analysis across the *x*-axis. Right side increases the lambda and repeats the previous step. The average square for these changes is stored in the C_{HDC} function

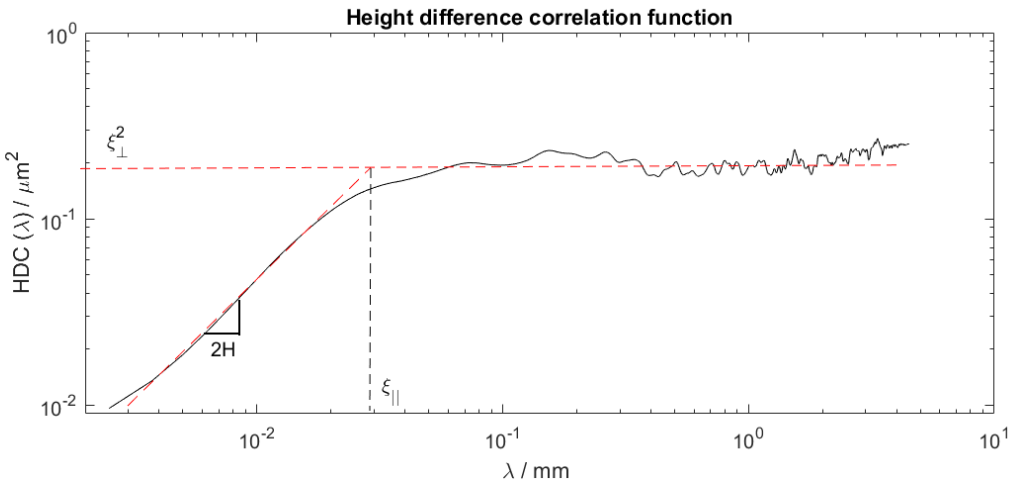

Figure 2.41: The relationship between the height difference correlation function, HDC versus the lambda, λ, value. The slope of the initial function provides the Hurst exponent, and the plateau region provides the vertical and horizontal descriptions of the surface.

The second method to characterise surface roughness is the Power Spectrum Density (PSD) method. The technique tries to match surface roughness profiles using sinusoidal waves with different amplitudes ($h(x)$) and different wavelengths (λ)(figure 2.42) [37].

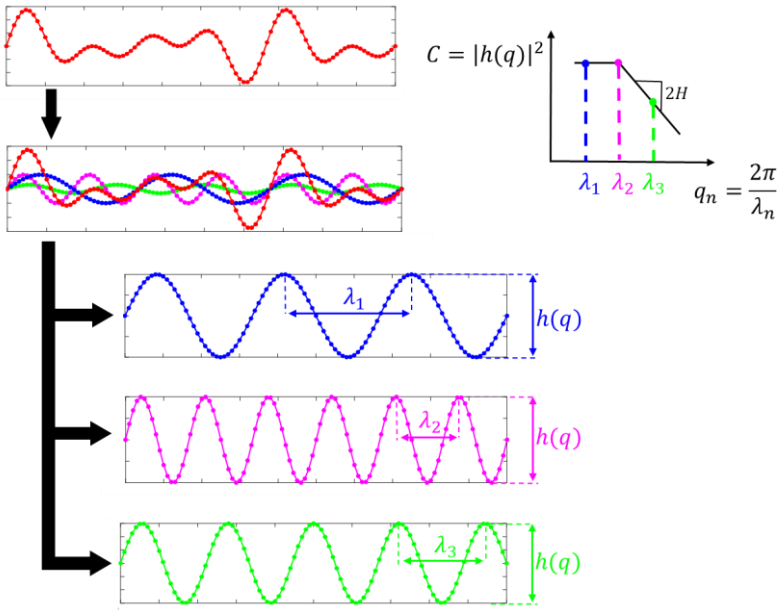

Figure 2.42: Breakdown of the power spectrum density (PSD) method. The surface roughness is broken down into smaller waveforms and waveform properties plotted.

If instead of using wavelengths, we use wavenumbers q ($q = 2\pi/\lambda$), and we define the power spectrum density $C(q)$ as the square of the amplitude $h(q)$ (Eq. 46), then we can observe the surface profile by plotting $C(q)$ versus q (Fig. 2.43).

$$C(q) = |h(q)|^2 \tag{46}$$

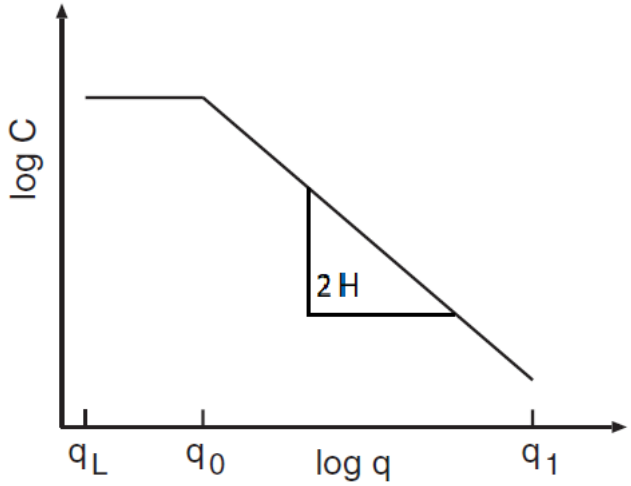

Fig. 2.43: PSD for a self-affine surface. The slope of the log (C) versus log (q) plot between q_0 and q_1 determines the Hurst exponent of the surface. (Modified from [47]).

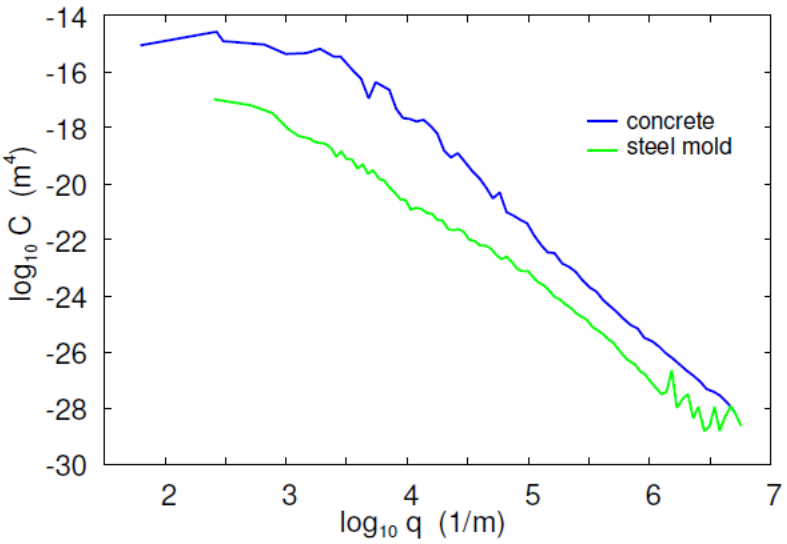

Figure 2.44: PSD analysis of concrete surfaces and a steel mold. Taken from [41]

Once we obtain the characteristic value of the wavenumber for the surface and the $C(q)$, we can describe the horizontal and vertical cut-off lengths of the surface. Given that a surface can have multiple roughness scales, there can be several cut-off wavenumbers ($q_0, q_1, q_2 \dots q_n$). The PSD function describes the surface between these values. These approaches are used in this work to characterise the surface roughness of different surfaces encountered during investigations, such as concrete or steel moulds (figure 2.44).

Although these methods can help us determine the surface roughness, it is also important to adapt seals to the roughness of the surface to avoid percolation. For seals to fail, there must be a channel of fluid that connects both sides through the seal, causing leakage. The point where said channel is big enough for leakage, is called the percolation threshold. To predict gaps where fluid channels could form, the topography of the surface is identified and then models can be done to predict the contact patches against the surface[96].

Figure 2.45 denotes the difference between channels formed in a rubber pressed against a surface. If there is a channel of non-contact that goes through the entire distance of the seal, then leakage occurs.

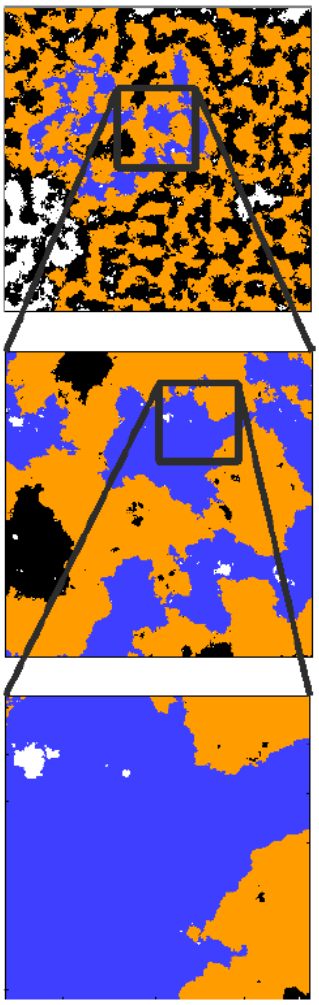

Fig 2.45: Surface with H = 0.8 contact and noncontact patches. Black denotes regular contact, with blue representing the largest connected contact patch. White and orange are similarly representing noncontact or open channels. Taken from [96]

Models of contact regions versus non-contact regions are severely affected by the selection of the wavelength number (q) as shown in figure 2.46. Higher wavelength numbers are related to smaller distances between the surface peaks. This means that sharper peaks will deform the rubber and it becomes more difficult for the rubber to smoothly cover all the surface. For these rougher surfaces, the real contact area is a lot smaller than the nominal, increasing the risk of the seal reaching the percolation threshold and causing leakage.

A second effect that occurs for these non-contact areas is that trapped fluid is present between the surface of the seal and the substrate. When these thin fluid films are exposed to higher pressures, two things occur: firstly, the lubricant viscosity increases, secondly, this flattens the contacting surface when elastically deformed, causing elasto-hydrodynamic lubrication.

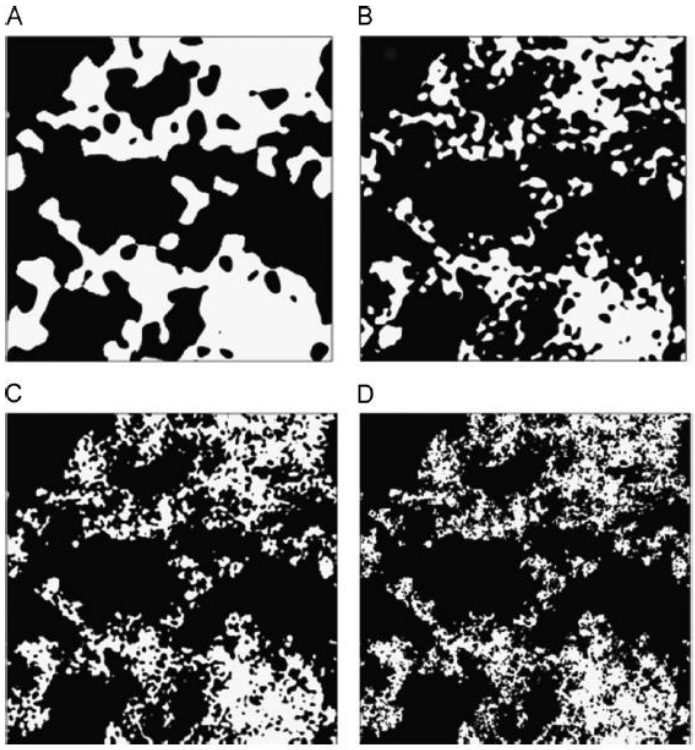

Fig 2.46: Contact regions (white areas) for H= 0.85 and wavelength numbers (A) = 16, $\frac{A}{A_0} = 0.45$, (B) = 32, $\frac{A}{A_0} = 0.42$, (A) = 64, $\frac{A}{A_0} = 0.39$, (A) = 128, $\frac{A}{A_0} = 0.37$. Taken from [97]

If the lubricant layer is squeezed to a point where the thickness of the film is down to a few nanometers, the friction behaviour will change from thin layer lubrication to dry friction[98].

All the previously mentioned variables and conditions (surface roughness, viscoelastic behaviour, lubricating layers) make rubber friction prediction extremely difficult to model. Even with modern models, the are aspects of it that need arbitrary selection of parameters (such as wavelength, base friction) that can not be obtained without careful friction testing.

Along with temperature and pressure dependency, there needs to be experimental constant that can fully describe frictional behaviour. Without proper testing, this is not possible, and currently, there are no “off the shelf” solutions for high pressure and high temperature friction characterisation. Highly demanding environments still require good sealing performance. These seals are sought after in different industries, such as automotive, aerospace and energy.

Testing the validity of these theoretical concepts on and models is commonly done in the tyre industry, not much of the research is directed to machined and highly polished surfaces. In order to fill the gap in knowledge of these conditions, the current project looks develop a novel method of frictional testing and model validation.

The new method must adapt to what equipment is commonly found in industrial testing facilities (environmental chambers, tension testing equipment) and rubber products. Besides the rig itself, no custom equipment is to be used. The rig must adapt to

commercially available options. This holds true not only in terms of connections to pressure and force sensors, but O-rings and adapters as well.

Although rig design is of great importance, tests can only be validated if good material characterisation is at hand. All friction models mentioned in the chapter require the knowledge of mechanical behaviour (both in the dynamic and static conditions) and how they change with measures of other variables (pressure and temperature). Variables which are carefully selected to achieve a proper description of the frictional behaviour of the material during its service conditions. This characterisation is described in chapter 3.

3. Material Characterisation

All the O-rings used for these experiments were made from commercially available materials. Parker supplied O-ring type seals for the friction tests along with 2 mm thick flat sheets and 28mm diameter, 13mm height compression buttons for characterisation. This friction study used two different base polymer materials, HNBR and FKM, which are explained in more detail in Chapter 2. Both rubbers were also studied using two different levels of hardness, 75 and 90 Shore A. Hardness levels were verified with a Sauter durometer. Finite element analysis (FEA) is an essential part of our study in order to understand the contact area and pressure in the test rig. Therefore, it was essential to characterise the stress strain behaviour for all four materials. This behaviour was characterised using stored energy function and to generate the input data, the uniaxial behaviour of the rubber had to be measured accurately.

3.1 Mechanical Properties

Sample preparation was carried out following the ASTM D412 tensile test procedure. The rubber sheets were cut using a type D die. Buttons came in accordance with ASTM D575 norm for compression testing. The characterisation of the mechanical properties of the elastomer was performed using an Instron 5900R84 fitted with a 500N load cell. Quasi-static tension and compression tests were made using dumbbell shaped samples and cylindrical buttons, respectively. To check for hardness, a manual measurement of each compound was done using a Zwick durometer and following ASTM D2240. Three hardness measurements are done on the flat sheets of material, and the average is presented. During tensile testing, a 1% strain per second speed was used to ensure no influence from strain dependent effect. Sample gripping was done with pneumatic clamps, the strain data was obtained using a video-extensometer which ensured that grip slippage did not influence the data acquisition. Even though video-extensometers can account for slippage in the grips, all samples reached failure before any form of slipping occurred.

Table 3.1: Shore A hardness values for all elastomer compounds.

Rubber	**Shore A value**
HNBR 75	75.33
HNBR 90	90.66
FKM 75	75.0
FKM 90	89.33

Table 3.1 shows good agreement with customer specifications, in order to avoid much

variance between different O-rings, it was requested that all the O-rings (withing a same type and hardness) came from the same mixing batch. This is probably the reason for the good repeatability of the tests.

Figs. 3.1 and 3.2 show the stress-strain behaviour of all rubbers at three different test temperatures, 20, 60 and $120°C$. Unfilled rubbers tend to get stiffer as temperature is increased. With higher temperatures, entropy increases, and chain become stiffer. When it comes to filled rubbers, there is a breakdown of the filler network that comes with increasing temperature, this could be caused by a thermal expansion of the matrix. Both of these effects compete with each other, in more highly filled rubbers, the breakdown of the filler network tends to dominate, decreasing the stiffness. For the case of HNBR 75, both factors cancel each other out and the mechanical response of the rubber is near identical at the lowest and highest temperature, with only a small decrease at 60°C.

Temperature selection revolved around three different reasoning points: room temperature (20°C), maximum working temperature for a lot of oilfield working tools (120°C) and a midpoint that can show a trend between these two, whilst still being low enough to perform experiments with low-risk conditions (60°C). It is common in industry to describe rubbers by their elastic modulus (Young's modulus or E) and their ultimate tensile strength (σ_{UTS}).

The first one simply describes the relation between stress and strain in a linear fashion, this is very unrealistic for filled rubbers, since filler network breakdown causes a non-linear tension behaviour. Because of this, the "Elastic" region is only taken for the first 10% strain level, where the filler network is broadly still intact.

The second one is simply the stress at which the sample fails during the test, this is typically used to limit the strain/stress the component is used at during applications.

Once all the uniaxial data is obtained, we can use the Abaqus curve fitting tool to translate the material mechanical behaviour into a strain energy function (SEF) instead of the typical industry parameters. SEFs are a much better descriptor of rubber's mechanical behaviour. Abaqus allows us to select the best possible fitting model. An example of this fitting procedure is shown in Fig. 3.3.

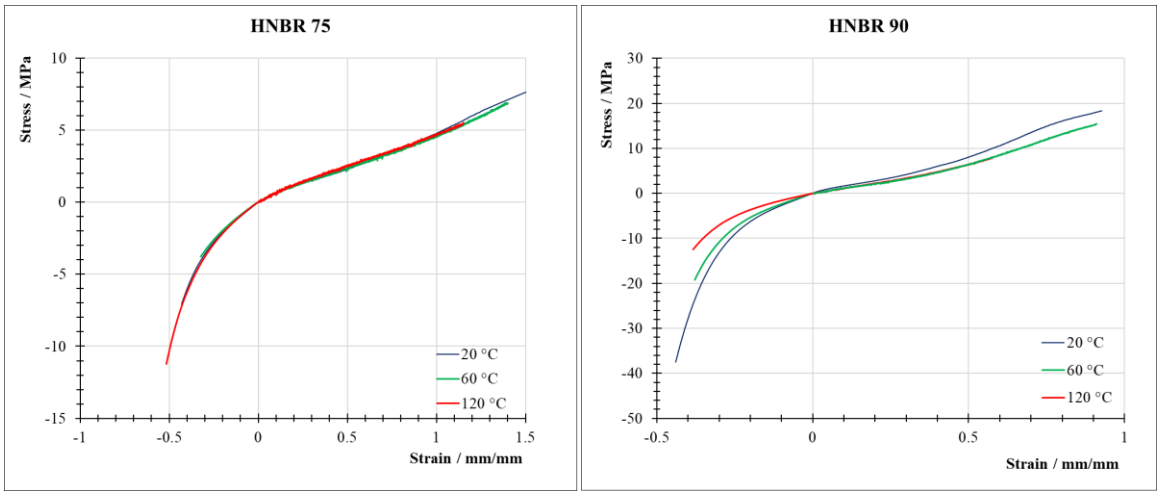

Fig. 3.1: Stress-Strain curves for uniaxial tension and compression in HNBR rubbers. HNBR 75 (left) and HNBR 90 (right).

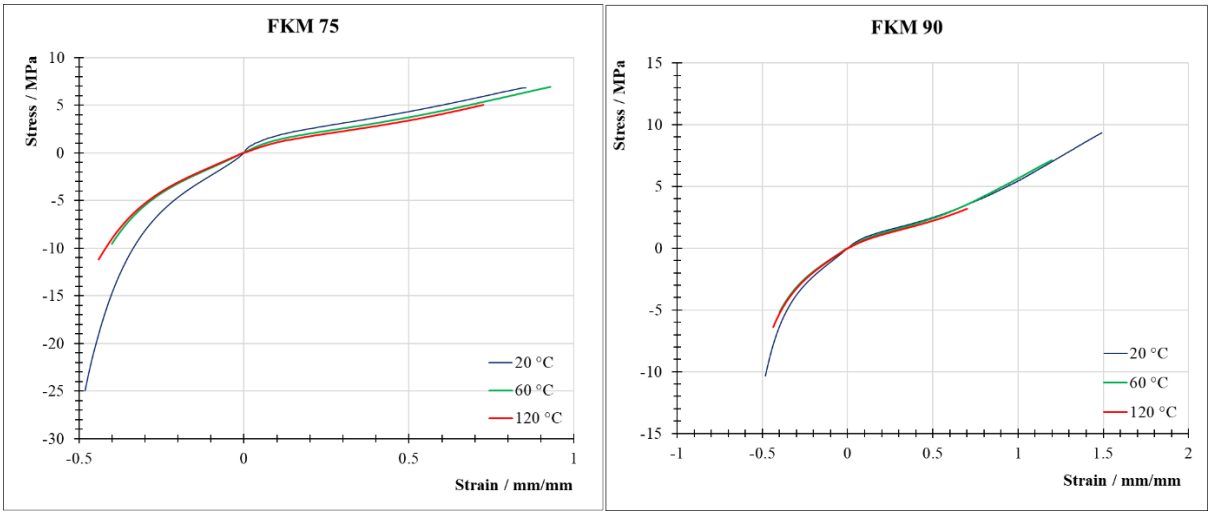

Fig. 3.2: Stress-Strain curves for uniaxial tension and compression in FKM rubbers. FKM 75 (left) and FKM 90 (right).

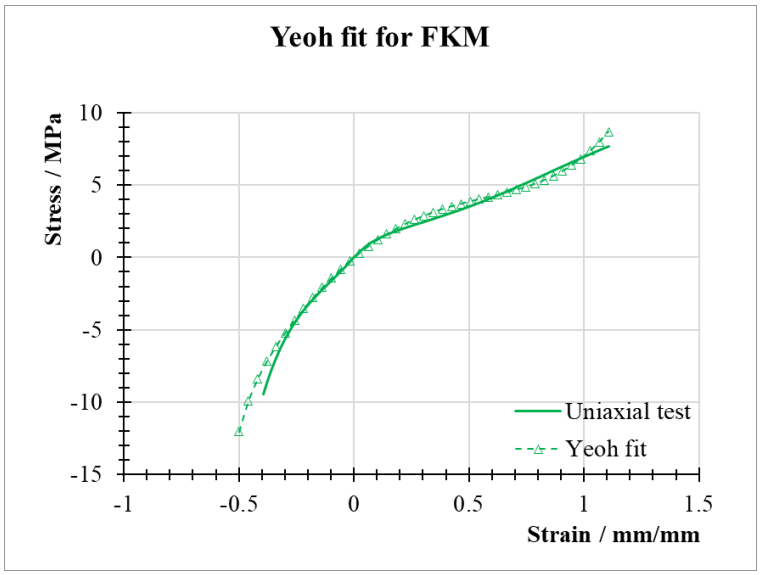

Fig. 3.3: An example the quality of the Yeoh fit is shown for an FKM 90 test at 60°C.

Table 3.2: Mechanical properties for tested elastomers at different temperatures.

	Temperature /°C	Young's Modulus /MPa	Ultimate tensile strength / MPa
HNBR 75	20	7.27	7.49
HNBR 75	60	6.66	7.05
HNBR 75	120	6.88	5.53
HNBR 90	20	16.62	18.35
HNBR 90	60	11.38	15.43
HNBR 90	120	10.40	7.76
FKM 75	20	8.97	9.36
FKM 75	60	7.34	7.11
FKM 75	120	6.51	3.22
FKM 90	20	17.52	6.53
FKM 90	60	13.40	6.91
FKM 90	120	10.87	5.02

The behaviour observed in table 3.2 is consistent with what is normally expected in elastomer mechanical behaviour. As the temperature goes up, the modulus and tensile strength for all the elastomers goes down. This effect is particularly stronger on the higher hardness elastomers, given their higher filler content. The only elastomer that actually increased in modulus with increasing temperature is HNBR 75, for the reasons previously discussed.

Ultimate tensile strength is also affected in the way that is expected. With higher temperatures, the strength decreases. One very noticeable pattern is how FKMs are considerably weaker than their HNBR counterparts. With lower strength comes the possibility of more cracks/failures under high pressure levels, this will become more apparent in chapter 5, where tests results are examined.

The Yeoh coefficient that are derived for all four rubber materials at each of the three temperatures are compiled into Table 3.3.

Table 3.3: Rubbers used for friction experiments and their Yeoh coefficients for all testing temperatures.

Rubber	Temp /°C	Coefficients /MPa	R^2
HNBR 75	20	C_{10} = 1.26, C_{20} = -3.35x10^{-2}, C_{30} = 1.47x10^{-3}	0.99
HNBR 75	60	C_{10} = 1.13, C_{20} = 1.61x10^{-2}, C_{30} = 8.66x10^{-3}	0.98
HNBR 75	120	C_{10} = 1.15, C_{20} = 1.56x10^{-2}, C_{30} = 8.72x10^{-3}	0.92
HNBR 90	20	C_{10} = 3.12, C_{20} = 0.59, C_{30} = 9. 95x10^{-2}	0.93
HNBR 90	60	C_{10} = 2.81, C_{20} = -0.81, C_{30} = 1.02	0.94
HNBR 90	120	C_{10} = 2.11, C_{20} = 1.025, C_{30} = 0.26	0.98
FKM 75	20	C_{10} = 1.02, C_{20} = -0.07, C_{30} = 0.004	0.97
FKM 75	60	C_{10} = 1.26, C_{20} = -0.06, C_{30} = 0.05	0.99
FKM 75	120	C_{10} = 1.19, C_{20} = -0.16, C_{30} = 0.10	0.99
FKM 90	20	C_{10} = 2.44, C_{20} = -0.159, C_{30} = 0.05	0.95
FKM 90	60	C_{10} = 2.19, C_{20} = -0.42, C_{30} = 0.12	0.99
FKM 90	120	C_{10} = 2.08, C_{20} = -0.66, C_{30} = 0.35	0.99

3.2 Dynamic Mechanical Properties

To characterise the dynamic mechanical behaviour of the seal materials, a Q800 DMA machine from TA Instruments was used. Using a tension method with a 10x2x2mm sample with 0.1% deformation amplitude a frequency sweep of the properties was undertaken over a range of different isothermal steps. This generated the data that is shown in Fig. 3.4 for HNBR 75 to be generated. Because of the COVID-19 pandemic limiting access to the testing equipment in the material characterisation laboratory, the rest of the samples were not tested in time for the delivery of the project. Only HNBR 75 are presented and tested in the frictional theory models that require dynamic mechanical analysis. Starting at the lower temperatures, the storage modulus E' and the loss modulus E'' reach their maximum values on the -40°C and -30°C isothermal curves during testing. If these tests were conducted at even lower temperatures (further away from rubbery region) the magnitude

of the moduli could be even higher. Because of equipment limitations on nitrogen feed, low temperature testing was done as close to the suspected glass transition as possible. The tan δ curve clearly has a maximum in the -40°C curve. Since tan δ can be define as the ratio of energy losses to energy storage during deformation, we can say that during glass transition viscous losses from the elastomer are maximised, so the ratio of storage and loss modulus is at its peak.

The physics behind dynamical mechanical testing revolve around one thing: as the deformation frequency is increased, the deformation and reptation of the chains that occurs during deformation, happens in a smaller time window. In a smaller time window, chain reputation and bond stretching does not occur so easily, so the stress response from the elastomer will be much stiffer than it would under normal conditions. This is equivalent to reducing the temperature still further and so the left-hand side of this curve is effectively below the glass transition temperature. It is possible to use these types of measurements to characterise the temperature and viscoelastic behaviour of all four compounds and can also be used to determine T_g, which was also later confirmed using Differential Scanning Calorimetry (DSC).

As is discussed in Chapter 2, the dependence of the viscoelastic behaviour on frequency can be correlated to the dependence of frictional behaviour on the sliding velocity. The way to move from one measurement to the other is determined by the frequency of the deformation. This frequency is dependent on the surface roughness and the wave amplitude λ. Using a Williams Landel Ferry (WLF) transformation allows the measured data to be shifted to a single reference temperature. This type of mastercurve can be used to examine different friction models. These models typically incorporate terms that control how the viscoelastic properties will vary at different temperatures.

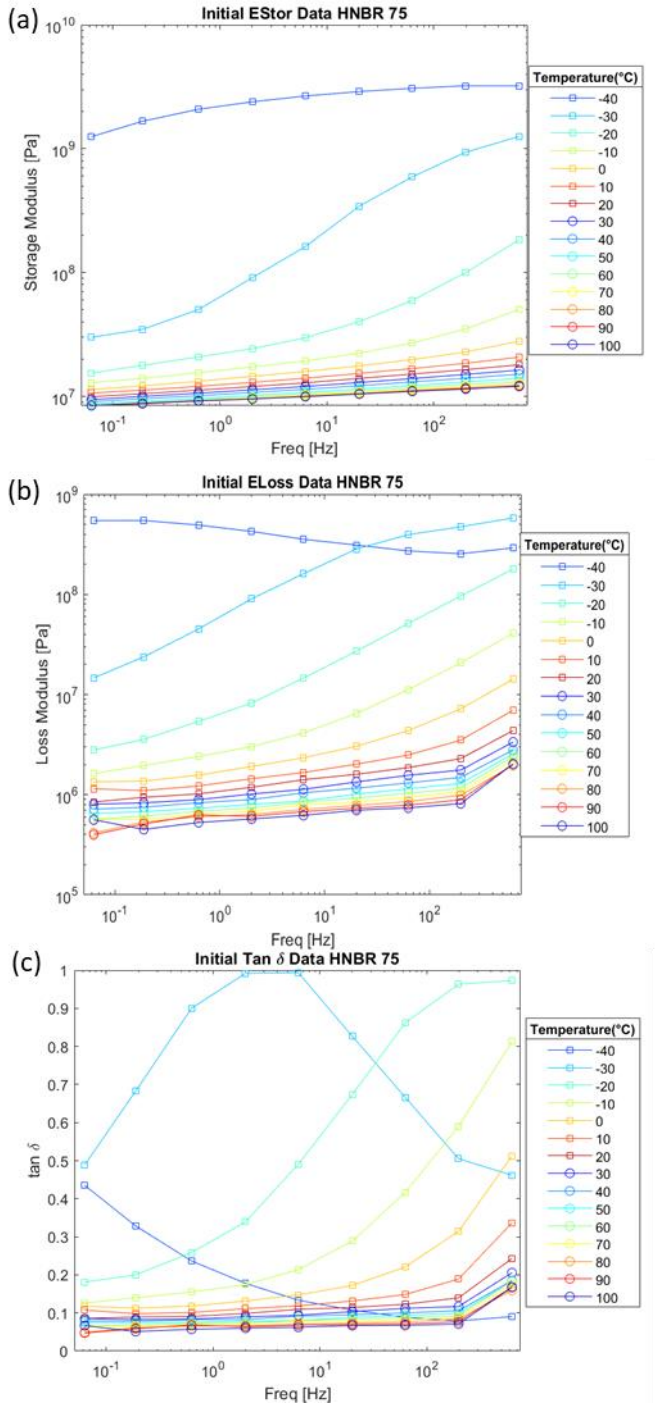

Fig. 3.4: DMA results for HNBR 75. Tension method with 0.1% amplitude of deformation. Unshifted outputs for (a)Storage modulus, (b) Loss modulus, (c) tan delta.

When we observe the resulting mastercurve from the WLF transformation of the HNBR 75 DMA data (figure 3.5) we can see the clear shift between glassy behaviour and rubbery behaviour. If 20°C is taken as the reference temperature, the transition window can be observed between 10^3 to 10^9 Hz. Approaching the curve from the low frequency range, the storage modulus only varies within the 10^2 MPa range, after reaching the transition range it increases all the way to 10^4 which is within the glassy region. Tan δ shows the same story, the peak of the tan δ is between the same frequency range (10^3 to 10^9), this transition region is where most of the viscous losses would occur when under strain.

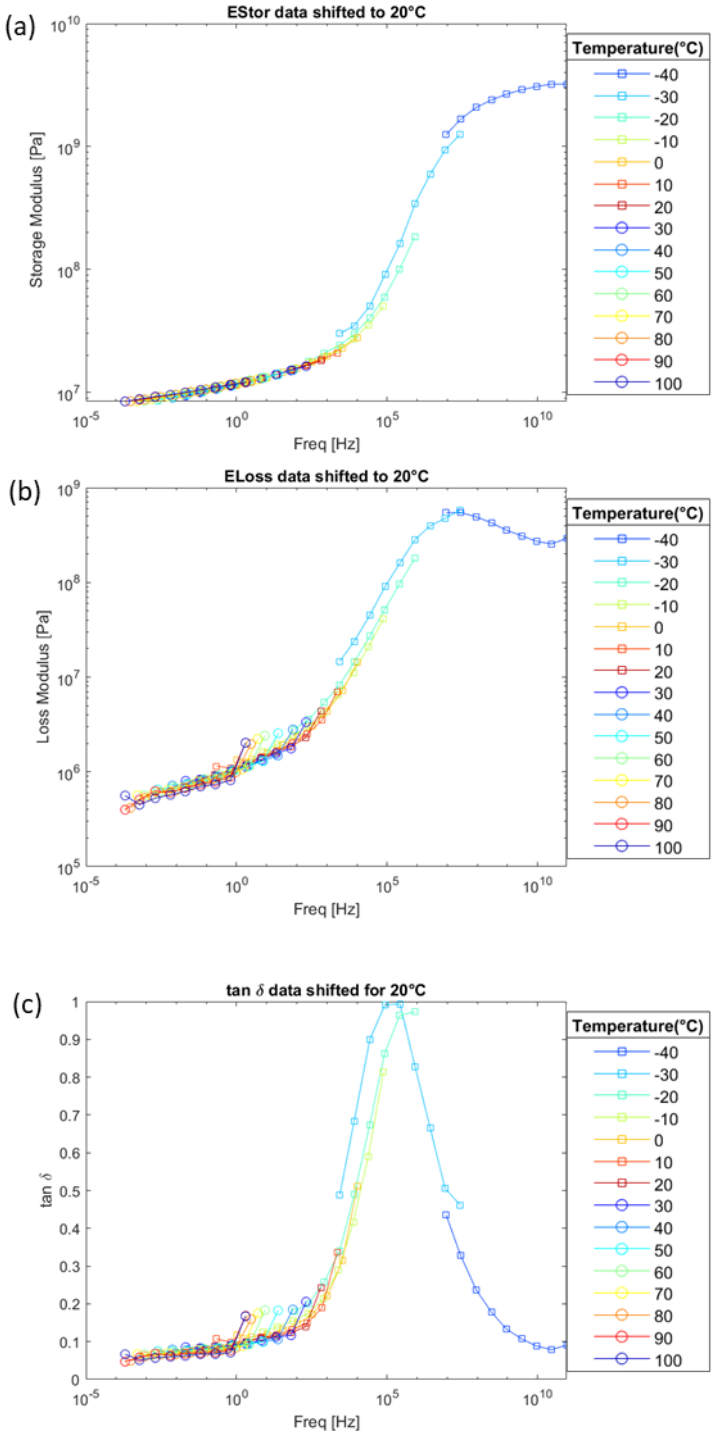

Fig. 3.5: Example of the DMA data shifted using a WLF transformation on the measured data for HNBR 75. Outputs for (a)Storage modulus, (b) Loss modulus, (c) tan delta. Reference temperature: 20°C.

3.3 Chemical and Thermal Properties

Calorimetry was done using a DSC25 from TA Instruments. HNBR samples are taken down to -80°C and increased up to 20°C at a heating rate of 1°C/min. FKM samples were brought down to -40°C and then increased to 20°C at the rate of 1°C/min. Both samples were done at atmospheric pressure. Each sample was done three times and the average result was used. The glass transition temperature was determined using a mid-point

approach on the changing slope. The T_g for the HNBR rubbers was identified as -35°C, and for FKM it was -19°C. Results are shown in figures 3.6 and 3.7. Heating process is marked as a red line in both figures, cooling is marked with a blue line.

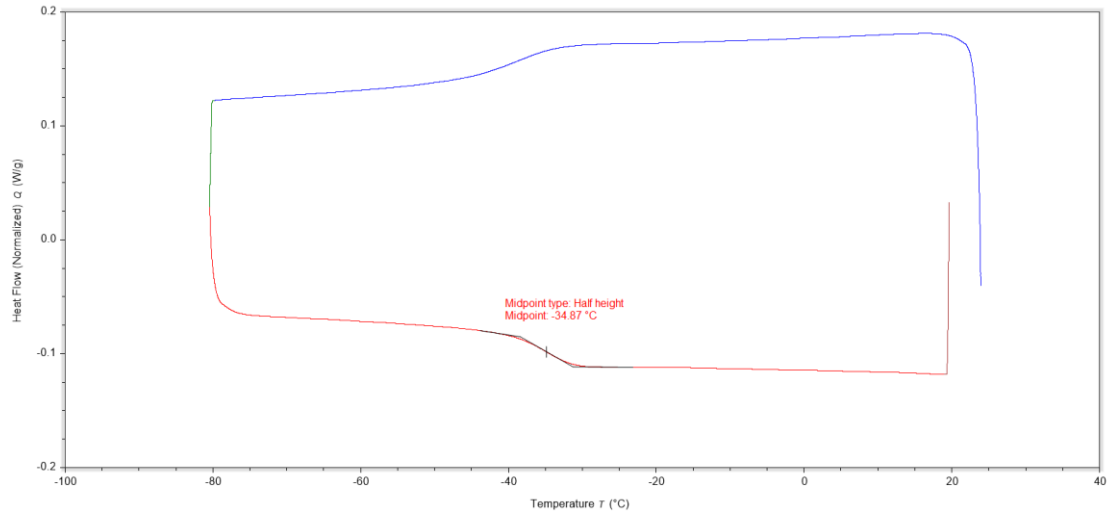

Figure 3.6: DSC scanning of HNBR, using midpoint analysis the T_g was marked as -35°C

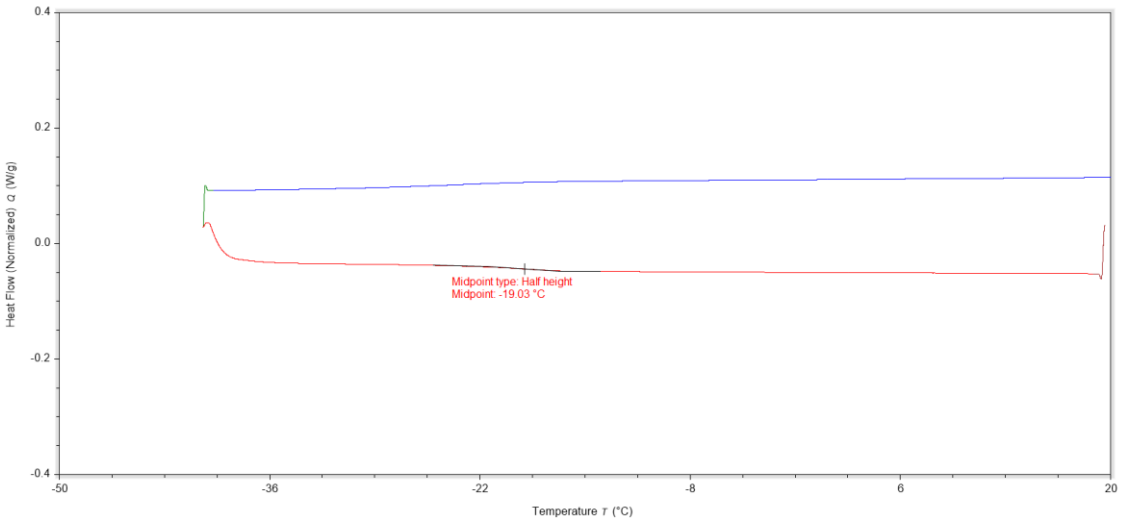

Figure 3.7: DSC scanning of FKM, using midpoint analysis the T_g was marked as -19°C

Thermogravimetric analysis (TGA) was done on all rubbers to determine their filler type and content using a TGA 5500 by TA® Instruments. Procedure was taken from ASTM D6370. Unfortunately, due to equipment failure, temperatures higher than 550 were not reached, so a switch to air environment was not possible. The analysis simply consists of the amount of polymer and volatiles compared to the amount of filler and ash.

Figures 3.8 and 3.9 show testing results for HNBR and FKM, respectively. For the HNBR, we can observe that the polymer decomposition temperature is much higher for the 90 hardness one. This indicates a difference in polymer grade for the compound, the lower percentage content of polymer and volatiles indicate that the filler content is higher. In combination with different polymer grade, this is what makes it higher hardness than the HNBR 75.

The FKMs have the same decomposition temperature. But the higher hardness and higher filler content amount relation remains the same as the HNBR. FKM also shows higher temperature of decomposition, this is one of the main reasons fluoroelastomers are used in industry, in addition to their chemical resistance. Even with the lower mechanical strength (as evidenced in section 3.1), FKMs are very useful as sealants for high temperature applications.

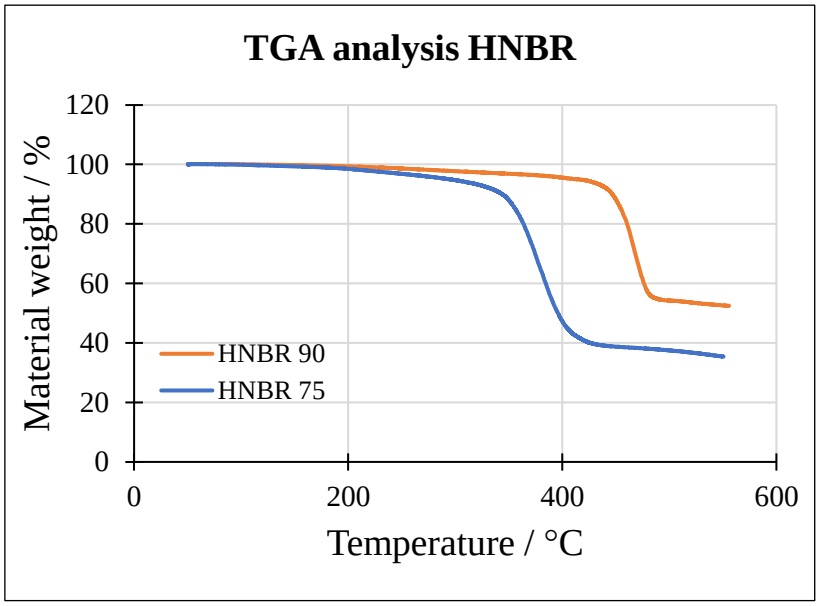

Figure 3.8: TGA analysis for HNBR compounds. Equipment limitations did not allow for full range of testing in air environment.

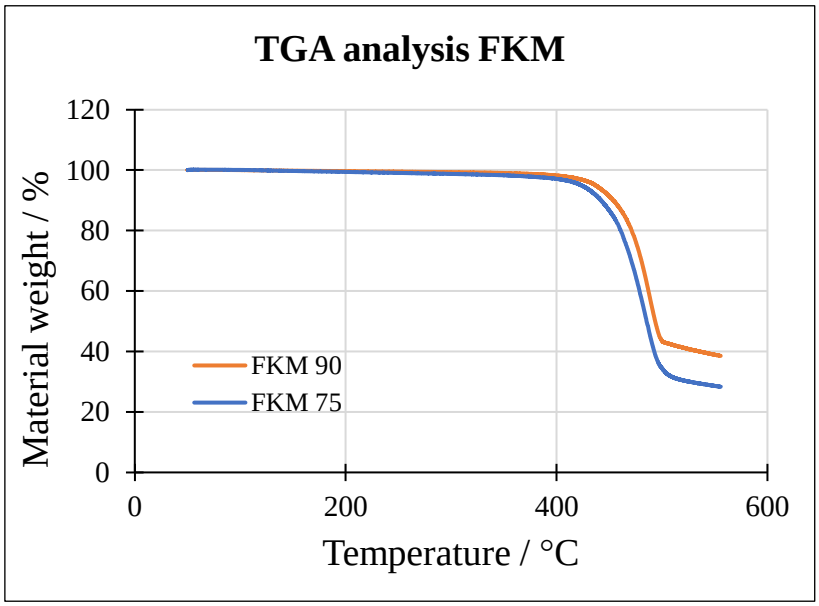

Figure 3.9: TGA analysis for FKM compounds. Equipment limitations did not allow for full range of testing in air environment.

3.4 Profilometry

Profilometry of the surface characteristics was done using a Mitutoyo SJ-400 profilometer. A stylus was drawn across the steel sliding surface against which the rubber friction was measured. The resolution of the Mitutoyo profilometer is 0.000125 μm. This system measured a 1-Dimensional profile of the height of asperities against the length of the surface. The new experimental rig was designed to be used with two different surfaces, called “Piston A” and “Piston B”. Both pistons were designed to be engaged with the seals fully submerged in a silicone oil bath. The pressurised fluid to be used in the tests was a Silicone Oil supplied by Sigma Aldrich, with a viscosity of 100 mPa.s at 20°C.

Both pistons have a polished steel surface, with slightly different finishes. One was specified with a 0.40 μm surface finish whilst the other was specified with a 0.80 μm surface finish. When defining the surface finish on the machining specifications in the industry, the value most commonly referred to is Ra. In this case the Ra value is equivalent to the height of the average peak from the mean line of the surface.

This data was analysed using the procedure described in Chapter 2 to derive both the power spectrum density (PSD) and height difference correlation (HDC) analysis of these surfaces.

Figure 3.10 shows the PSD analysis for both pistons. Examining the actual PSD values, highlights that both surfaces are very similar, even the cut-off length q_1 is almost identical. This cut-off length is a lot smaller than that typically used in tyre friction experiments, where the wavelength size is much larger[41]. For polished steels, the 20-micron value that this wavelength value represents matches the roughness that was initially indicated to the manufacturer. The cut-off wavenumbers for piston A were: $\log(q_0) = 4.51, \log(q_1) = 5.89, \log(q_2) = 6.43$ and for piston B: $\log(q_0) = 4.56, \log(q_1) = 5.99, \log(q_2) = 6.28$. Figure 3.10 also shows how these sections of the surface roughness are fitted. For PSD fits, there is typically good correlation between the linear fit and the curve. In this case, given the scale of the micro-roughness of the surface is very small (polished surface) the correlation is not as good. For this linear fit, only the slope matters, the independent term is of no physical importance for friction measurements, even the H parameter is irrelevant if the wavenumbers are reasonably selected. This small-scale roughness is the same that is measured through the HDC method.

It is worth noting, that at the very end of the PSD analysis, the values reach an almost flat slope, this means that even with the larger wavelengths, an actual change in the power spectrum is not seen. This is likely due to the stylus not having a small enough resolution to pick up the changes in micro-roughness at the lowest scale for carefully machined steel surfaces. Since both pistons are made of stainless steel with a similar surface finish, this was anticipated.

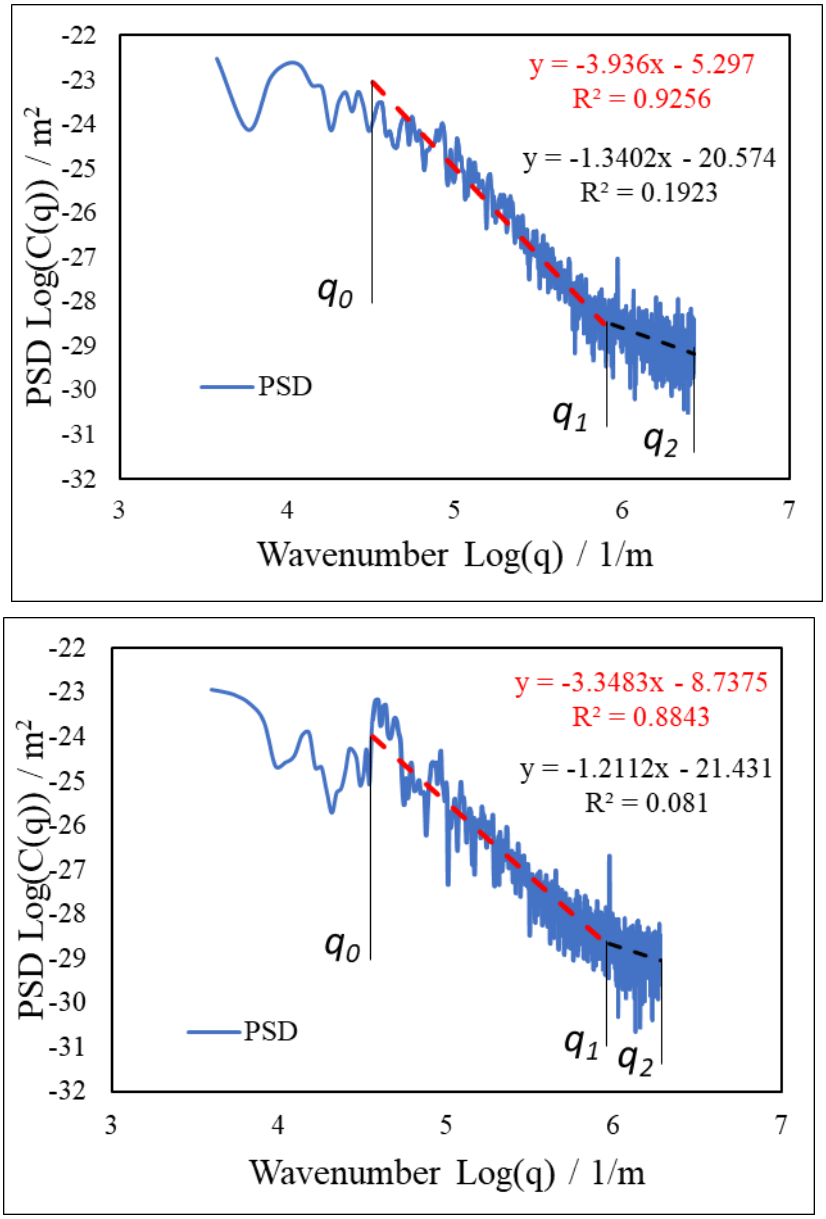

Fig. 3.10: Power spectrum density for piston A (top). Power spectrum density for piston B (bottom). We can see the wavenumbers used for the determination of the horizontal cut-off length.

HDC analysis is presented in figure 3.11 using the same stylus data. Both methods are a statistical analysis of the surface roughness. They both observe where most of the surface roughness profile lies, so it is expected that their results are not identical, but that they are similar. The similarities of both surfaces are also observed in the HDC results.

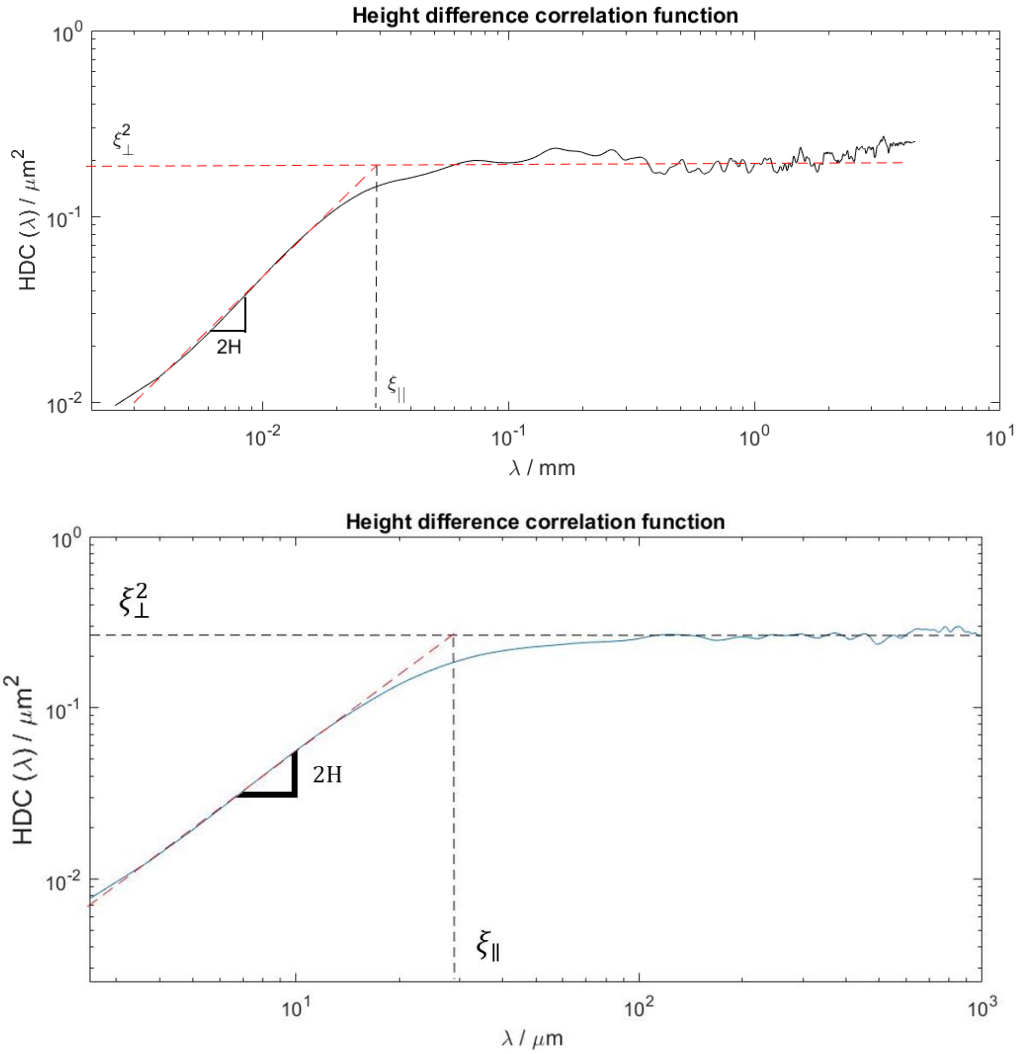

Fig. 3.11: HDC analysis for piston A (top). HDC analysis for piston B (bottom). We can observe the vertical and the horizontal cut-off length in both calculations.

Surface roughness characteristic features are shown in table 3.4. All features were separated by analysis method. All results are very close to each other, having hardly any difference between the analysis methods.

Table 3.4: Surface descriptors for both PSD and HDC analysis on pistons A & B.

	PSD		HDC	
Piston	A	B	A	B
Vertical dimension /μm	0.38	0.77	0.29	0.52
Horizontal dimension /μm	19	25	27.5	32.5
Hurst exponent	0.67	0.61	0.68	0.61

Once the characterisation of both, material and substrate are done, the frictional behaviour can be modelled and observed. Since the piston wavelength values have been selected, the local frequency of deformation for rubber materials can be marked. This, along with the frequency dependant mechanical behaviour and the WLF superposition explained in chapter 2, is enough to fit the Persson friction models and compare them to test results.

Since there is also clarity of the mechanical response the rubber will provide when compressed radially at different temperatures, the FEA models for radial compression of seals are good enough to provide the normal forces that is obtained from seals.

These three things: material model, surface characterisation and variable selection are enough to perform a full study of rubber friction with the newly created rig. Even though the functioning is straightforward (simple vertical motion), compliance with pressure and temperature requirements give the rig some complexity.

Rig design and operation are described in chapter four. Although there is no direct visualisation of the seals engaging with the piston, and the leakage is only observable through pump rate, understanding all stages of the test is not a difficult task. Explanation of these stages and how to obtain accurate data from them will be explained. This explanation along with the material characterisation data are described in chapter five. A full recreation of friction models and description of frictional behaviour of rubber under high temperature and high-pressure conditions.

4. High Pressure Dynamic Friction Test Rig Design

It is apparent from the review of the previous scientific literature in chapter 2 that the friction behaviour of rubber has a significant dependence on a range of other factors. Normal forces can change the contact area and thus the adhesional component. Velocity influences the rate of deformation of the rubber, changing the strain response, as it is described in dynamical mechanical rate results in chapter 3.Test temperature will affect not only the mechanical response of the elastomer, but also the viscosity of the elastomer. Establishing the dependence of the friction on various parameters was the most important feature of this work, and in particular to verify this for the typical elastomers materials commonly encountered in the oil and gas industry.

4.1 First Friction Experimentation Results

Initial attempts to test the frictional behaviour in rubber were done using a pulley type of test system described in section 2.9. This test required that a block of rubber was glued to a metal plate and dragged over a prepared surface such as a machined aluminium block using an inextensible string. The string is connected to a tensile testing machine whose load cell was used to measure the sliding friction forces with the normal pressure force being determined simply from the weight of the rubber block and plate, with additional bronze weights included on top of it. This initial test was adopted as it has been used extensively in the past by other researchers at QMUL and it was hoped it would allow difficulties associated with rubber friction testing to be identified. After preliminary results and testing method limitations are observed the testing procedures will then be changed to accommodate the higher normal pressures and elevated test temperatures as they are expected in the oilfield applications in discussion with the research sponsors. The approximate size of the blocks was 20 x 20 x 2 mm, which produced a resulting nominal contact area of approximately 400mm^2.

Whilst carrying out these tests, a high-speed camera was placed alongside the rubber pointing in a perpendicular direction to the sliding trajectory. Figure 4.1 shows the behaviour of the rubber block whilst sliding against a smooth aluminium plate. In the initial state, shown as Image A, the block it is completely in contact with the metallic surface (at least on the apparent or nominal macroscale resolution). After overcoming adhesion forces, the block lifts (as seen in image B and C of figure 4.1) significantly reducing the nominal contact area present during the sliding motion, it finally lands on the surface and returns in a complete contact as shown in Image D. This jumping motion is known as stick-slip behaviour. Stick-slip can be resumed into three phases: the body is in contact with the surface, where adhesional friction is maximised and there is no movement despite tangential forces acting. Secondly, the tangential forces overcome the adhesional elements and the body moves rapidly in the direction of the tangential force, this jump is the “slip”

part of the movement. Lastly, once the body lands against the surface, the adhesion takes over and the cycle begins again. This behaviour makes it very difficult to corroborate the instantaneous real or nominal contact area during frictional sliding. Using the pulley system method proved to be very difficult to obtain an accurate measurement of the contact pressure.

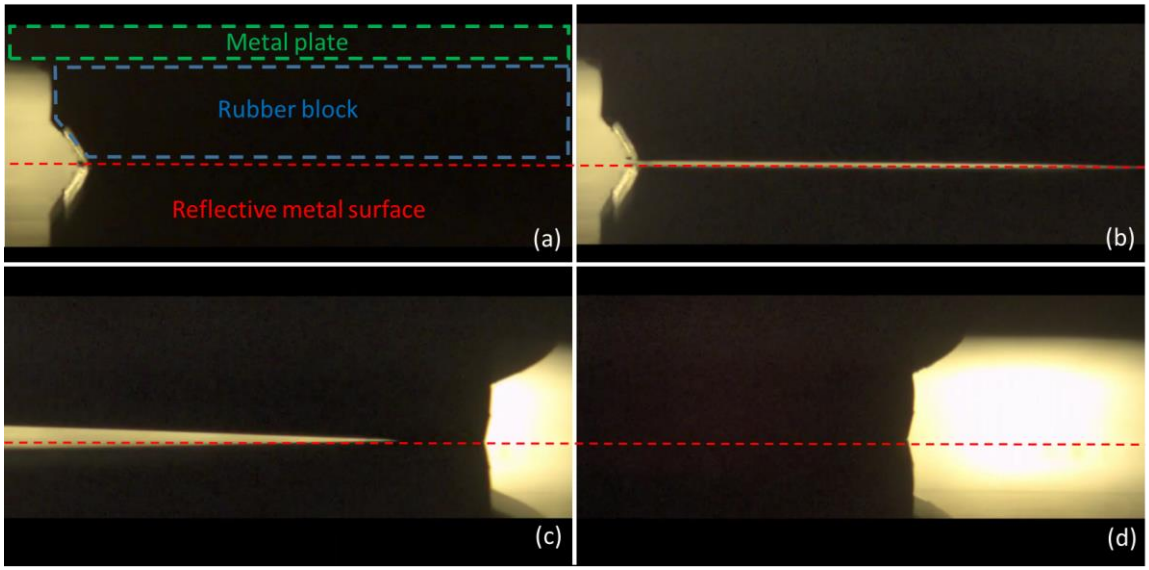

Figure 4.1: Pulley tests high-speed camera. Image (a) shows the initial configuration when the rubber block is in initial contact with the aluminium surface, Image (b) shows the moment when the rubber block jumps out of contact from the substrate, Image (c) shows the block landing back in contact and Image (d) shows the moment when the block is returned into contact over the entire surface.

Examining the measured outputs for these types of pulley experiments highlights that this stick slip behaviour is apparent. Figure 4.2 shows the frictional force against displacement at two different sliding speeds for an ethylene propylene diene monomer rubber (EPDM) elastomer sliding against an aluminium block, measured at five different normal forces. The selection of EPDM is not because the material is of particular interest for the research, it is simply the material that was available in the form of test sheets (already cured) to test the pulley system and observe whatever limitations it might have. At higher normal forces, as the real contact area is increased, the observed stick-slip effect becomes increasingly obvious. Higher normal loads output peaks of forces before a sudden drop happens, as the jump section mentioned previously. The sliding velocity also has a large effect on the introduction of the stick-slip motion, making these types of measurement especially difficult. To test the frictional sliding behaviour at these higher normal loads, required a restriction of this stick slip motion to be introduced to allow a more meaningful examination of the real in-service friction behaviour encountered in dynamic seals at a high pressure. Much heavier loads might produce this, but in practice this approach was not thought practical in these pulley types of experiment.

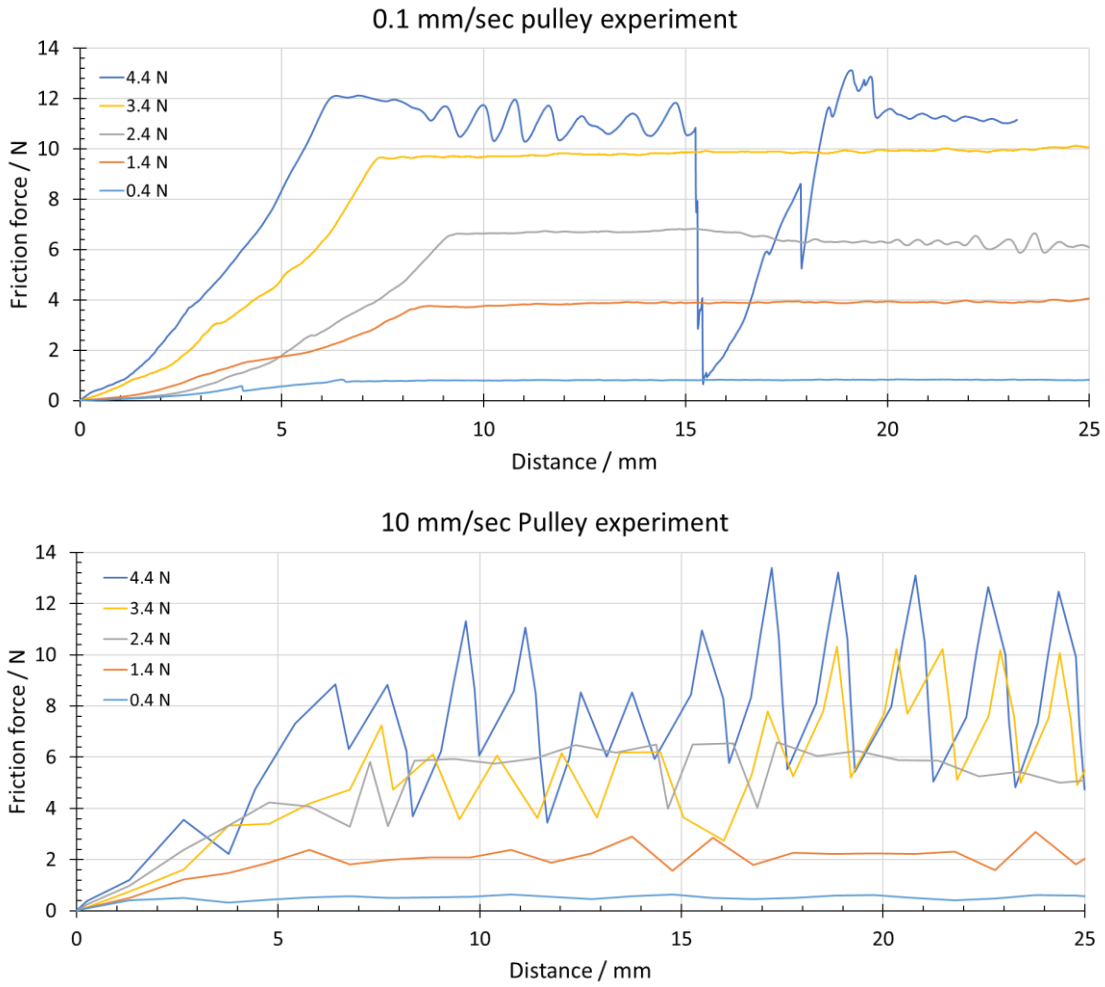

Figure 4.2: The measured friction force produced by sliding a block of 20x20x2 mm rubber against a block of machined aluminium. Both tests were done using the same rubber material against the same surface. The 0.1mm.s^{-1} velocity (top) shows much more stability and less stick-slip behaviour than the 10mm.s^{-1} one (bottom).

After looking at the viability of restricted movement tests, a rotational experiment with compression forces was chosen next. An Instron ElectroPuls dual axis test machine (E10000) was used as it can simultaneously apply and measure a vertical compression force in combination with a finite torque applied during a rotation. Adopting a simple flat-ended short rubber cylinder (known in the industry as a rubber button) which was located in the centre between two compression plates allowed the friction to be tested for a wide range of different levels of pre-strain (or required pressure) by the subsequent rotation of the plate. The resulting torque was assumed to represent the frictional sliding shear forces during the slip phase. With the torque up to the point of sliding simply producing an initial shear deformation in the button.

Figure 4.3 is a bottom-view schematic of this experiment. The button was compressed by lowering the top plate until either the desired strain or pressure level was reached. Next the top face was rotated through 180° and then returned to the initial position. The white mark on the button was used to identify which interface was slipping during the experiment.

When calculating the friction force, it was assumed that all the torque measured by the plate were generated as a shear in the button. Initially, initial shear deformation occurred in the button, but this reached a maximum when the button started to slide against one of the sliding interfaces. During this sliding phase, the measured torque can be related (shown in figure 4.4) using simple statics to the shear force, which is at a maximum at the outer edge of the button.

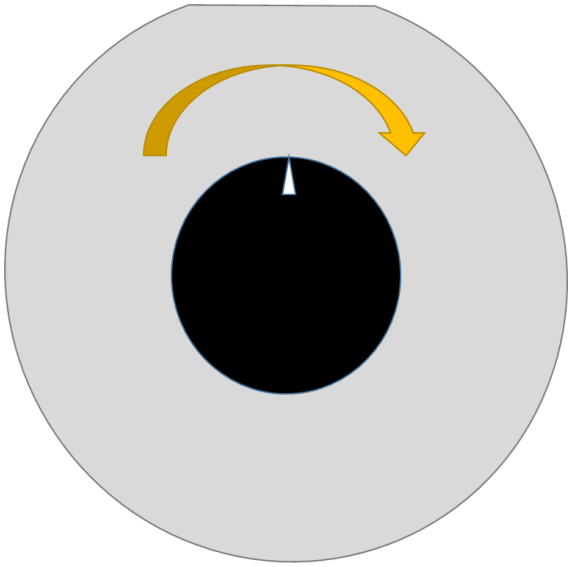

Figure 4.3: Schematic of button experiment. The black rubber button sits at the centre of a compression plate. The white triangle is a mark for the researcher to observe that it is the compression plate, and not the button rotating during the experiment. The plate rotates in the direction of the arrow.

For these experiments, the E10000 can measure the shear stress during rotational forces as well as normal loads on its dynamic load cell. A simple analysis of the shear stresses indicates that the torque increases linearly with radius until the edge of the button is reached. With the shear stress at the centre of the button being zero. There are two approximations that have been made when making this assumption. The first is that the contact area does not change, which is for a real surface not true as the pressure increases then the true contact area will also increase and then adhesional contribution to the friction will increase significantly with the real area of contact. The second problem is the assumption of an equivalent energy dissipation mechanism across the entire surface. This is clearly not the case as the hysteresis contribution will be much higher at the edge of the cylinder (where the sliding velocity is much higher) than towards the centre.

Since rubber can be assumed incompressible at this strain level (under 30%), the volume of the entire button remains the same, the button is expanded radially to compensate for the compressive strain.

To calculate the force from the torque output, a characteristic average value for the radius was required. The calculation was done using the previous assumption that the torque increases linearly with radius. Given that area increases in quadratic form in a circle,

there is a wrong assumption about the adhesional contribution. The compromise of middle linear area was used to simplify the calculation. Since there is no intent in breaking apart the contribution of friction, but just observing how friction changes with speed and pressure, this error does not carry over into further testing. Further research will do well to create two different calculations: one where the adhesional contribution is done using the integration of linear area; and a second one with the hysteresis contribution depending on the angular speed as it increases with increasing radius.

Conceptually, this is correct in a beam type model. With longer leverage distance, the torque increases. In this case, the assumption is that not only distance matters, but also area. This is the concept that comes from rubber dry friction theory presented in section 2.9.2. The line was the length at which the triangle of torque was split into two equal areas. Figure 4.4 shows a schematic of this problem, whilst equations 4.1 to 4.4 show the method to obtain the characteristic length h that would be used for the calculations. h represents the single value of distance that will be used for the calculation of torque forces on the button from adhesional friction. There is no particular property or characteristic tied to this value.

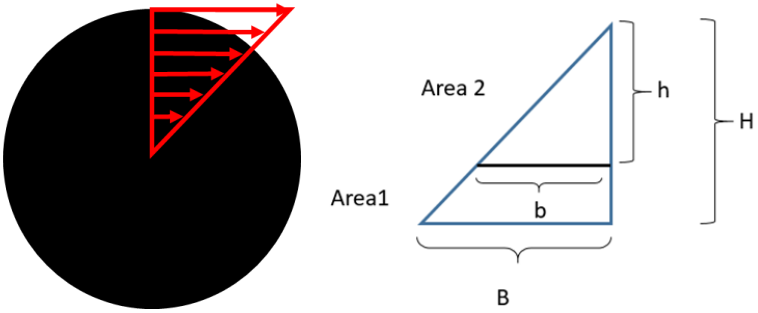

Figure 4.4: Schematic of the torque distribution from the button's centre (left). Equal triangle sketch showing the characteristic length h. Assuming a linear increase of torque, h is the point that we use to measure velocity and torque.

$$\frac{1}{2}bh = \frac{1}{2}\left(\frac{1}{2}BH\right) \rightarrow bh = \frac{1}{2}BH \tag{47}$$

$$\frac{b}{h} = \frac{B}{H} \rightarrow b = \frac{B}{H}h \tag{48}$$

$$\left(\frac{B}{H}h\right)h = \frac{1}{2}BH \rightarrow h^2 = \frac{1}{2}H^2 \rightarrow h = \frac{H}{\sqrt{2}} \tag{49}$$

$$\tau = h \times F_f \tag{50}$$

Once the average (or representative) value of h was obtained, the raw values of torque could be translated into frictional force. When divided by the vertical load that was simultaneously measured on the compression plates throughout the experiment as well, coefficient of friction was determined for different precompression levels and linear velocities (were translated from angular velocities).

Precompression levels were 10, 20 and 30%. In field operations, seals have a compression range of 10-15% for dynamic applications and 20-30% for static applications.

CoF will be affected by the normal contact pressure, but the contact pressure levels came from the selection of strains. A linear growth of strain levels was used to give an idea of the behaviour of rubber friction response similar to those of unpressurised seals during setting phase. In terms of velocity, since literature often separates CoF vs. velocity curves in the logarithmic scale, three decades of velocities (1, 0.1 and 0.01 mm/s) were tested to observe how friction would change with significant velocity changes.

The material selected was the same EPDM used in the pulley experiments, due to the availability of it. Once experimental conditions and limitations were worked through, a full experimental analysis of the elastomer compounds was undertaken.

An example of the torque calculation from the E10000 experiments is shown on figure 4.5. The button is rotated 180° in one direction and then in the opposite direction. The initial rotation (shown in blue) and when it is rotated backwards to its original position (shown in orange) are then translated into CoF (Fig. 4.6). These two lines are then averaged and presented as a single point in figure 4.7.

Once all combinations of strains (3) and all combination of velocities (3) were tested, a CoF vs. Pressure graph, as presented in figure 4.7, highlights the pressure dependent behaviour of rubber with varying pressure. Exponential trendlines are presented to better observe the tendency of this behaviour, they are not used in any particular calculation or theory, because of this, they are not presented with the corresponding R^2.

The experimental results showed good consistency with the literature. Pressure increases consistently showed a drop in the measured CoF, higher sliding velocities had the opposite effect, increasing the CoF value. For most rubbers, a range of 1-10 mm/s is where the peak adhesional component is experienced [41]. Since there was no lubrication applied to the buttons, prior to testing, adhesional contributions to friction were maximised. Even if lubricant was indeed applied, the fact that the buttons were being compressed by flat plates, the lubricant can just be squeezed away from the interface between the rubber and the plates. The effects of barrelling of the buttons as the normal pressure is increased further above 3 MPa, plus the difficulty of completely submerging the elastomer in a lubricant (in order to simulate the behaviour of real oilfield seals) made this experimental approach less than optimal for this research project.

In order to better understand the possible friction parameters encountered in practice when testing under still higher pressures and over a wider range of temperatures an alternative approach was developed next. The proposed methodology required the development of a brand-new friction rig. The elastomer was constrained to move only in the direction of frictional sliding, thus avoiding stick-slip types of behaviour. A confined location for the rubber limited the amount of deformation that the rubber could undergo, this in turn limits the possible mechanical failures that arose as well as other effects such

as the barrelling or extreme shape change encountered in the test piece.

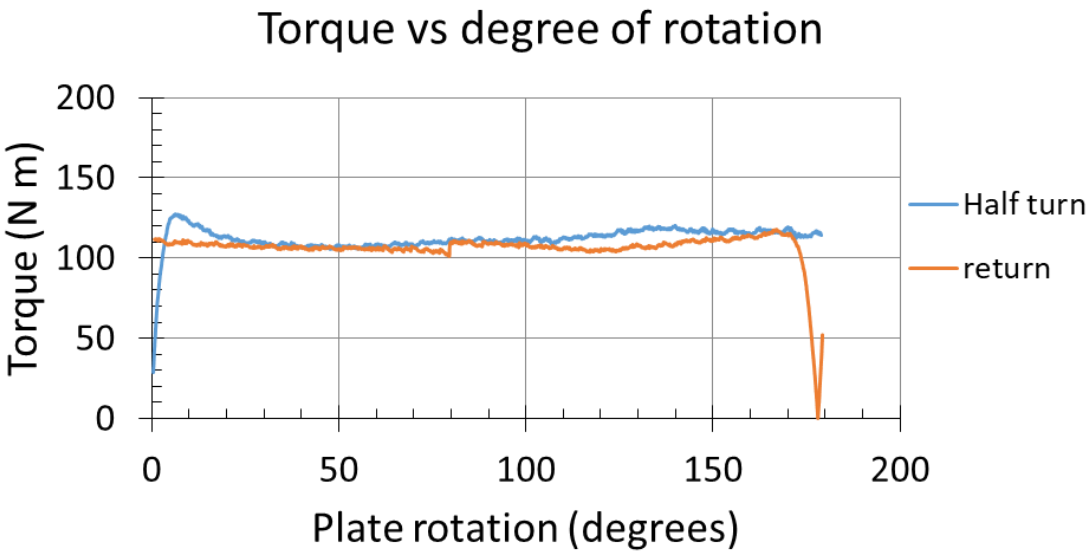

Figure 4.5: Torque values obtained using eq. 50 after plate rotation whilst compressing an EPDM rubber button at 30% strain and 0.01 mm/s rotational velocity. Data is stable, at pressure values around 1 MPa.

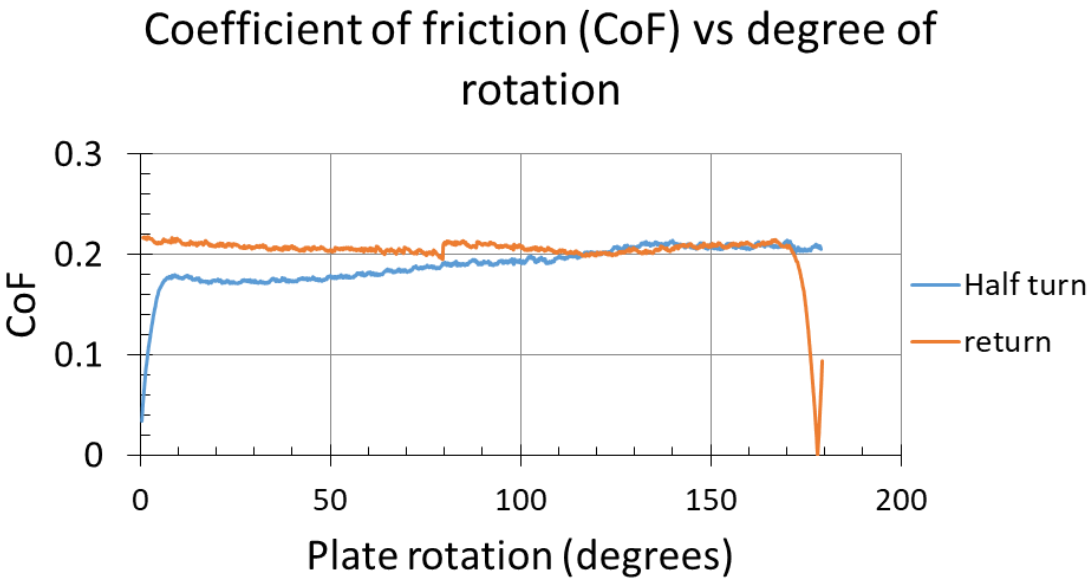

Figure 4.6: Coefficient of friction values obtained using the frictional force F_f from eq. 50. The normal force values are obtained directly through the Instron E10000. EPDM rubber 30% compression and 0.01 mm/s rotational velocity.

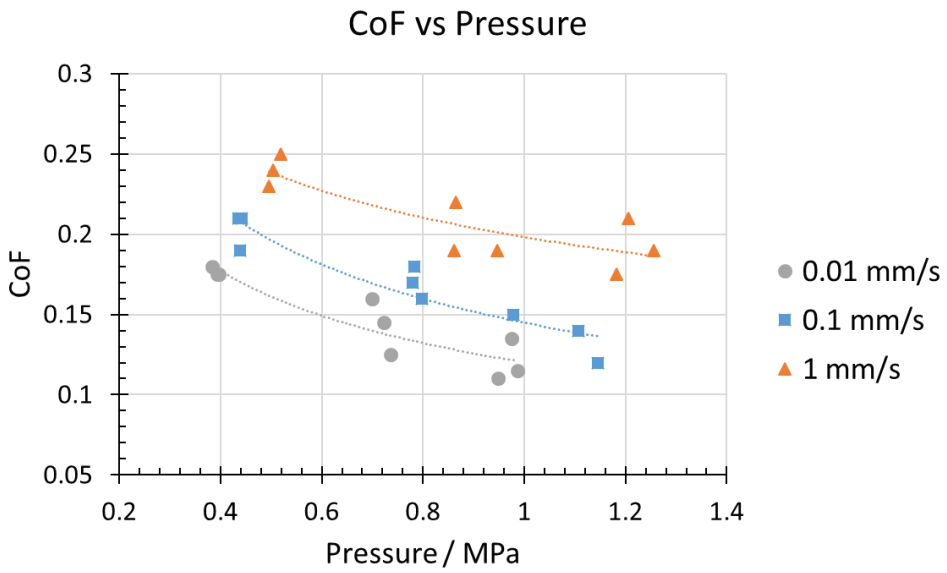

Figure 4.7: EPDM Button frictional data after arranging results by pressure and velocity. The behaviour of friction is a good replication of theoretical data. Once data is discriminated by velocity, the effect of higher frequencies of deformation is also observed.

The resulting test setup had to contain a closed system that included the lubricating liquid, but which also allowed this liquid to be pressurised. The elastomers that were tested also worked as seals to enable the generation of a significant pressure. The ideal sample would be commercially available (for ease of sample preparation) and quick to replace. The final decision was made in consultation with the project sponsor, and this was to use O-rings, since these are commercially used extensively in the oil & gas industry, they are mass produced and can be changed in the newly developed sliding test rig relatively quickly.

4.2 Novel Rig Design

No existing facility existed prior to this investigation to measure the effect of sliding velocity on the friction coefficient of elastomers used in sealing applications under specified conditions such as elevated temperatures or high pressures. Therefore, it was first necessary to build a novel test system. The essential requirements were that it could measure the friction sliding force using a calibrated loading cell for different types of rubber surfaces that were sliding against a precisely manufactured and accurately measured steel surface. This had to be maintained whilst the rubber was simultaneously subjected to large sealing pressure and was operating at carefully controlled operating temperatures. Although rubber sealing in oilfield applications can reach 140 MPa, reaching this range was an impossibility with the laboratory conditions available at the university and at the sponsor's research facility whilst keeping the dimensions of the rig that would allow commercial O-rings to be easily installed. A compromise had to be made and 35 MPa was decided to be high enough to observe the behaviour of O-ring friction under high pressure behaviour. This is equivalent to a hydrostatic column of 3 km of water. Deep-water wells frequently reach this depth at the seabed.

To achieve this a novel sleeve-piston type of test rig was designed and developed that could withstand an internal pressurisation of up to 35 MPa whilst running sliding friction tests. The target rubber geometry adopted for these tests were O-rings. The carefully design experimental setup is shown in Fig. 4.8. At the high pressures that were encountered during the experiment, neither the normal pressures nor the contact area could easily be measured directly. It was therefore necessary to model the behaviour of the rubber seals in the rig to calculate both values using an FEA modelling approach. This allowed the coefficient of friction to be calculated from the measured sliding force at each sliding velocity.

Fig. 4.8 shows the rig was based on a simple piston design, in which the outer sleeve can hold O-rings that can vary either the cross-sectional diameter or compression levels, with the level of compression being determined by the choice of the appropriately sized machined grooves into which the O-rings were inserted. Different central rods, which were hollowed out for ease of handling, were made with different surface roughness characteristics machined into them. The effect of the surface profile on rubber friction are well known from the literature [34] and so the piston was characterised using profilometry and analysed using a height difference correlation (HDC) approach. Profilometry of the surface characteristics of the piston was done using a Mitutoyo SJ-400 profilometer.

The entire experimental setup is shown in figure 4.9. The upper section (piston) was mobile and engaged through the O-ring connectors with the fixed section (sleeve). Both sections were designed to connect to an Instron ½ inch female connection type. The mobile section connected to the crosshead of the 5900R84 tension machine. This was used to control the speed of the testing (which for this work ranged from 0.1 to 10 mm/s). In series with the system was a load cell that measured the vertical forces generated by the friction once it engaged with the O-rings. The fixed section had different O-ring glands that allowed the use of two different sized O-rings with two different compression levels (13% and 24% nominal compression). The defined dimensions were adopted as a compromise between being light enough to enable ease of handling and robust enough to take the stress.

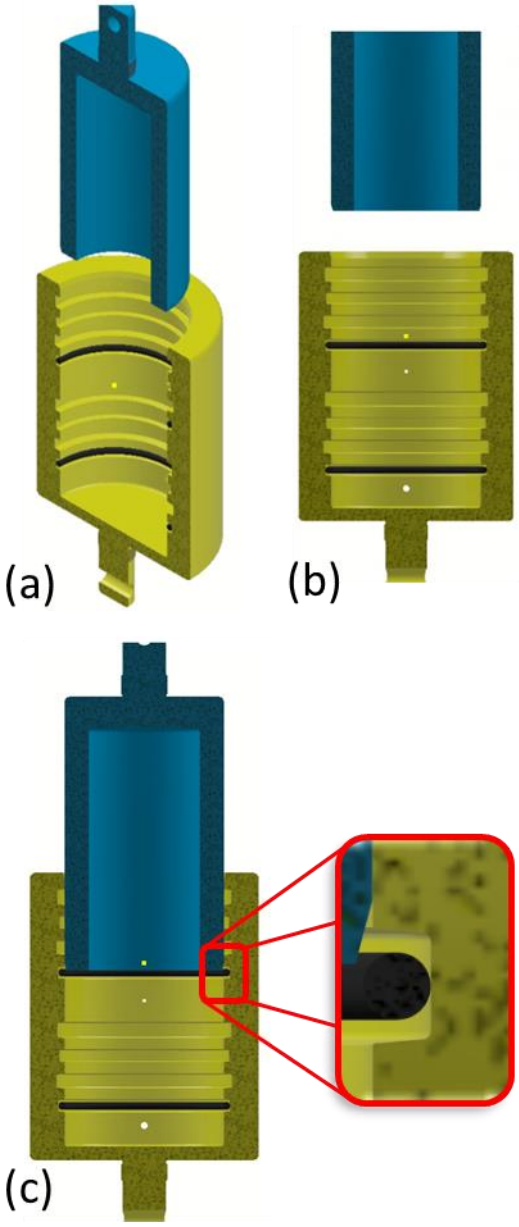

Fig 4.8: a 3D modelling of the friction rig. (a) a half cut 3D view of the piston (blue) and sleeve (yellow) with the O-rings (black) installed. (b) 2D front view before the engagement of the piston. (c) 2D front view of the piston engaging with the O-ring, zoomed in on the gland. The gland will be used for FEA to determine normal forces.

The overall weight of the rig was low enough so that there was no requirement for lifting tools to assemble the rig, whilst ensuring that the piston was able to safely withstand the large pressures and stresses encountered during testing.

The sequence of different glands was repeated to create a sealed volume between the two O-rings. Between the two rings was located a pressure injection point that allowed the pressure between the two seals to be increased during testing to a predetermined and well controlled higher level. O-ring glands were designed for O-rings of 113.67 mm inner diameter and two different cross-sections, two for 5.33 mm diameter cross-section (BS 349) and two for 6.99 mm cross-section (BS 425). With these sizes, the handling of the rig would be safer, more comfortable and efficient for the operator. With two different cross-sections,

different contact areas can be analysed whilst keeping the same strain and using the same rig. In this study, there was not enough material or time to test the second cross-section.

In order to control temperature, thermocouples were used at various points of the sleeve (centre and glands). Although there are no assigned sockets for thermocouples, these readings, along with the environmental chamber controllers and temperature measurement, temperature values were consistent across zones and measurements.

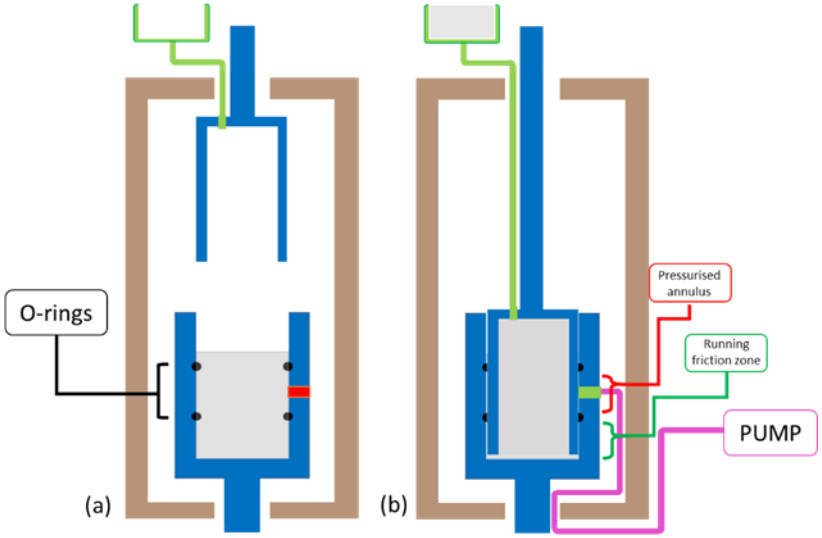

Fig. 4.9: Experimental apparatus for rubber O-ring friction under extreme pressure. (a) Cut away cross-section of the novel friction rig 3D model prior to engaging the seals. (b) After the seal has been engaged. The diagram highlights that the full working friction rig is located inside an environmental chamber to allow the operating temperature to be controlled.

The calculation of the coefficient of friction assumed that there was an equal contribution to the frictional forces from both O-rings during sliding. Even with this presumption, there was a risk of decentralisation of the piston, which could potentially damage the test fixtures or the O-rings under test and could potentially generate uneven force responses. To check the validity of this assumption, tests were run at different speeds with only one O-ring in position and compared with another set of tests that were done with both O-rings in place. Tests were also carried out without any form of lubricant in position which meant that they had no capability of having the pressure increased. Fig. 4.10 shows how the vertical force varied with the displacement during the installation phase for both systems with just one O-ring (the solid lines) and for both O-rings (the dashed lines) for three different sliding velocities. Although during setup, there is a check for concentricity of the piston, there is no calibration procedure at the beginning of the tests. The repeatability of O-ring contribution to vertical forces was the only form of quality check. Misalignment issues were a concern during the initial tests. This problem is solved during the initial setup. After any change of rig components (pistons or sleeve), the parts are connected to the tension machine, but not tightened. A “dummy” run is performed with loose connections and fresh O-rings, slowly moving along the sleeve and monitoring any spikes in vertical

forces. Only after the piston has fully entered the sleeve without any issues, are the connections tightened. If misalignment takes place, it would be observable by sudden spikes in the tension values. This sometimes occur in the event of O-ring extrusion, but it is noticeable in the output. For these occasions, the rig is depressurised, and the test is stopped.

Examination of figure 4.10 shows an initial spike in the force at about 40 mm for all the systems. That correlates with the engagement of the first O-ring and then a smooth sliding force until the next O-ring is encountered in the dashed lines which correlates with the second peak just before a 140 mm displacement is reached. Beyond this is the measured sliding friction response when both O-rings are activated. It is clear from these measurements that the simple assumption of basically equal contribution to friction by both O-rings is valid. Thus, the final frictional value of two O-rings is broadly equal to double the single O-ring value. The initial setting response is slightly lower for the second O-ring; this could be attributed to centralisation effects, with the first O-ring correcting for most of any eccentricity issues that stem from the initial misalignment of the central piston and the outer shell in the testing equipment.

Table 4.1: Repeatability tests for single and double seal runs.

Velocity / mm/s	Friction force / N		Ratio
	Single seal	Double seal	
0.1	759	1512	1.99
1	1321	2622	1.98
10	3329	6230	1.87

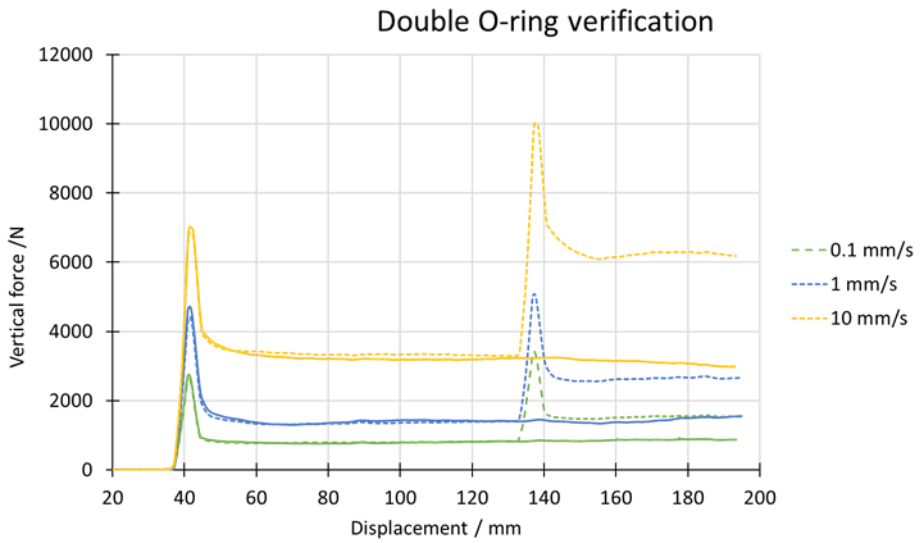

Fig. 4.10: Piston setting tests, continuous lines represent the measured insertion force when a single O-ring is fitted into the rig. Dashed lines show the measured force when both O-rings are in position. The force contribution from the second O-ring is approximately double the magnitude when a single O-ring is used.

Table 4.1 shows the values of the piston setting tests in single and double O-ring situations, to assess the validity of the assumption that two O-rings will simply output double the friction force that one O-ring causes. This assumption facilitates finite element modelling and simplifies calculations done for test results. It is observed that only at the higher speed levels, the assumption starts to deviate from the idealised conditions. This could be caused by heating or wear effects, as well as more aggressive contact of the piston edge with the seal. Measurements are taken once the O-ring has moved more than 20 mm form setting and is in a frictional force plateau.

After both O-rings were fully engaged the rig could be exposed to an internal pressurisation from the pump. This caused the upper O-ring to be pushed upwards and the lower one to be pushed downwards. As a result of this symmetry, both an upward and a downward direction of motion can be used to study the frictional response since in both cases all the effects such as the extrusion or shear forces on the O-rings will cancel each other out. For example, the lower O-ring is sheared downwards by the pressurised fluid, which might result in a negative contribution to the piston's upwards movement; this is countered by the upper O-ring creating an identical but opposite shear. The gland design and interference fit were designed to ensure that specified nominal (or average bulk) compression levels were obtained for each O-ring. When no pressurisation fluid was used in the test, the difference in compression levels was large enough that two distinctly different contact pressures could be studied. The Parker Handbook for O-rings [48] was used to design the rig geometry and to help specify the detailed dimensions for the O-ring glands and their machined surface characteristics, such as surface roughness and tapering dimensions.

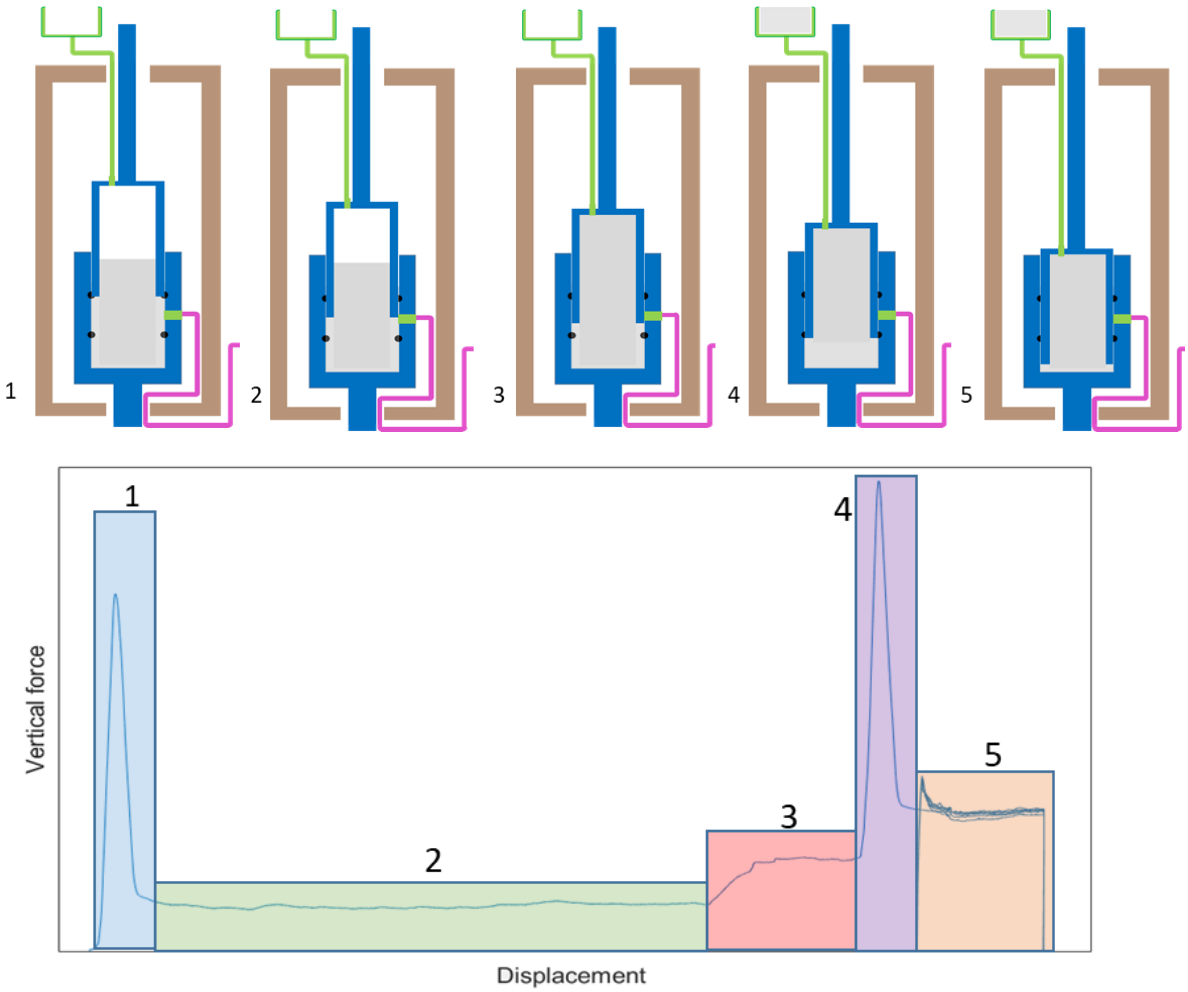

Fig. 4.11: The typical force output from the friction rig can be represented in 5 distinct sections. 1: piston engagement of the first O-ring. 2: running friction forces whilst the piston travels down the sleeve. 3: Upward forces generated by the fluid entering the pipes that lead to the overhead tank (silicone oil for this case). 4: piston engagement with the second O-ring, the annular seal is created. 5: running friction tests that can be pressurised (this is the standard data collection region).

Fig. 4.11 shows a how the force varies with displacement in a typical experiment as the cylinder is assembled. This graph is divided into distinct 5 regions. As the piston goes down into the sleeve, it initially has no resistance. Once the piston reaches the O-ring, it compresses it to fill the gland and a large spike in the force is observed (Region 1). After setting, the vertical force arises only from the sliding friction of the O-ring sliding against the rod (Region 2). Region 3 is where fluid flowing to the overhead tank generates an additional upward force that must be accounted for when analysing the running friction forces. Region 4 is the engagement of the second O-ring, at this point the annular sealed region between the two O-rings is created. Region 5 results are the ones taken for the running friction forces as the piston is cycled up and down.

To avoid any form of trapped gas between the sealing components, the sleeve was first filled with the testing fluid up to the position of the top seal and the elastomer O-rings were placed in their desired positions. When the piston was lowered, the air and excess fluid escaped through two 8mm holes drilled on the top part of the piston, which then flowed into an overhead tank held at atmospheric pressure. The tank holds the fluid while the piston is moving in the downwards direction and then returns the fluid back into the system when the piston ascends. The holes were made as large as possible whist maintaining the strength of the piston and whilst also trying to minimise any potential pressure drop when using high viscosity fluids. Although this event is less than ideal, the number of connections to the overhead tank that would have to be done in order to drop the pressure build up to a minimum would compromise the stability of the connection. A way to get around this, was to have a thicker section on the top of the pistons, allowing for more pathways for the fluid. The additional forces that would be generated as a consequence of any upwards fluid flow could be accounted for using the Hagen-Poiseuille equation:

$$\Delta P = \frac{Q8L\eta}{\pi R^4} \tag{51}$$

where ΔP is the pressure differential, Q is the flowrate in the pipe, L is the length of the pipe, η is fluid viscosity, and R is the pipe radius. Clearly, increasing the radius produced the most significant way to decrease the pressure drop. As this is a quartic relationship it is obvious that a doubling of the radius would reduce the pressure build-up by a factor of 16. The piston was fitted with two pipes of 1.8 mm inner radius connecting to an overhead tank into which the fluid was displaced during sliding. For silicone oil testing at 20°C, 6 mm/s vertical velocity, with a pipe length of roughly 1 metre, the additional force increase is calculated as 751 N. Fig. 4.12 shows an increase in force that is approximately 800 N in the third phase of operation, which is when the fluid is filling up the overhead tank. This appears reasonable given the potential of additional frictional effects inside the pipes. Since the fluid resistance can be seen in each test, the calculation is mostly used as a quality check that the pipes are not obstructed. Silicone oil can be considered a Newtonian fluid at this shear rate with a constant viscosity (Galland et al. [49]). For figure 4.12, an example of HNBR75 size 349 O-rings is shown, although this figure is simply a check of the fluid pressurisation calculation and validity. The raw values of fluid upwards force are directly observed during the experiment and the additional contribution can easily be subtracted from the measured total vertical force. Eq. 51 was used specifically during the design of the rig to ensure that the pipes used were appropriately sized to avoid excessive forces being generated by the pressurised fluid.

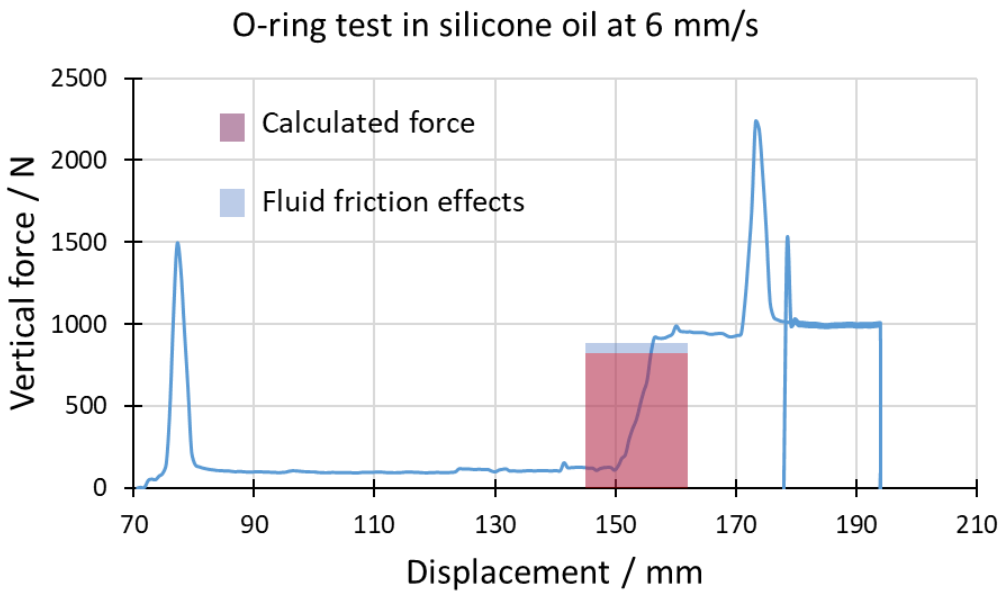

Fig. 4.12: Fluid resistance effects on the vertical forces that occur during the experiments. The observed force is subtracted from the total value during running friction in order to resolve the elastomer friction contribution.

Despite a large volume of fluid being required to fill the chamber, the amount of pressurised fluid in the gap between the O-ring seal and the piston was slightly less than 90 ml. Therefore, a high-capacity pump was not required. A 35 MPa rated pump was connected to the midpoint of the sleeve; once the seal was complete, pressurisation took place, and the pump was set to maintain a constant pressure. Leaks could have been detected by monitoring flow through the pump. Since the pump is set to maintain constant pressure, once the pump rate is below 0.05 mL/min, a no-leak condition can be assumed. At no point were leaks observed in the pressurisation part of the system. The contact pressure of the seals is enough (equal or higher) than that of the fluid. There are also no percolation paths between the rubber and the piston. Even though there is no way to observe the current contact of the seals, both conditions must be met in order to prevent leakage. Motion of the piston begins once the pump flowrate is reduced to less than 0.05 mL/min. At no point during testing were there any indication of leaks, either from a change in flowrate or by fluid leaking from the top or the bottom of the seal. Because oilfield pressure ratings are typically specified in imperial units, the internal pressurisation occurs with reference to values that are in hundreds of pounds per square inch (psi). The adopted pressure levels were as follows: atmospheric, 100 psi, 200 up to 500psi (which is in increment of 0.69MPa), 1000 psi, 1500 psi… 5000 psi (which is an increment of 3.45 MPa up to 35 MPa). The results are plotted consistently throughout using SI units.

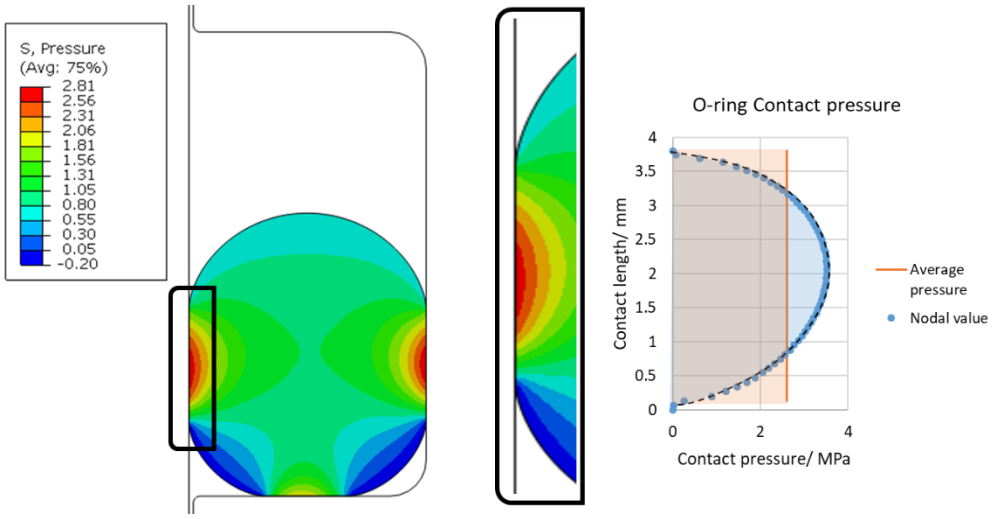

Fig. 4.13: An O-ring compressed axisymmetric model used to calculate the normal forces and contact pressures encountered during installation. The right-hand graph presents the difference between the local pressure (where each point represents the force imposed on a node) and the equivalent average pressure level between the linear elements. The areas under the blue curve and the orange curve are equal. All stress values are given in MPa.

All the FEA models presented in this thesis were calculated using Abaqus v6.18. The normal pressure response was calculated using an FEA axisymmetric model (Fig. 4.13) that adopted a simple stored energy function (SEF) approach where the rubber, a fluoroelastomer (FKM), was characterised in both tension and compression. The Yeoh model fit of the stress strain behaviour in both tension and compression is presented in Fig. 4.15. Both the sleeve and the piston were made from steel and were modelled as analytical rigid surfaces because of their large difference in elastic moduli when compared to that of the elastomer; this simplified the model and reduced computational effort. The elastomer component used hybrid elements together with enhanced hourglass control. Quad shaped elements with structured technique were used, as shown in Fig. 4.14, and the mesh size sensitivity study was undertaken manually until no discernible differences appeared in the results of two differently sized meshes. This was when a global seed size of 0.04 mm was used. Implicit solution domain was used throughout as the contact was straightforward and the rubber used in the model was assumed to be incompressible. Two steps were used for the simulation, the first one was to slide the piston down as the seal is fully made between the two O-rings. At this point the surface interactions between the O-ring and the sleeve (CoF) is not as relevant, since the output force of the O-ring compression is the only information required. This is better described in chapter 6 when looking at the different outputs with different friction models. The second step was used to apply the fluid pressure on the O-ring. Both steps used normal, hard contact interaction with the rigid surfaces. Pressure-penetration interaction type was used to simulate the fluid pressurisation.

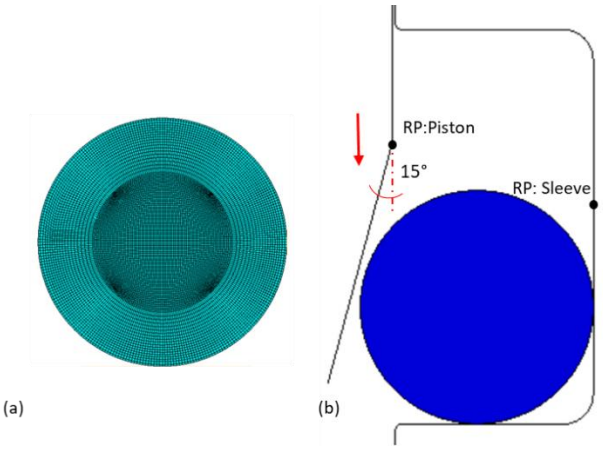

Fig. 4.14: (a) mesh for the O-ring axisymmetric model. (b) setting step of the simulation. The sleeve reference point is fixed in all directions and rotations. The piston reference point is fixed in the *X* and *Z* direction, it moves downwards until the seal is made

Contact pressure was not uniform along the O-ring surfaces (as is shown in Fig. 4.13). Elements in contact with the surface all have different levels of contact pressure. The circular cross section geometry of the undeformed O-ring model produces a maximum contact pressure that is broadly in the middle of the contact area. To calculate CoF versus pressure curves, the average contact pressure was calculated. This average must match the total forces that are present in the nodes in contact with the piston. In Fig. 4.13, both, the individual element value for contact pressure and the average value over the entire contact surface are shown. The average value was simply calculated as a function of the Abaqus output parameter CFN1 (normal force magnitude of the contact) over the CAREA (contact area) for the model. CFN1 was also used to calculate the normal force of the elastomer acting against the piston.

To validate our FEA results, a simple experiment was carried out in the form of an O-ring compression test. Using the curve fit obtained from the uniaxial tension results, an axisymmetric model of an O-ring of the same material was compressed up to 25% of the nominal strain, this was then compared to the results from a simple compression measurement on the O-ring. The instantaneous response was enough for the purpose of this dynamic friction studies, since the piston will cycle up and down, the frictional response is reversed in every half cycle, thus resetting the instantaneous response during each stroke.

Fitting of the measured data to the Yeoh stored energy function was performed using the data fitting algorithm in Abaqus and shows a good fit along the entire testing range (Fig. 4.15). Data was obtained from uniaxial testing in both tension and compression, as is discussed in detail in Chapter 3; for this case, the Yeoh model would be the ideal one due to its dependence on the first strain invariant only, as explained in Chapter 2. There are other, more precise variants of the Yeoh model that can provide better fits at low strain levels [50]. However, from an examination of the Abaqus curve fit, it was decided that the standard Yeoh model was a suitable fit for this work.

The derived coefficients for the Yeoh model are taken from Table 3.3: C_{10} = 1.26 MPa, C_{20} = -3.35 x 10^{-2} MPa, C_{30} = 1.47 x 10^{-3} MPa. A comparison of the measured and modelled values of the O-ring compression was made with the material properties being measured in uniaxial tension and compression. Fig. 4.16 shows that the test results and the prediction were close, and this developed a high level of confidence in the accuracy of the FEA model.

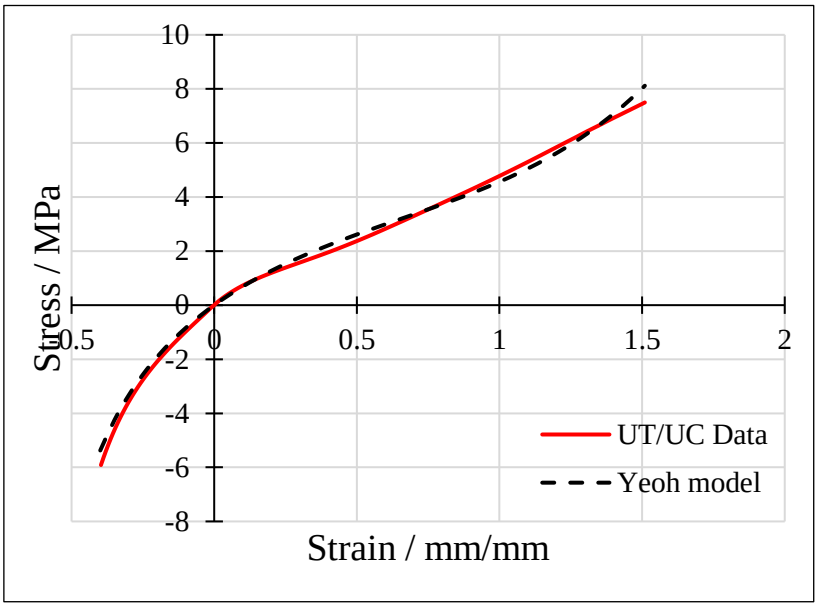

Fig. 4.15: An example of the uniaxial mechanical testing data fitted with Yeoh stored energy function for the HNBR 75.

With the previous uniaxial tension fit, we compress the same type of O-ring used in the rig in our validation experiment. Fig. 4.16 shows a good match between the model and the experiment. Although button compression and O-ring compression are very similar experiments, and a true model requires several other tests such as biaxial testing and pure shear, the model in question is simply done to test for the force output that comes from compressing the O-ring seal into the gland. For this, the model validation is seen as sufficient.

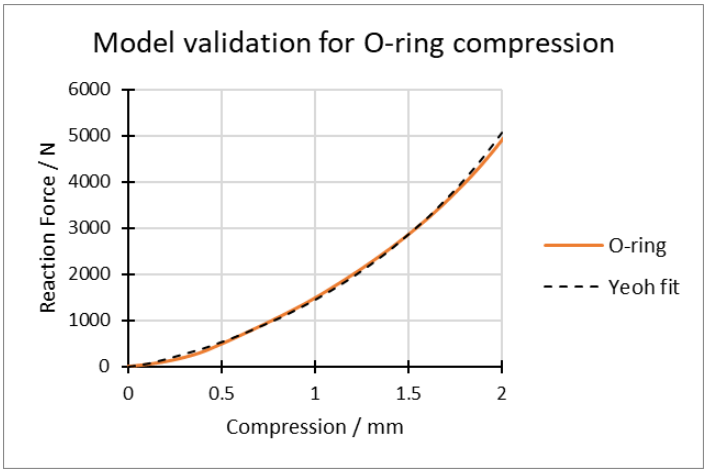

Fig. 4.16: Force vs. Compression length for the axisymmetric validation experiment.

Fig. 4.17 shows the stress profile of the O-ring when it is compressed in the glands machined within the sleeve and then subjected to different levels of internal fluid pressure. The friction model had only a very modest effect on the normal response of the elastomer at the higher pressures once a pressure dependent friction behaviour was adopted. At no point of the experiments was there leakage or breakdown of the O-ring simply arising from the initial pressurisation. No correction for the changes in SEF due to the increase in the hydrostatic pressure was introduced, since it was assumed that the elastomer behaviour remained largely unchanged in terms of its stress response.

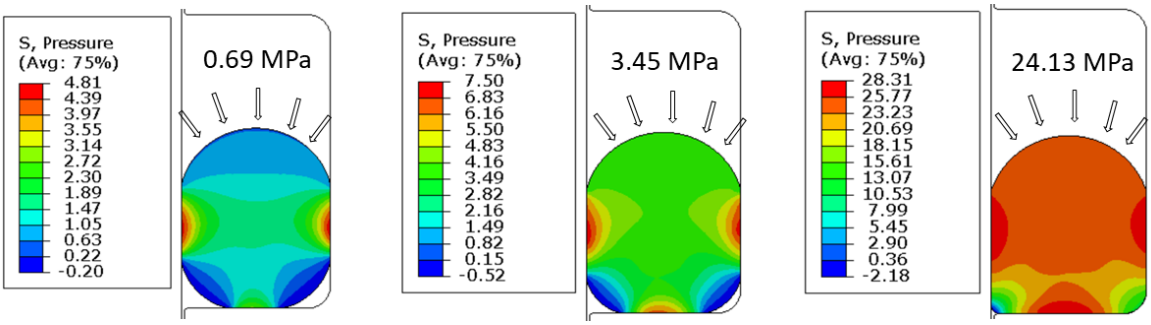

Fig. 4.17: O-ring axisymmetric model compressed with three different hydrostatic pressure values at 20°C. Left to right: 0.69, 3.45 and 24.13 MPa.

All the average pressure outputs coming from the normal forces and the contact area are tabulated in Tables 4.2-4.7. FKM rubbers were not tested at 24% compression glands due to lack of availability and high costs of FKM large O-rings (10 to 20 times that of styrene butadiene rubber (SBR), rubber very commonly used in friction studies).

Tables 4.2 to 4.7 compare the results of simulations for all O-ring/gland combinations, results that are missing are points where the deformation on the lip of the seals is too high. Observing the “contact pressure” columns of the tables, some patterns arise. When it comes to temperature changes, all HNBR materials have a minimum at 60°C, before rising again when they reach 120°C. When filled rubbers are heated up, two things happen: the polymer part of the rubber compound is stiffened, the polymer chains have higher entropy and try to come out of an aligned state, making it difficult to stretch the rubber; secondly, thermal expansion breaks down the filler network and makes it easier to stretch it. These two things have opposing results, where from 20°C to 60°C this filler network breakdown takes precedence and softens the rubber compound more than the chains can stiffen it; between 60°C and 120°C, the polymer chain stiffening becomes more dominant, giving the rubber some of its stiffness back.

Table 4.2: FEA results of 13% compression gland of the novel friction rig for HNBR75. The material models used for these calculations are taken from chapter 3.

	HNBR 75					
	13% Compression gland					
	20°C		60°C		120°C	
FLUID PRESSURE (MPA)	Contact area (mm^2)	Contact pressure (MPa)	Contact area (mm^2)	Contact pressure (MPa)	Contact area (mm^2)	Contact pressure (MPa)
0.00	800	1.82	792	1.50	800	1.82
0.69	963	2.07	883	1.97	963	2.07
1.38	1072	2.44	958	2.50	1072	2.44
2.07	1149	2.89	1028	3.06	1149	2.89
2.76	1304	3.11	1067	3.68	1304	3.11
3.45	1370	3.53	1139	4.16	1370	3.53
6.89	1227	7.47	1235	7.34	1227	7.47
10.34	1269	10.62	1302	10.46	1269	10.62
13.79	1302	13.92	1341	13.60	1302	13.92
17.24	1338	17.10	1344	17.05	1338	17.10
20.68	1348	19.86	1361	20.27	1348	19.86
24.13	1333	23.88	1366	23.65	1333	23.88
27.58	1335	27.35			1335	27.35
31.03	1338	30.79			1338	30.79
34.47	1340	34.26			1340	34.26

Table 4.3: FEA results of 24% compression gland of the novel friction rig for HNBR75. The material models used for these calculations are taken from chapter 3.

	HNBR75					
	24% Compression gland					
	20°C		60°C		120°C	
FLUID PRESSURE (MPA)	Contact area (mm^2)	Contact pressure (MPa)	Contact area (mm^2)	Contact pressure (MPa)	Contact area (mm^2)	Contact pressure (MPa)
0.00	1357	3.20	1310	2.71	1359	3.20
0.69	1357	3.47	1355	3.22	1359	3.47
1.38	1358	3.80	1403	3.76	1359	3.80
2.07	1391	4.08	1454	4.30	1392	4.08
2.76	1427	4.37	1483	4.91	1426	4.37
3.45	1460	4.69	1512	5.54	1461	4.69
6.89	1583	9.14	1623	8.60	1583	9.14
10.34	1633	12.36	1658	11.87	1633	12.36
13.79	1692	15.38	1686	15.10	1692	15.38
17.24	1708	18.75	1697	18.43	1707	18.76
20.68	1718	22.15	1702	21.78	1718	22.15
24.13	1677	25.76	1704	25.17	1676	25.78
27.58	1682	29.18	1705	28.58	1682	29.18
31.03	1688	32.56			1688	32.56
34.47	1688	35.99			1688	35.99

Table 4.4: FEA results of 13% compression gland of the novel friction rig for HNBR 90. The material models used for these calculations are taken from chapter 3.

	HNBR 90					
	13% Compression gland					
	20°C		60°C		120°C	
FLUID PRESSURE (MPA)	Contact area (mm^2)	Contact pressure (MPa)	Contact area (mm^2)	Contact pressure (MPa)	Contact area (mm^2)	Contact pressure (MPa)
0.00	772	4.46	782	2.21	794	2.83
0.69	790	4.93	841	2.68	838	3.28
1.38	816	5.47	889	3.24	884	3.78
2.07	850	6.00	939	3.80	917	4.35
2.76	870	6.70	974	4.41	951	4.92
3.45	910	7.22	1009	5.00	986	5.48
6.89	1018	10.21	1106	8.20	1114	8.37
10.34	1089	13.22	1184	11.32	1176	11.60
13.79	1139	16.35	1207	14.77	1236	14.64
17.24	1167	19.64	1248	17.87	1259	17.96
20.68	1193	22.85	1271	21.07	1282	21.17
24.13	1219	25.95	1285	24.36	1296	24.46
27.58	1244	28.97	1308	27.40	1319	27.52
31.03	1247	32.47	1310	30.84	1320	31.00
34.47	1249	35.96	1311	34.29	1322	34.44

Table 4.5: FEA results of 24% compression gland of the novel friction rig for HNBR 90. The material models used for these calculations are taken from chapter 3.

	HNBR90					
	24% Compression gland					
	20°C		60°C		120°C	
FLUID PRESSURE (MPA)	Contact area (mm^2)	Contact pressure (MPa)	Contact area (mm^2)	Contact pressure (MPa)	Contact area (mm^2)	Contact pressure (MPa)
0.00	1258	9.02	1302	4.85	1299	6.12
0.69	1277	9.09	1345	5.30	1320	6.63
1.38	1296	9.54	1369	5.85	1365	7.04
2.07	1316	10.00	1393	6.42	1389	7.58
2.76	1336	10.48	1418	7.00	1391	8.24
3.45	1356	10.96	1444	7.57	1416	8.79
6.89	1421	13.77	1547	10.57	1496	11.83
10.34	1490	16.63	1605	13.68	1573	14.78
13.79	1539	20.22	1608	17.17	1603	18.02
17.24	1566	23.16	1638	20.34	1634	21.14
20.68	1592	26.67	1640	23.79	1636	24.59
24.13	1618	29.82	1642	27.25	1638	28.05
27.58	1621	32.88	1676	30.13	1640	31.51
31.03	1623	36.34	1677	33.54	1673	34.32
34.47	1648	41.66	1677	36.97	1674	37.73

The FKM materials do not follow the same compensation behaviour in these ranges, the lower hardness FKM actually stiffens with the change from 20°C to 60°C, and only decays in stiffness slightly between 60°C and 120°C. The higher hardness FKM stiffness decays completely with increasing temperature, noting that the filler network breakdown is the dominant factor here. It is to be expected, as higher hardness rubbers compounds have higher amount of fillers.

One thing that is noticeable in all cases, is that when the highest levels of pressures are reached, the difference between temperature ranges gets smaller. The absolute value of contact pressure and area might be similar (or even slightly greater sometimes), but when speaking in relative terms, the differences are smaller. At this point, the contact pressure of the elastomer comes (mostly) from the pressurised liquid, and not from the rubber mechanical properties.

Table 4.6: FEA results of 13% compression gland of the novel friction rig for FKM 75. The material models used for these calculations are taken from chapter 3.

	FKM75					
	13% Compression gland					
	20°C		60°C		120°C	
FLUID PRESSURE (MPA)	Contact area (mm^2)	Contact pressure (MPa)	Contact area (mm^2)	Contact pressure (MPa)	Contact area (mm^2)	Contact pressure (MPa)
0.00	801	1.35	770	1.66	786	1.54
0.69	893	1.83	856	2.10	872	1.99
1.38	961	2.40	933	2.71	950	2.59
2.07	1032	2.96	1009	3.29	1010	3.22
2.76	1104	3.48	1050	3.94	1070	3.81
3.45	1144	4.08	1092	4.56	1128	4.36
6.89	1270	7.17	1222	7.61	1224	7.56
10.34	1344	10.19	1270	10.81	1273	10.75
13.79	1347	13.61	1298	14.03	1301	13.98
17.24	1349	17.04	1305	17.44	1308	17.38
20.68	1350	20.47	1311	20.83	1312	20.81
24.13	1351	23.90	1315	24.27	1313	24.27
27.58	1352	27.34	1317	27.73	1314	27.74
31.03	1382	30.13	1318	31.21	1331	31.20
34.47	1384	33.47	1334	34.29	1315	34.71

Table 4.7: FEA results of 13% compression gland of the novel friction rig for FKM 90. The material models used for these calculations are taken from chapter 3.

	FKM90					
	13% Compression gland					
	20°C		60°C		120°C	
FLUID PRESSURE (MPA)	Contact area (mm^2)	Contact pressure (MPa)	Contact area (mm^2)	Contact pressure (MPa)	Contact area (mm^2)	Contact pressure (MPa)
0.00	801	3.16	770	2.74	786	2.51
0.69	831	3.65	804	3.22	804	3.06
1.38	862	4.18	859	3.84	876	3.61
2.07	894	4.72	914	4.43	914	4.29
2.76	959	5.10	952	5.07	971	4.84
3.45	962	5.81	991	5.67	1026	5.35
6.89	1107	8.56	1132	8.62	1153	8.37
10.34	1187	11.61	1200	11.70	1202	11.61
13.79	1230	14.83	1228	14.97	1250	14.65
17.24	1298	17.55	1253	18.19	1258	18.07
20.68	1301	21.02	1279	21.30	1284	21.17
24.13	1346	23.76	1286	24.66	1288	24.58
27.58	1347	27.19	1292	28.04	1291	28.00
31.03	1348	30.62	1296	31.46	1293	31.44
34.47	1349	34.04	1298	34.90	1293	34.91

4.3 Lessons Learned and Particularities of the Rig

Before testing the commercial materials that had been identified for these frictional studies, a large pack of 70D (Shore A) Nitrile O-rings were bought to test the usability of the rig and observe any particular effects that might occur during testing. Several issues were identified from this preliminary set of tests including: the effect of stress relaxation on the normal force during the test, the possibility of surface roughness changes across a number of tests, and the assumption of no physical cracking during the initial setting of the O-rings. Concentricity was required to ensure no movement of the seals in order to avoid leaks and potential setting eccentricity of the rig.

To test the effects of stress relaxation on the elastomer response, a single O-ring was engaged and ran through roughly half the piston's length. Most of the effect of stress relaxation occurs in the first few seconds[24]. To observe an extreme case of relaxation time, a time of 12 hours was selected to observe changes in the behaviour. After the O-ring was fully engaged, the piston came to a stop and a 12 hour hold time was adopted. After this 12-hour hold time, the sliding experiment was restarted, and the frictional forces were measured. Figure 4.18 shows the frictional force output of this experiment. The vertical drop of force after a displacement of 100 mm is the point where the piston was held in position for 12 hours. Once restarted, there is a noticeable jump in the frictional force, with

a small peak before the continuous movement. This peak results from a combined effect of adhesional friction and stress relaxation. The rubber will relax and fit into the surface roughness of the piston, increasing the real contact area. Once the piston continues to slide, the peak drops and the value becomes steady until the 187 mm mark at the end of the stroke.

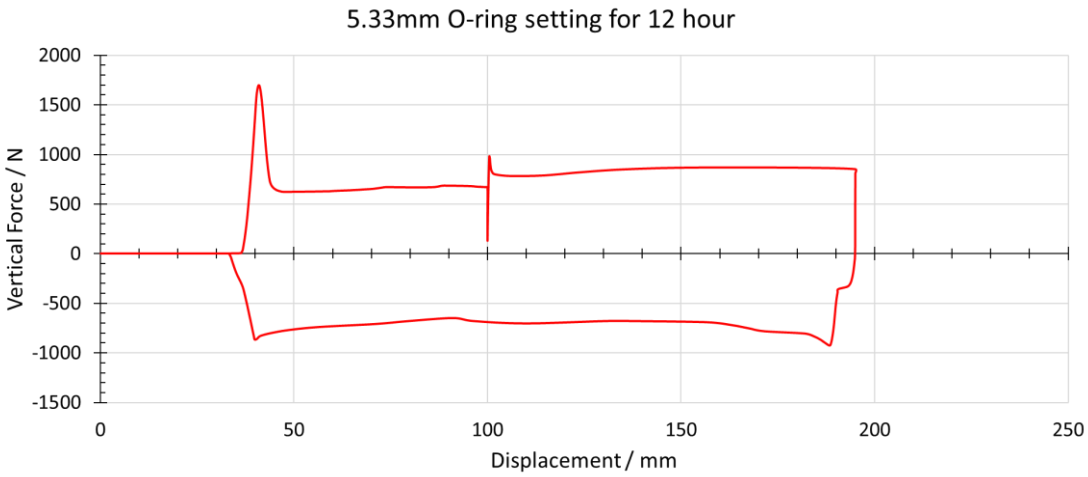

Figure 4.18: Frictional force output for a 70D Nitrile O-ring after a 12 hour hold at 100 mm displacement distance. The return frictional values show no effects from the stress relaxation

It is initially thought that stress relaxation would decrease the frictional response in the seal, this is not the case. The stress relaxation behaviour is only observed qualitatively, for the moment, because these are dummy runs to determine if further testing and actual quantitative data is required. Since the material has relaxed (albeit an unknown amount), the total area of contact is increased and the adhesional component is likely to be creating a greater contribution. On the reverse stroke however, the O-ring is now dragged in the opposite direction, and the area under stress changes, eliminating the effect of stress relaxation with each cycling of the piston. This means that the average frictional forces return to their pre-stress-relaxation values. Because the CoF values that are tested for this research, occur in the average of 6 cycles of strokes for each pressure level, whatever effect stress relaxation might have on the seal has disappeared after the first cycle. Since the focus of the project is to observe the running friction, the value after the last cycle does not involve stress relaxation effect. To include stress relaxation behaviour for each cycle/test would increase the experimental time of the project beyond what is acceptable. It is considered then that the effects of stress relaxation are beyond the scope of this work. But this experiment highlights that it cannot be ignored for any friction system with extensive dwell times and single cycle situations. This study does not have dwell time between cycles.

When rubber materials are in constant sliding action against a surface, it is common for the carbon black particles close to the surface to start abrading the metal. If this is ongoing then there may be measurable changes to the surface roughness. These in turn might change the frictional behaviour, both the adhesion and the hysteretic contributions.

Since the investigation of rubber friction is to be done across hundreds of runs, the friction response must remain constant from the first measurement to the last one. To test the validity of frictional force results, the initial nitrile O-ring tests were done across a span of 6 months, laboratory conditions are maintained (temperature and velocity) but some environmental conditions have a slight difference (10 kN load cell → 50kN load cell). For each test, a pair of virgin O-rings was used. The O-rings were stored in opaque black zip bags, inside sealed cardboard boxes, in dry-humidity controlled rooms to avoid contamination. According to ISO 2230, NBR parts can be stored for up to 7 years without any effect on their properties. The results of two tests 6 months apart are highlighted in figure 4.19.

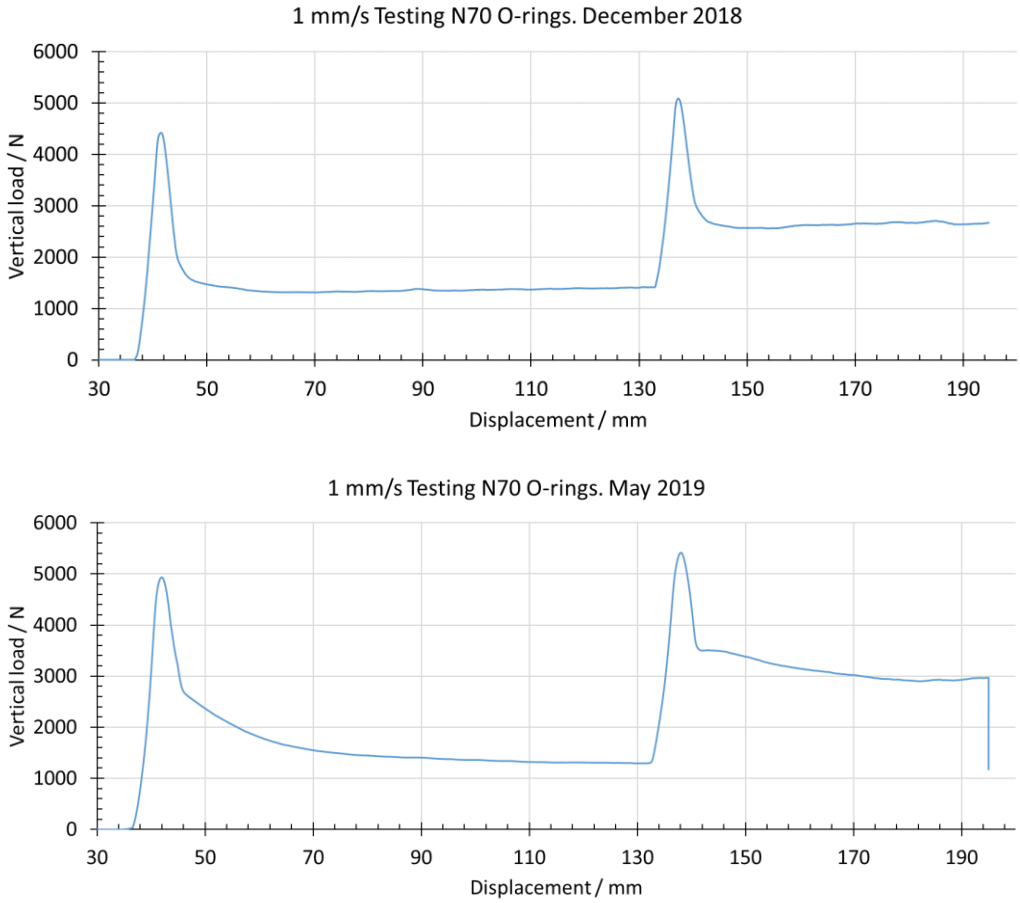

Figure 4.19: double O-ring insertion test for 70D Nitrile O-rings on the same piston 6 months apart. Besides the initial drop of tension after insertion, the running friction values remain. The second O-ring has a slight increase that might be caused by variability within the rubber batches.

A double O-ring insertion was done at the same temperature in May 2019 and then compared to an earlier one done in December 2018. Because of the high costs (and low availability) of HNBR and FKM O-rings, these tests that would observe changes in the piston were performed using the cheaper NBR alternative. Once the tension is stabilised after insertion, there is very little difference between the two tests. As long as the initial drop after the peaks has passed, there is no indication of changes in the surface tangential

forces. There will always be the possibility of differences between different rubber batches, but the piston surface appeared to remain a constant. To confirm this theory, further profilometry testing was done on the pistons to ensure constant values and there were no observable changes from the first day of testing to after the last test was done.

The third concern of the new testing rig was how to observe possible failures in the O-rings before any fluid pressure had been added into the experiment. A failure in the O-ring during setting would almost certainly result in a leak during the fluid pressurisation phase. Not only is it an environmental concern to spill silicone oil, but it is also a safety one in terms of slippage and high temperature testing.

From figures 4.18 and 4.19 we can observe that, although the increase in frictional forces was high during setting, the peak of the curve had a rather smooth transition. When peaks are sharp and abrupt, or when the setting force is unusually high as is shown in the case highlighted in Fig. 4.20, it was indicating that either O-ring extrusion or material fracture had occurred.

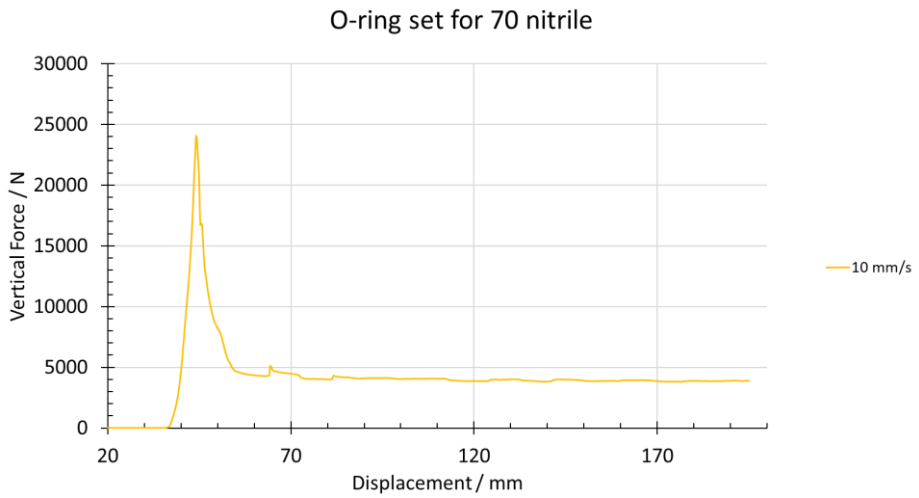

Figure 4.20: O-ring set for Nitrile rubber at 10 mm/s. The initial force peak is much sharper than the ones in regular experiments.

Once the sharp peaks are observed, or when a peak is divided into two (Fig. 4.22) the test process was stopped, and the O-ring's integrity was rechecked. This avoided not only potential risks of a leak, but also potential damage to the piston. From figures 4.21 and 4.23, it is noticeable that the O-ring fractures are not perfectly symmetrical. If there is material between the piston and outside of the gland, the eccentricity is lost and can lead to unwanted scratches on the piston surface.

Figure 4.21: Nitrile O-ring used for the experiment plotted in Fig 4.20. The figure on the left shows the bottom of the sleeve with the shavings of the cleaved material. The figure on the right is the O-ring after the test with all the fractured material shown.

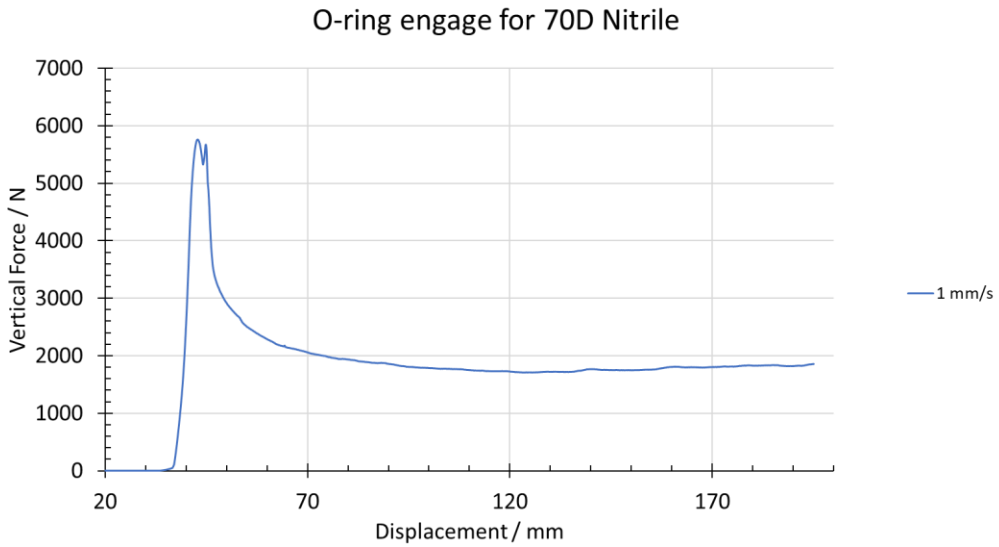

Figure 4.22: O-ring set for Nitrile rubber at 1 mm/s. The initial smooth force increase is followed by a small sharp peak, indicating a second shearing of the material.

Figure 4.23: Nitrile O-ring used for the experiment lined out in Fig 4.22. The O-ring has clear signs of damage during insertion.

Tests that produced sharp peaks were quite uncommon. With good concentric alignment of the piston and well lubricated O-rings, failure during setting was a rarity. But recognising when a test was failing helped alleviate any environmental and safety concerns.

With the rig fully built, tested, and its behaviour analysed, the entire test regime was laid out in efficient manner to observe the behaviour of frictional forces in four different types of elastomers with varying pressure, velocity and temperature.

Overall, the rig proved to be excellent for what was needed. It was able to sustain the 35 MPa pressure without leaking, deformation or failure. The data from the friction experiments was as described in figure 4.11. allowing for ease of reading of frictional forces. The company that sponsored the entire research project is now in possession of the rig and continues to use it for friction experiments.

Total experiments are as follows:

For HNBR: three temperature values, two levels of compression, two different materials, fifteen points of pressure, two surface roughness profile, six different velocities. For a total of 2160 data points. For FKM: three temperature values, one level of compression, two different materials, fifteen points of pressure, three different velocities, two roughness profiles. For a total of 540 data points. It is important to note that every O-ring undergoes all the pressure tests, reducing the number of O-rings required to be about 180. This entire testing stage took two years, between fine-tuning the rig and checking for best-practice, along with the slower velocities. The culmination of two years of experimental work, the results and rationalisation for the frictional behaviour is laid out in chapter 5.

5. Experimental Friction Results

A detailed experimental programme was undertaken that characterised the O-ring frictional behaviour for all four elastomers (HNBR 75, HNBR 90, FKM 75 and FKM 90) at each of the three temperatures (20°C, 60°C and 120°C) characterised in Chapter 3. This full set of working results demonstrates how the friction behaviour is surface topography, pressure and velocity dependent for all the materials across the operating temperature range. Utilising the measured profilometry of the steel sliding surfaces allowed each of the measured sliding speeds to be translated into a characteristic frequency of deformation. This enabled a comparison of these results to the theories explained in Chapter 2 to be made to verify their validity when working under these extreme conditions. Detailed data analysis is presented for a specific elastomer to examine how every variable affects the frictional behaviour in general. Once the detailed methodology had been completed the entire data set is presented in a single simple graphical format for each material.

5.1 Repeatability

A detailed design of experiments (DoE) was undertaken following initial talks with the sponsoring company. Knowing that it could take 1-3 hours to set up and prepare the rig for each test meant that compromises were made when it came to the number of tests that we could undertake as part of this study. The target number of potential tests are presented in Table 5.1. Although many variables are of interest for the research, the elimination of certain variables to reduce experiments was done by the availability of testing equipment and expertise of field experts. What was considered most urgent by the sponsor was the main reason behind variable selection.

Table 5.1: Design of experiments showing the full number of experiments required for this detailed investigation.

Variable	**Amount**
Elastomer material	4
Velocity	6
Temperature	3
Pressure	15
Gland size	2
O-ring size	2
Surface roughness	2
Total	**8640**

If a single measurement was made of every possible combination for all of these variables, then there would be a requirement to undertake 8640 test runs. Judicious experimental design allowed this to be reduced to approximately 2000 experiments. This meant that repeating each test for statistical variation was impossible within the timeframe of this study. Since friction in rubber is most variable at low pressure levels, there are 6

measurements at low pressure (every 0.69 MPa) and after 3.5 MPa, changes to every 3.5 MPa. This allows for a complete analysis of the decay of CoF with increasing pressure, whilst saving time for tests at higher pressures. However, throughout the test programme certain specific tests were repeated to test the system was still producing the same data for a specific material under specific set test conditions. Fig. 5.1 for example shows data for HNBR 75 that had been run approximately one year apart under dry conditions with just a single O-ring in position against the same piston surface, at a sliding velocity of 1 mm/s.

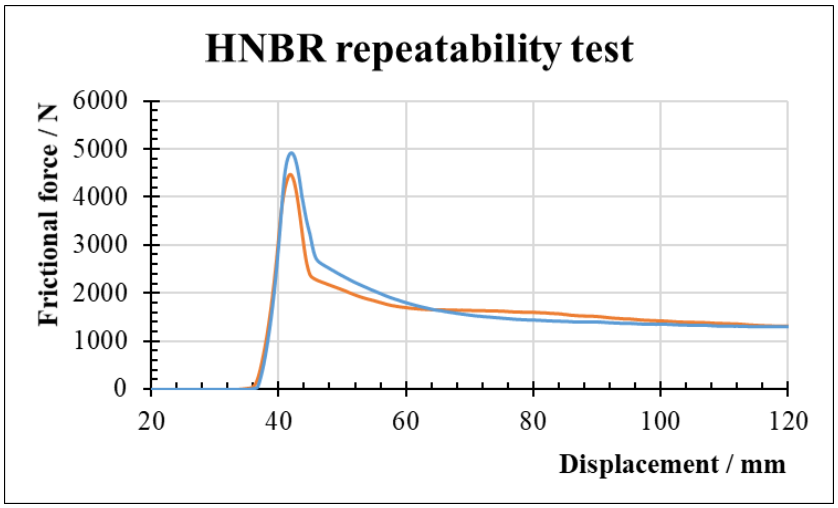

Fig. 5.1: Repeat of a dry HNBR 75 test at 1mm/s a year apart. Blue line represents a test done in early 2019, orange line was done in early 2020This confirmed integrity of the surface and repeatability of the test.

This level of repeatability was typical for all the spot tests that were undertaken throughout the study. Also, each test was repeated through several test cycles as is explained in Chapter 4. This level of reproducibility gave us confidence that our testing procedure was robust, and it allowed us to calculate the variability of our experimental data which was pleasingly and remarkably low.

Figures 5.2 to 5.5 show all the results for the friction tests of all four materials. The CoF is plotted against the face pressure to observe patterns and show typical behaviour. The plots also include all levels of speed. Even though CoF vs. Speed is to be observed later, we can also draw initial conclusions whilst looking at these figures. Once all the cases of these tests are mentioned, the physical effects of the variables are discussed in later sections (5.2 onwards) when it comes to the effects of variables and how to better define environmental conditions

When it comes to the HNBR 75(figure 5.2), one of the first things that draws attention is the lack of results for piston B. During runs with piston B, all HNBR 75 samples failed when tested at 20°C and 120°C, only when tested at 60°C would they pass the test. This could be attributed to the higher roughness of piston B. As observed in the mechanical testing of the HNBR, the modulus of the 75-hardness rubber decreased when heated to 60°C and then increased again when temperature rose to 120°C. This lower modulus apparently allowed the rubber to deform more easily when compressed, and the crack

resistance of the rubber (although not tested) did not decay enough to cause cracks to take place during setting on the rougher surface.

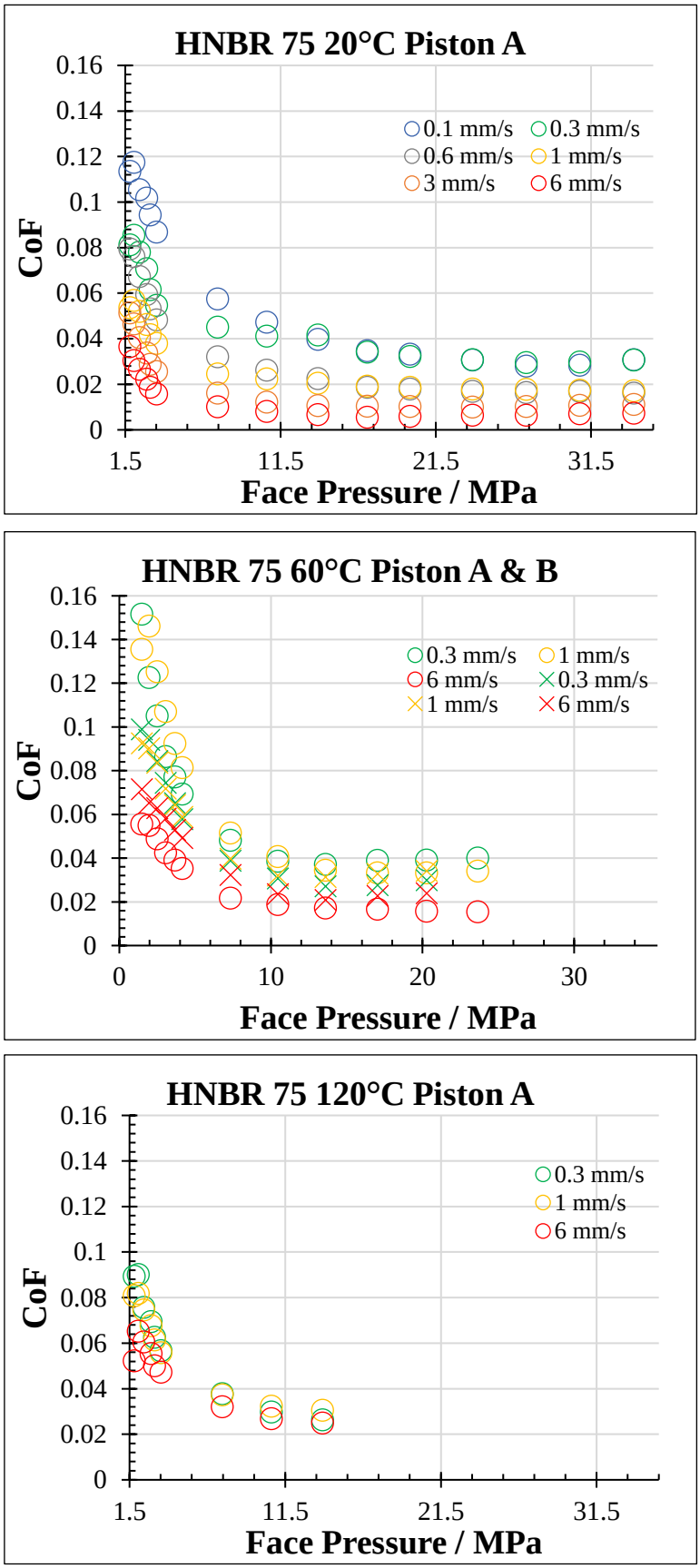

Fig 5.2: HNBR 75 friction tests results. Higher temperature testing uses less velocities due to material limitations. Material also failed most tests with piston B (extrusion).

The range of testing (in terms of pressure) is also limited for HNBR75 samples. For the lowest temperature, the full range of 35 MPa was reached without an issue. As we go higher in terms of temperature, the rubber begins to extrude/fail at lower levels of pressure, failing at 25 and 13 MPa for 60°C and 120°C respectively. Increasing the temperature caused a reduction of pressure capacity upwards of 50%. Differences between velocities ranges are also observed, with increasing velocities generating lower CoF. In the only occasion where both pistons are tested, there is a particular behaviour about the friction. At the lowest velocities, the rougher piston does not generate higher friction values, it only does so at the higher velocity ranges. It appears that at this point in temperature and velocity, the rubber is not touching most of the peaks of the surface, generating higher frequency of deformation. At the highest temperatures, the pattern of higher velocities associating with lower friction remains true, but the difference between all ranges of velocity becomes minimal. An explanation for this, is that at this temperature level, the rubber is soft enough to deform into the surface even at higher velocities.

The tests for HNBR 90 (figure 5.3) did not present the same level of failures that the HNBR 75 had. Higher hardness allowed for minimal extrusion during the entire pressure testing range, for both pistons. Lack of material did not allow for full testing velocity ranges at the higher temperatures. For this, it was decided to move between: lowest, medium and highest velocity levels. This remains the case for the rest of the elastomers, the cost of FKMs and HNBRs was a limitation (along with time) for a full spectrum of tests.

At the 20°C level, the clear distinction between roughness is observable, with piston B having higher friction levels (although not by much), this is much more noticeable at higher speeds. There is a clear difference between piston B and piston A when it comes to velocity effects. The gap between the slowest speed in piston A is much larger than in piston B. This trend holds true for 60°C and 120°C. Both at the low-, and high-pressure testing ranges.

When observing the higher temperatures, it is also noticeable that initial levels of friction are higher. Lubricant thinning will be presented as the explanation for this in a later section. Thanks to its mechanical properties, high pressure testing ranges can be evaluated for HNBR 90, as opposed to its lower hardness counterpart and the FKM elastomers.

For FKM 75 (figure 5.4) and FKM 90 (figure 5.5) cost considerations restricted the full range of testing. But results from both pistons at all temperature levels were obtained with reduced velocity ranges.

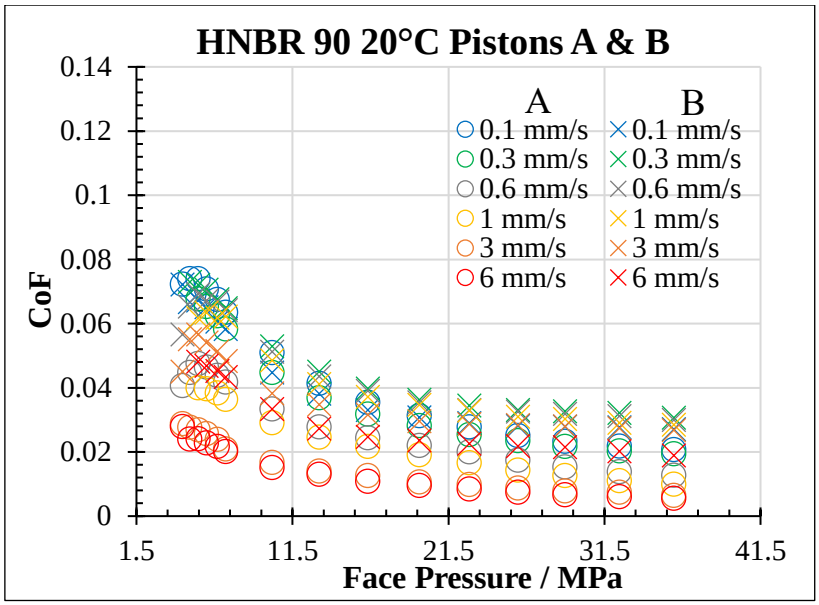

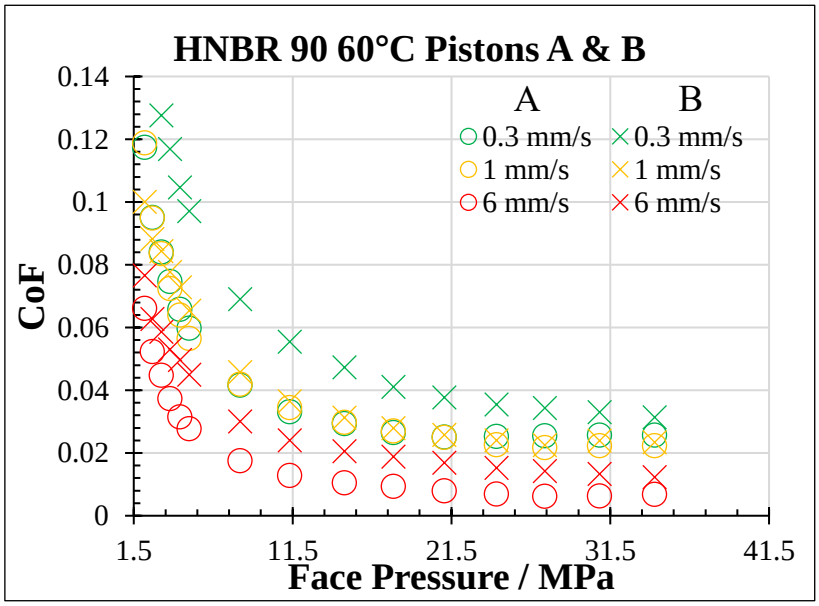

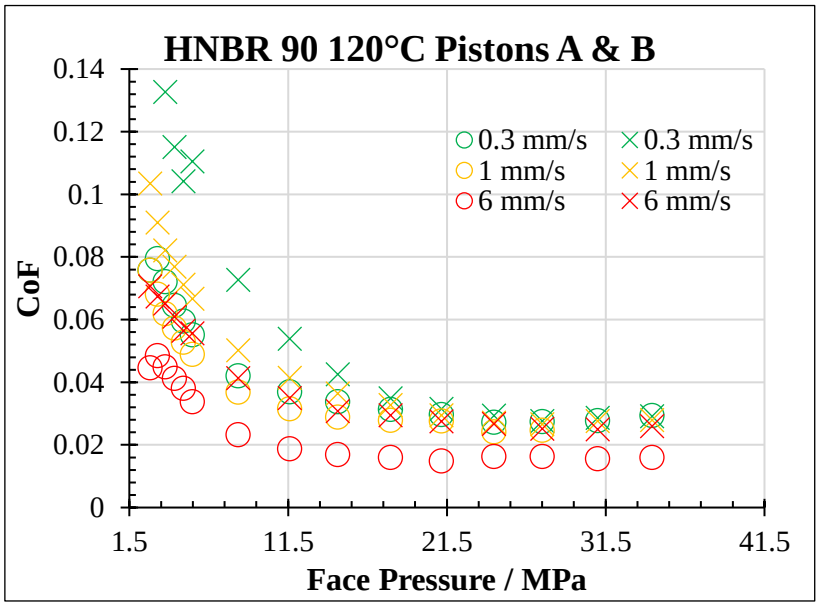

Fig 5.3: HNBR 90 friction tests results. Higher temperature testing uses less velocities due to material limitations.

FKM 75 presented some challenges for friction testing. The tear resistance of the material was noticeable lower when compared to the higher hardness counterpart, and the HNBR rubbers as well. There is no indication of extrusion for 20°C tests, but during the 60°C Piston B tests, once the face pressure reached 15 MPa the CoF start increasing. This could indicate two things: a displacement of the lubricant due to increased contact pressure, or extrusion events in the O-ring gland. Since these conditions did not increase friction for elastomers of the same hardness, the conclusion appeared to be an extrusion, which could cause failure in the O-ring. This was confirmed after the tests, O-rings showed cracks just like the ones presented in chapter 4. The same incidents happen at 120°C for both pistons after 15 MPa. Higher temperatures showed to decrease mechanical properties to a point where the O-rings would constantly extrude.

For FKM 90, the events are somewhat similar. Higher temperatures and higher velocities came with higher CoF. Piston B remains the one with higher CoF for the highest velocities in all cases.

In terms of extrusion and seal failures, the higher hardness remains to be the factor that allows us to evaluate a wider range of pressure levels. Whilst there were still some failures and points of extrusion, these cases were limited to pressures above 30 MPa, double the value achieved with FKM 75.

When observing the entire range of tests, the elastomer that is best suited for high pressure/high temperature applications in terms of friction is HNBR 90. It has the highest resistance to extrusion given its mechanical properties, allowing for a wide range of pressure and temperature. Under dry conditions, FKM is normally the best material friction-wise, but given the lubrication against the smooth surface, the FKM advantages is not noticeable, making HNBR 90 the best suited one for lubricated conditions.

Overall, there were several patterns recognisable during the entire range of testing for the elastomers. A few key points are obtainable:

- In accordance with literature findings, higher pressure levels showed a lower CoF.
- Higher velocities showed a consistent drop in CoF.
- Higher temperatures were associated with higher CoF.
- Rubber type was not too determinant on the outcome of frictional values.
- Friction values are so low, that viscous flow from the lubricant and hysteresis effects could be attributed with the entirety of tangential effects.

From chapters 5.2 onwards, all the variables, and how they contribute to the coefficient of friction are explained. In order to avoid confusion (given the large number of data points), each variable is typically presented with a single case for a specific material. This allows for easier visualisation of the variable effect. Any particular results can always be observed once again when coming back to this section.

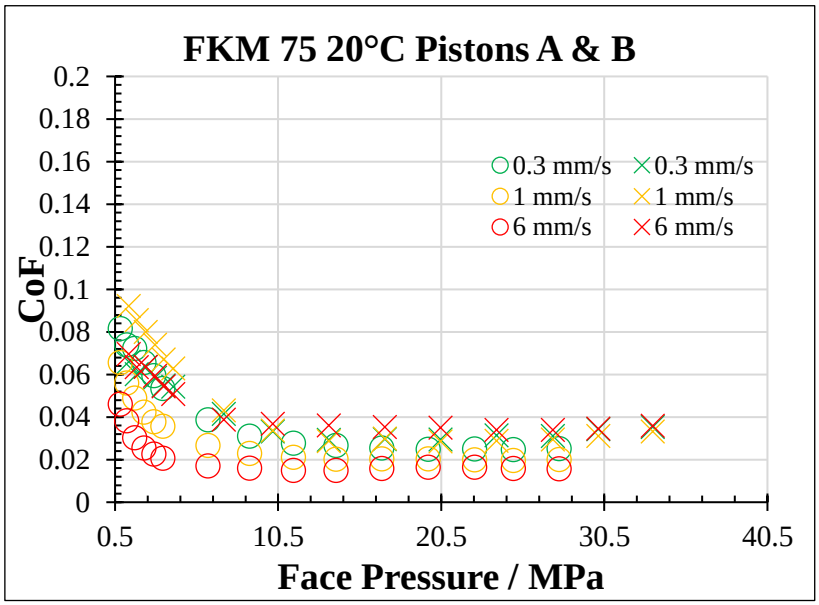

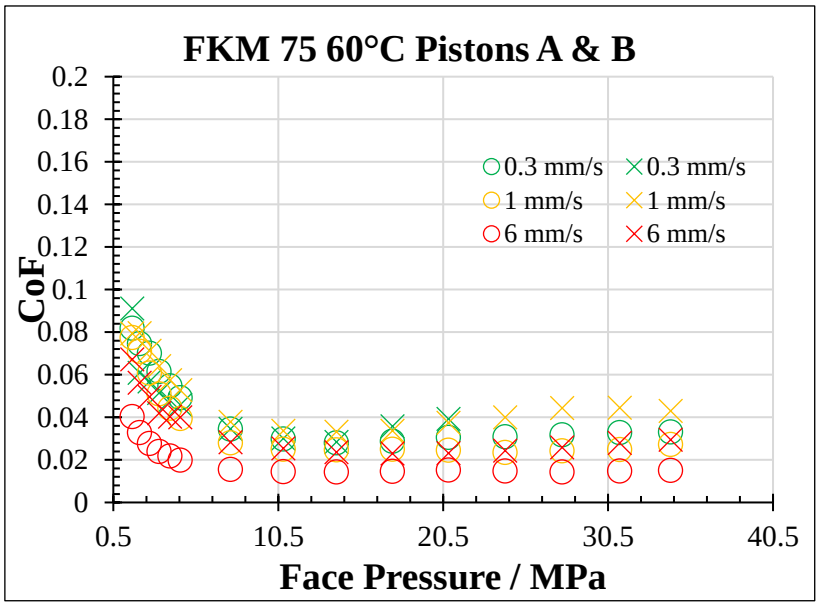

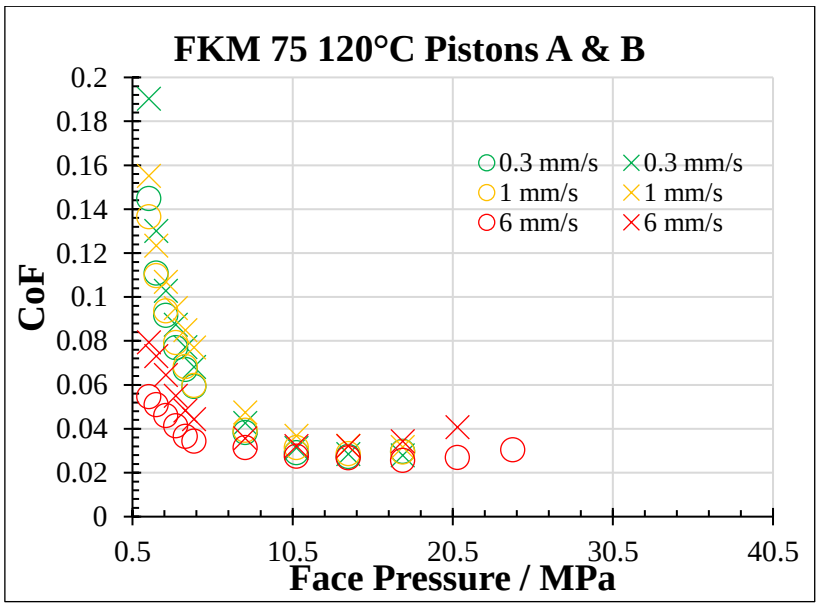

Fig: 5.4: FKM 75 friction tests results. Material limitations is the reason for lower number of velocities used during testing.

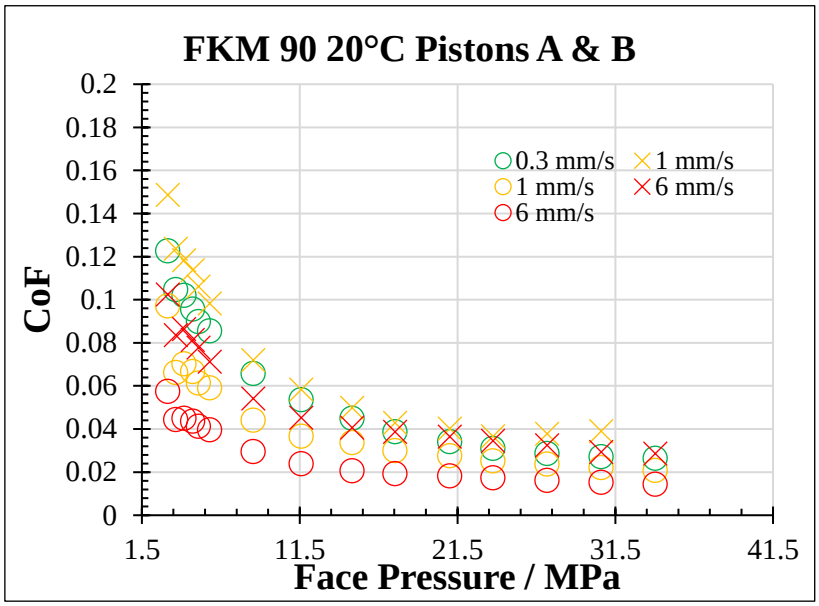

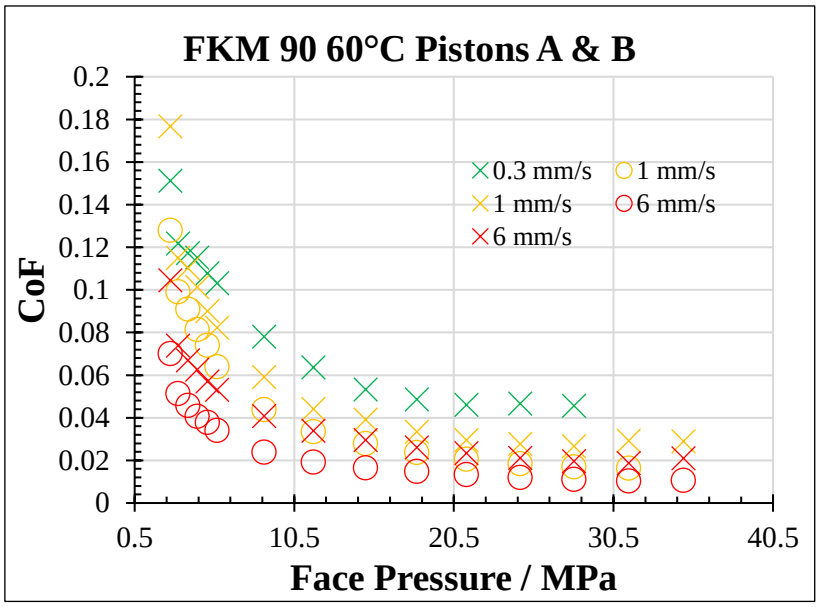

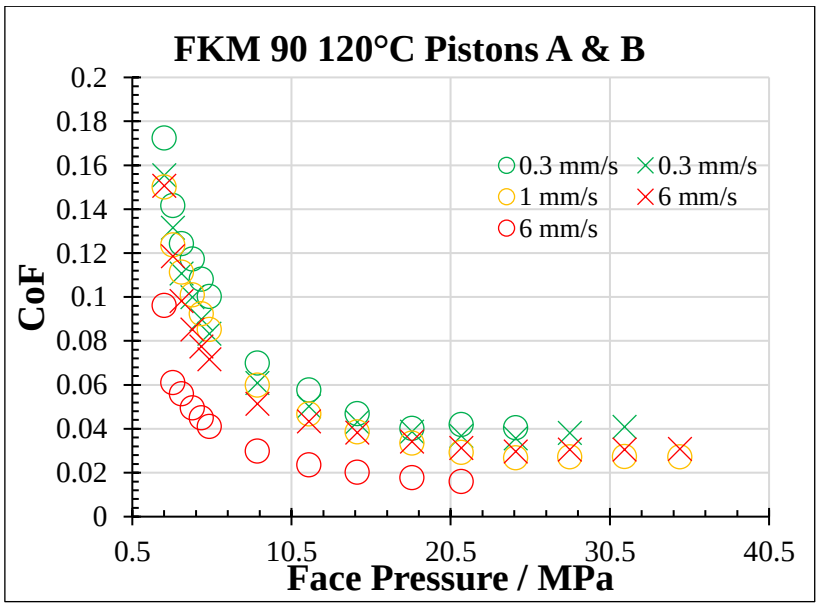

Fig 5.5: FKM 90 friction tests results. Material limitations is the reason for lower number of velocities used during testing.

5.2 The Effect of Pressure

As is discussed in the friction section of Chapter 2, the pressure effects on the coefficient of friction (CoF) of a sliding rubber surface are well known. In the case of our test rig the amount of the pressure applied initially depends upon the level of precompression that the O-ring is subjected to during insertion. This pressure is then ramped up to potentially very large levels by the application of additional pressurisation of the silicone oil injected into the annular chamber between the two O-rings. Throughout all the testing there was no pressure loss or oil leak associated with the test fixtures. Tests that indicate damage of the O-ring manifested themselves by erratic force readings and were eliminated due to the unpredictability of contact area. There are occasions in which extrusion of the O-ring into the extrusion gap was observed. In these cases, the CoF was seen to ramp up again with further increases in pressure. This would signal that the ring was about to fail.

Fig. 5.6 shows how, for one material (HNBR 75) at one test temperature (20°C) against one specific sliding surface, the coefficient of friction depends upon the pressure using this test approach. This figure confirms that a decrease in the CoF with increasing contact pressure is seen for these materials under these conditions as was expected. As these tests were undertaken whilst the rig was fully submerged in a full silicone oil bath, the adhesion contribution to the friction was expected to be quite limited. Silicone oil is expected to not only lubricate the interface but also fill in any gaps in the micro-roughness of the surface [51]. Eventually, the rubber can no longer deform any more or interact more closely with the contact surface. Above this applied pressure the friction coefficient remains at a constant value. Given the extremely low values for the coefficient of friction, and the similarity with elastomers of the same type, the adhesional effect has almost completely disappeared at this point and these friction contributions come from viscous hydrodynamic losses and hysteretic effects. In Fig. 5.6 this value was achieved at pressurisation of 24 MPa, but this value was seen to be very dependent on the type of lubricant, the surface roughness and the elastomer properties, with the elastomer and lubricant properties being subject to significant temperature dependency. Another aspect that could be determined from these test results was the pressure above which there was extrusion of the seal into the extrusion gap. This was significantly dependent upon the seal material properties and the test temperature. Extrusion of the seal was characterised by erratic sliding frictional force readings and an observable increase in the CoF with pressure. Fig. 5.6 highlights data where this was observed using the shaded rectangle. The zone of extrusion for each material was dependent upon the specific set of test conditions used. For the results presented here, the values of CoF are ignored when there is suspected extrusion in the test data.

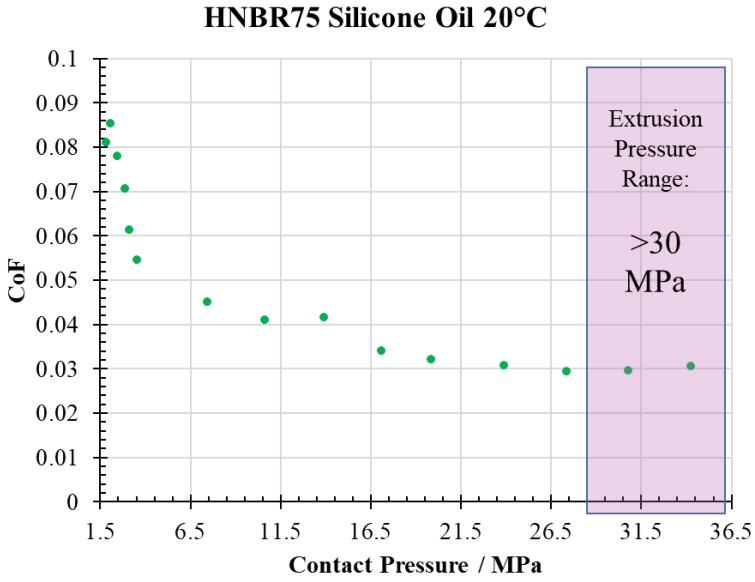

Fig. 5.6: A full test of an O-ring being pressurised until extrusion. The value of the coefficient of friction is observed to increase above the extrusion pressure.

When observed from the perspective of pressure, gland size also plays a role. The smaller gland sizes (larger compression levels) operate at slightly displace position on the plots when compared with data from the smaller glands. Figure 5.7 shows both gland sizes in a single graph, generating a continuous result for both sizes, despite the differences in contact area (shown in tables 4.2 and 4.3). This is in part because of the lubricating effect of the oil. To further understand this effect, different viscosity lubricants could be used. Given the number of tests necessary for this change, there was not enough time to test thicker, oil-based muds used in the industry. The study of velocity, pressure and temperature are still observable even within the same lubricant frame of reference.

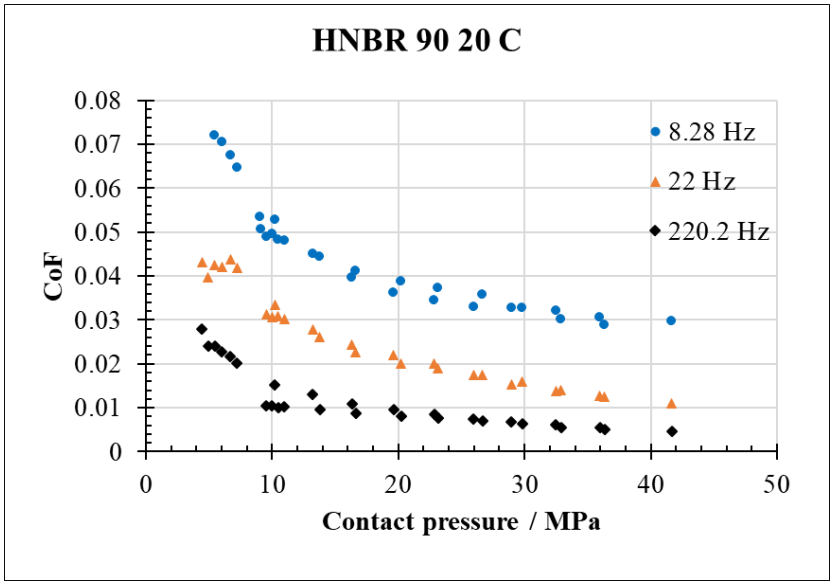

Fig. 5.7: CoF vs Contact pressure with frequency as the main differentiation. This approach can collapse different velocities to a simple relationship so long as the surface roughness is broadly similar and hence their sliding frequencies match.

5.3 The Effect of Temperature

The anticipated changes of mechanical behaviour with temperatures are discussed in the context of the viscoelastic behaviour of these types of elastomers in Chapter 2 from a theoretical point of view. Chapter 3 highlights these changes in viscoelastic behaviour as determined by experimental tests on samples of all four elastomer materials. Changes in the coefficient of friction due to temperature are not obvious since there are competing effects at hand. For example, when there is an increase in testing temperature there might arise:

- A softening of the elastomer material potentially increasing the contact area at a higher temperature.
- A change in the viscoelastic behaviour with temperature, strain and loading frequency, with a resulting change to the energy dissipation mechanisms during sliding the could either increase of reduce the observed friction.
- A reduction of the viscosity of the lubricant which might make it easier to be displace from the sliding interface and which will increase the observed friction.

As the rubber is in a slot or gland with a specific size and shape there is a limit as to the global strain that the O-ring can experience and so in effect the viscoelastic softening of these types of filled rubber with increasing strain, known as the Payne effect (explained in 2.5.3), is limited. Fig. 5.8 shows the typical behaviour with temperature using the FKM 75 material. The softening of the rubber with an increase in the deformability, translates into an increase in the contact area [52], together with an observed thinning of the lubricant. These two effects together are believed to be the cause of the observed increase in the friction coefficient as the temperature increased.

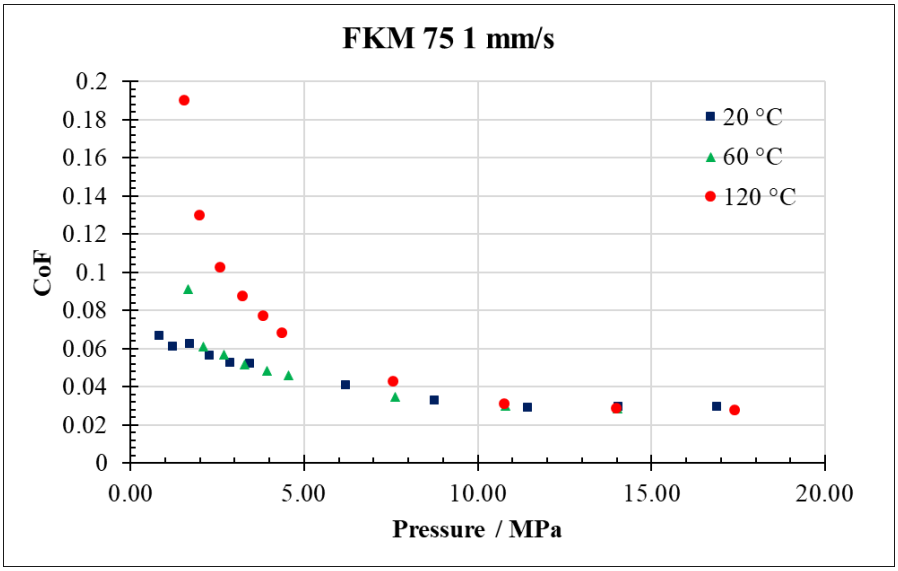

Fig. 5.8: The CoF vs contact pressure for an FKM seal at three different testing temperatures. The CoF value is increasing with increasing temperature before it reaches a plateau at the highest pressures.

5.4 The Effect of Velocity and Surface Roughness

When discussing the behaviour of dynamic seals, the sliding velocity at the interface becomes very important. Clearly this will not be the case for static seals. In this study, the velocity changes are associated with the surface topography of the sliding interface and the cyclic nature of the seal's interaction with the surface. Fig. 5.9 shows the changes in CoF with increasing velocity, the unit of mm/s being readily understood, so the data is presented this way here to aid understanding and to facilitate visualisation. For the HNBR 90 material shown here, there is a clear decrease in the CoF with an increase in the sliding velocity which is observed across the entire range of test pressures. This change is caused by an increase in the stiffness of the elastomer expressed both in terms of the in-phase storage modulus and the out of phase loss modulus with sliding velocity as this velocity corresponds to an increase in the strain rate [53]. This increase reduces the ability of the rubber to flow into the detailed contours of sliding steel interface at higher speeds. At even higher velocities (at above 1 m/s for example) there would be an additional contribution to the friction arising from the onset of the wear of the rubber surface [41]. For this specific set of test conditions, this range of required sliding velocities was never reached in this work.

The main drawback of using a sliding velocity in these graphs of friction behaviour is that it cannot be immediately related to the elastomer properties, at least not directly. A comparison between of the sliding velocity dependence of the friction coefficient in Fig. 5.9 between the two surfaces highlights that the coefficient is about twice as high for Piston B compared to Piston A across the entire range of pressures using the 1 mm/s sliding velocity for example when tested on HNBR 90. It is worth remembering that from simple observations, that these two surfaces at the length scale that we can resolve with our eye or feel with our fingers appear identical. So, if we were to use a velocity map for the friction coefficient, it would require a different curve to be produced for every sliding interface that was to be encountered.

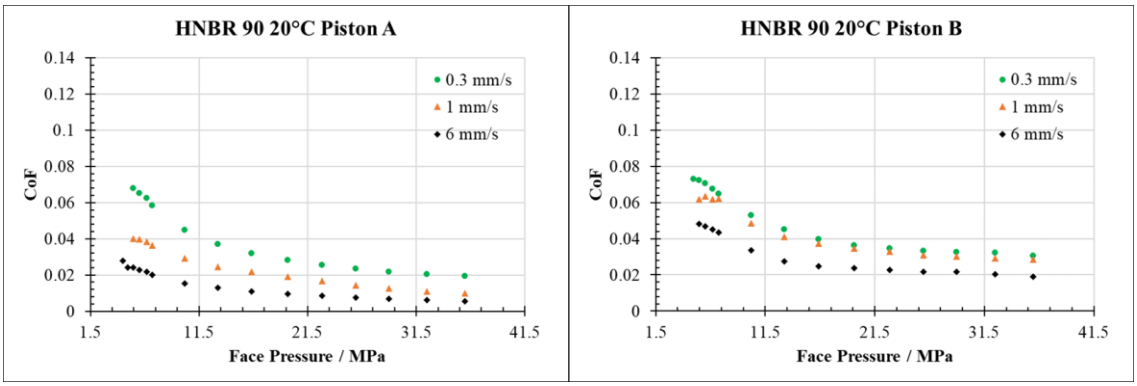

Fig.5.9: CoF vs. Contact pressure for two different sliding surfaces. By using velocity as a variable, it would require a different diagrams to determine how the friction varied for each specific surface roughness.

Therefore, an alternative approach is required. The standard approach adopted in practice is to associate the velocity of movement to a characteristic length measured on the sliding surface. This approach allows an association to be made between the sliding velocity with a sliding frequency that can be related directly to the measured viscoelastic properties of the rubber. Knowing that rubber properties change with changing frequency of deformation, we can derive frequency-dependent friction results [35]. These results are much more translatable between different surfaces, as is highlighted in Fig. 5.10.

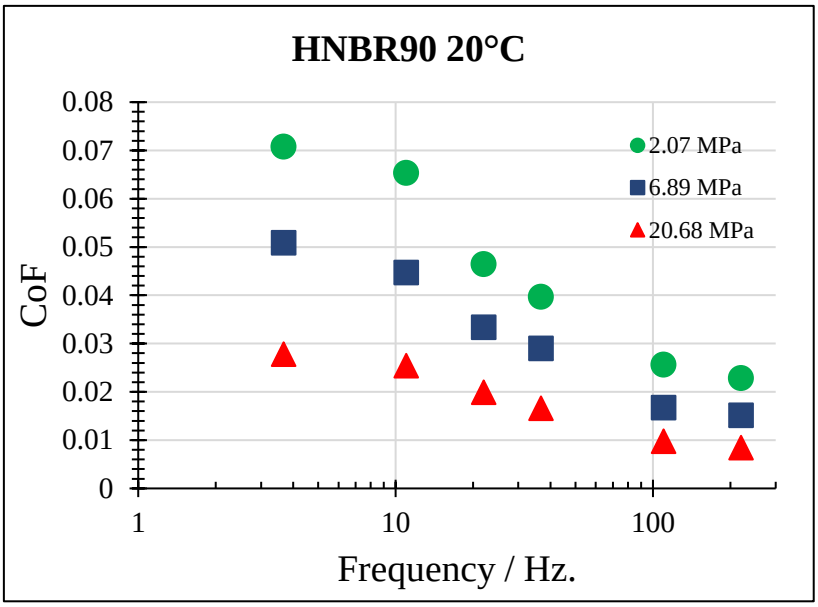

Figure 5.10: CoF vs Frequency of deformation for two different sliding surfaces. Results can be collapsed into the same graph thanks to the characteristic length. The effect of pressure can still be clearly observed.

Some changes to the rubber CoF can occur even at the same frequencies if the surface material is different, mostly because of additional contributions to the friction from the adhesional term. For the case of lubricated friction and similar surface materials (as is the case for all the work presented here), frequency-related results are the best way to observe how the strain-dependent properties of rubber affect the CoF.

5.5 Detailed Results and Material Models

Having explored how the rubber sealing materials are affected by each of the different experimental variables, both from the background literature and from our initial experimental investigations, it is important to develop a way to represent all the measured results for all four rubber seals across all three different temperatures. Figs. 5.11 and 5.12 show how the hardness, temperature and frequency each alter the rubber friction for both HNBR and FKM rubber seals. This pressure dependent behaviour reflects the anticipated behaviour reported in the scientific literature [55]. The compiled results presented in figures 5.11 and 5.12 facilitate an easy comparison of how the key variables of temperature, pressure, modulus of the rubber and sliding velocity impact the frictional behaviour for the HNBR and FKM compounds respectively.

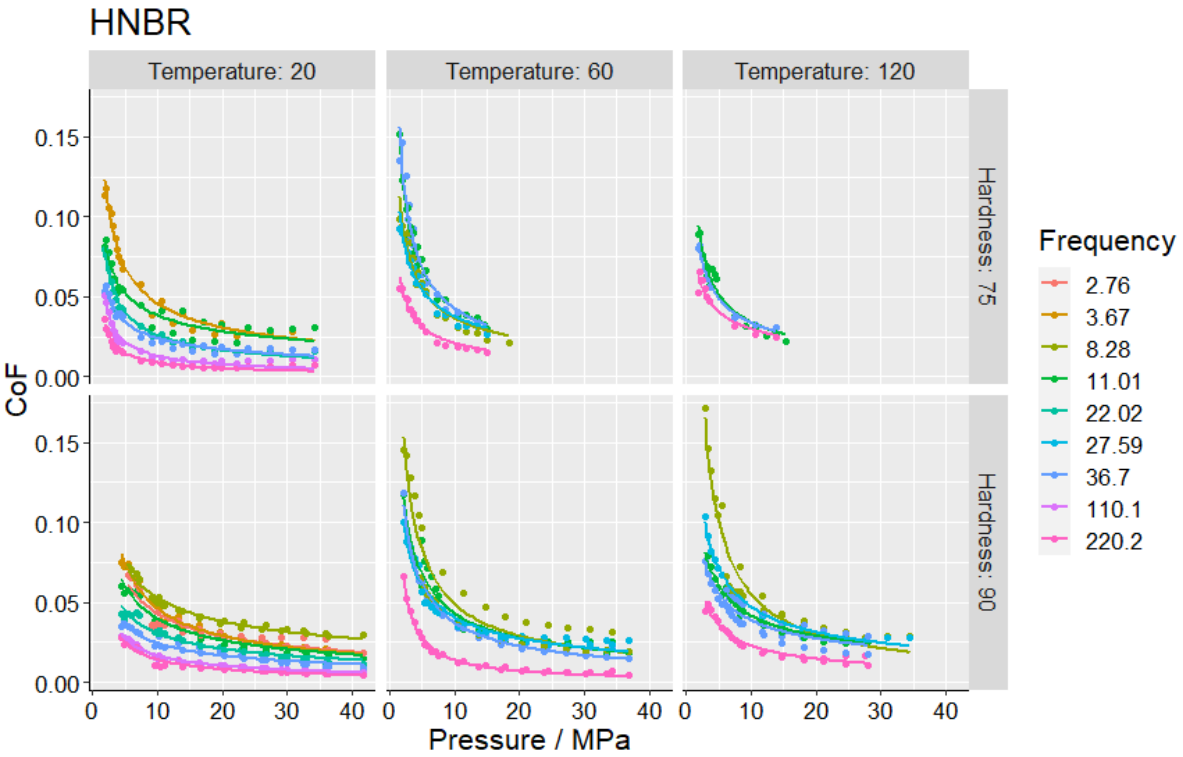

Fig. 5.11: Frictional analysis of HNBR against contact pressure for different temperatures and Shore A hardness. Series shown by frequencies in Hz.

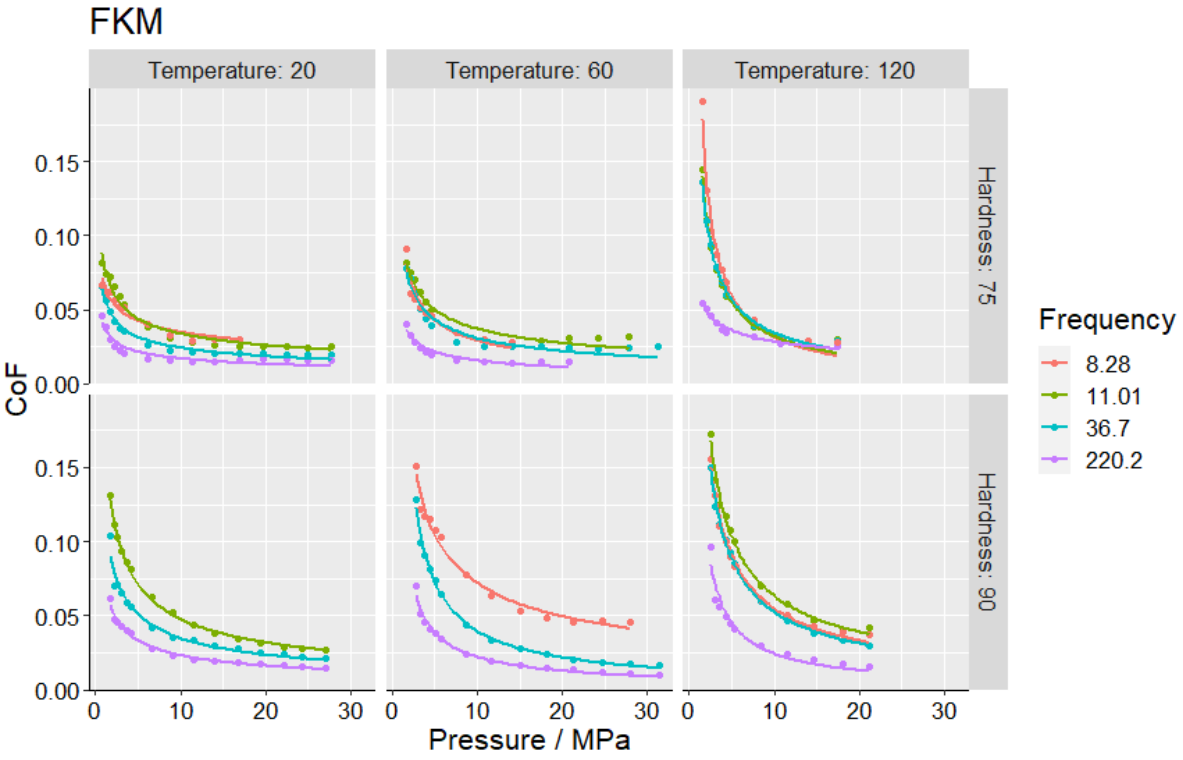

Fig. 5.12: Frictional analysis of FKM against contact pressure for different temperatures and Shore A hardness. Series shown by frequencies in Hz.

Temperature effects: There are several different factors in the friction behaviour that are altered by an increase in the temperature. These include the viscosity of the lubricant, the modulus of the rubber, and the toughness of the rubber all of which are reduced with increasing temperature.

The reduction in the viscosity of the lubricant results from an increase in the kinetic energy of the molecules that make up the lubricant. With an increase in temperature, the particle interactions decrease, reducing the internal friction which produces a resulting drop in viscosity. This is typically described in the industry as the "thinning out" of the lubricant. Because of the reduction in the lubricant viscosity, the localised pressure from the rubber pressing against the surface is now at the point where it may be enough to totally displace the lubricating layer. With a reduction of the lubricating layer, the real interfacial contact area is likely to increase at all levels of pressure. It is clear from the higher (120°C) temperature tests, that the reduction of the CoF with pressure is more significant as the pressure starts to increase. Not only that, the CoF across most of the test frequency range is increased at higher temperatures.

Changes of rubber modulus with temperature are contributed to by various effects. Figure 3.4 shows that higher temperatures correlate with lower storage modulus for the rubber materials at all frequency points. When looking at equation 2.5.7, the NkT term (where T is the absolute temperature) highlights how for an unfilled elastomer that the shear modulus of rubbers is directly proportional to temperature. Thus, the softening of the rubber with increasing temperature appears counterintuitive. However, although the rubber matrix of the compound is stiffened with an increase in the temperature, the filler network structure and the polymer filler interactions are both reduced with an increase in temperature [76]. The filler network breakdown and the polymer chain stiffening are competing factors in determining changes to the mechanical behaviour of rubber with temperature. The HNBR75 uniaxial tension results presented in Figure 3.1 are an example where these two competing effects cancelling each other out and the stress versus strain data are virtually identical at all three temperatures. When rubbers are even more highly filled, which is common for the case of oilfield elastomer seals, then a very significant of the elastomer compound stiffness comes from the filler network. Consequently, once the interactions of the network weaken, the rubber will lose some of its stiffness. This is the case for example with HNBR90 where the elastomer compound is clearly less stiff at higher temperatures. If the rubber becomes too soft, then seal extrusion is more likely, which contributes to the failure of some of the seals at 120°C at lower levels of pressure.

The secondary effect of rubber reduction in modulus with temperature is that the real contact area increases at lower levels of pressure. The increase in the real contact area will produce an increase in friction at lower pressures, the effect of which will reduce as the pressure increases. These effects all contribute to the steep decrease of CoF with pressure at elevated temperatures and the failure of the seal at higher levels of pressure.

There is a tertiary effect of temperature that can be related to the cohesive failure of the rubber. Equation 27 includes a fourth contribution to the friction force that is related to the

elastomer wear, typically referred to as the friction contribution associated with cohesive failure. As explained in chapter 2, the cohesion contribution comes from the additional irreversible energy dissipation that is used to generate cracks in the material as it is being abraded away by the action of the surface roughness pressing against the elastomer. At the higher temperatures, the local deformation of the elastomer is greater, and the abrasion resistance of the elastomer is reduced, causing some small, localised failures to generate shavings of O-ring into the pressurised annulus. This extra energy dissipation that is associated with the crack growth adds a contributory effect onto the measured friction. It also implied that abrasion failures occur more easily and that the overall pressure limits are lower when this type of behaviour occurs during friction testing.

Even when these effects are described, one can still observe that at the highest pressure levels, the values for CoF are similar between different temperatures. At this point, the material's inherent mechanical properties that are being changed from higher temperature are not as important as the fluid's hydrodynamic losses. Given that the lubricant is the same for all materials, these equal values are likely the lubricant behaviour at this level of pressure.

Pressure effects: The effect of pressure has both a mathematical and a physical significance to the understanding of the coefficient of friction. The mathematical effect is relatively simple, and produces a CoF versus pressure curve that has an exponential decay shape. Although the adhesive component is increased with pressure due to an increase in the contact area, the relationship between normal pressure and adhesion is highly nonlinear.

The physical significance of pressure effect on friction arises from two contributions to the pressurisation. The first results from the initial response of the rubber to conform to the shape of the gland and then there is an additional deformation resulting from the fluid injection. The initial pressurisation is fixed provided that the seal and gland socket geometry both remain unaltered. In practice during our testing, we had different gland size geometries. These were observed to generate only modest differences in the strain-induced responses. The additional gland sizes only shifted the initial state of the test range slightly and therefore provided additional points on the graph with increasing fluid pressure.

When it comes to fluid pressure, the effects were much more significant at the lower pressures. To illustrate this the HNBR90 O-ring simulation at 13% compression are used as an example. Table 4.5 shows the initial contact area at 772 mm^2 without any fluid pressure, simply contact between the piston and the seal, after an increase to maximum pressure (35MPa) this contact area increases by 62%. The contact pressure however, increases from 4.46 MPa to 35.96 MPa, a 700% increase. Since contact area is linearly related to adhesional friction, even assuming a very non-realistic consistent growth of contact area under lubricated conditions, it is clear that the adhesional effect is almost non-

existent, and the total friction contributions come from the hysteretic effect as the pressure increases. This can be explained with two arguments: The maximum contact area to be reached is limited, given that the O-ring is contained within a gland; the low values of CoF are not in the range of what adhesional effects would cause[87], more within the range of hysteretic effects in smooth surfaces and hydrodynamic losses[98].

Modulus of the rubber: The modulus of the rubber is determined by various elements and has various consequences in sealing and rubber friction. When it comes to hardness, a higher hardness is associated with higher modulus [89], since the hardness test is simply an observation of the resistance for a small elastic deformation on the surface of the rubber. Initially, before any fluid pressure is applied, the initial pressure level is higher for the same amount of deformation. Meaning there is a small section at the lower levels of pressure where there is no data for higher hardness values. This initial pressure difference becomes almost irrelevant at higher levels of fluid pressure, as it is shown in tables 4.3 and 4.5. Another aspect to consider is the resistance to extrusion. If the rubber has a higher modulus, then extrusion will occur at higher fluid pressures, allowing for more data points. For most velocities, the lower hardness elastomers fail at lower levels of pressure, especially at higher temperatures. The modulus of the rubber then is observed from a compound standpoint.

For commercial materials whose composition is not completely known, one typically assumes that an increase in filler materials is the cause for the higher modulus. At larger amounts of filler, the hysteretic losses increase. When comparing the friction trends for the same elastomer, we observe that the higher hardness does have higher CoF at the higher velocities and pressure levels. This could be attributed at the increased hysteretic effect at higher pressure levels, where the adhesional factor becomes less influential in the overall CoF.

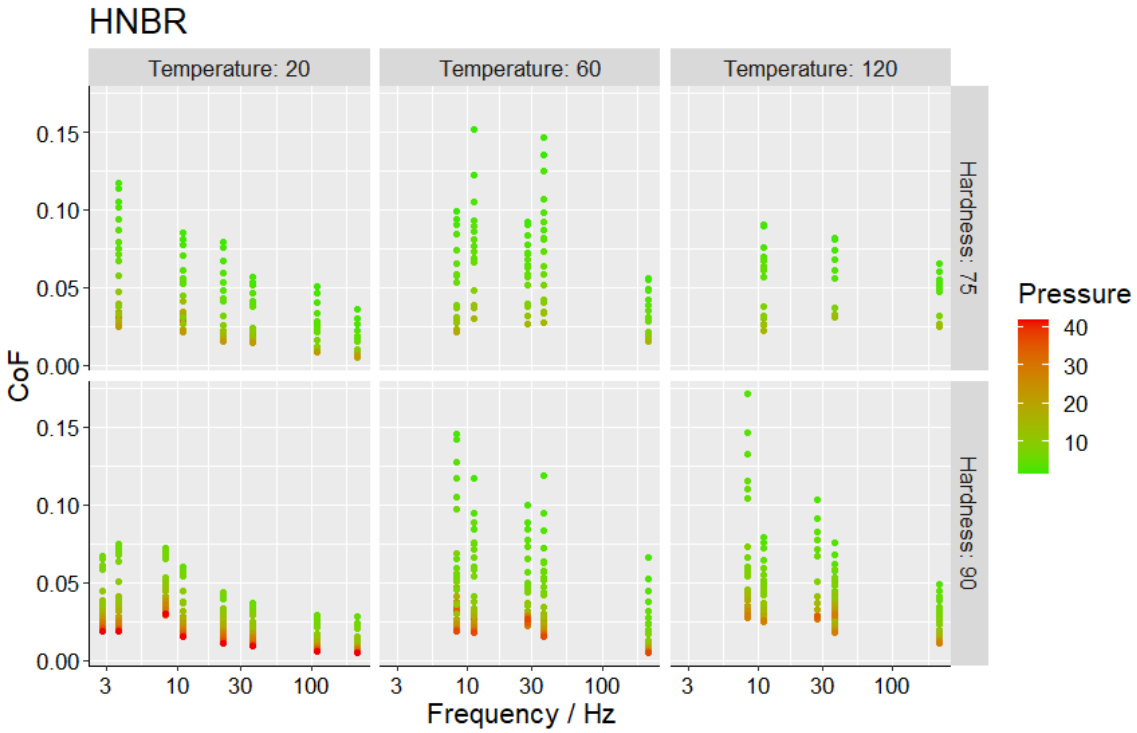

Figure 5.13: Frictional analysis of HNBR against frequency (converted from velocity and surface roughness) for different temperatures and Shore A hardness. Series shown by pressure levels on a colour scale.

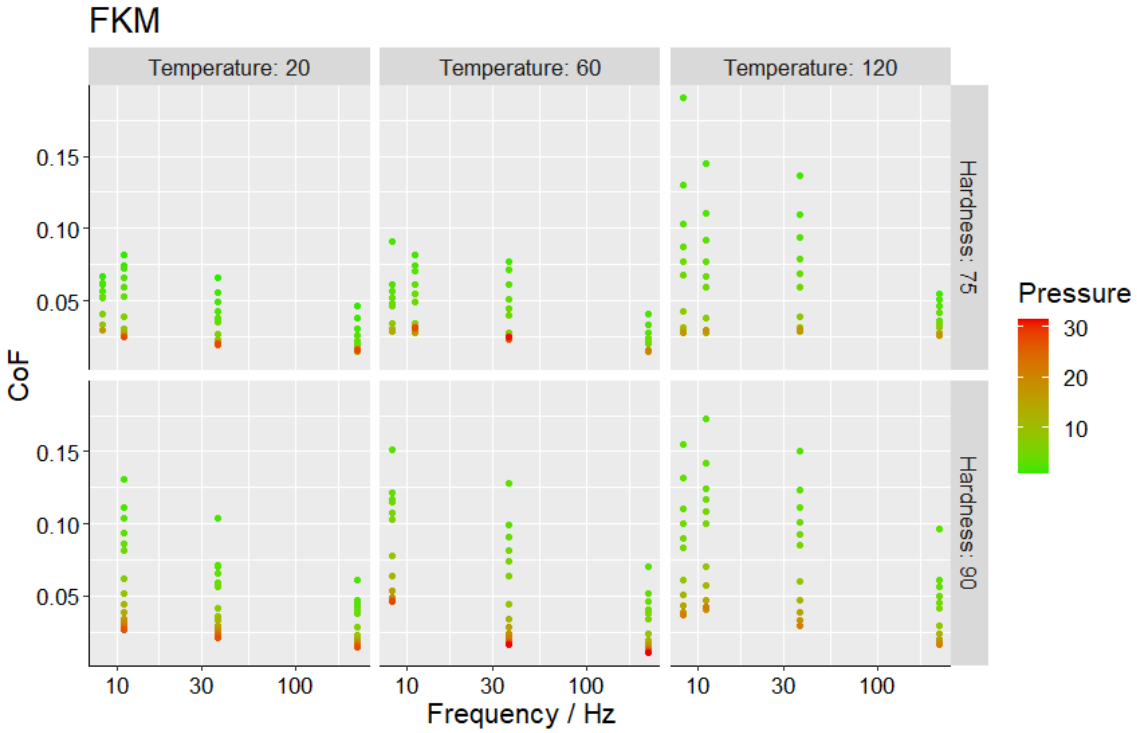

Figure 5.14: Frictional analysis of FKM against frequency (converted from velocity and surface roughness) for different temperatures and Shore A hardness. Series shown by pressure levels on a colour scale.

Velocity effects: as the frequency increases, there are viscoelastic changes in the rubber. Since the localised deformation occurs at very fast rates, the strain dependent component of the rubber modulus is affected. Figures 5.13 and 5.14 demonstrate the changes in friction expressed in terms of the frequency of deformation. The dynamic

mechanical analysis (DMA) results in chapter 3 (for HNBR75) highlights how the viscous losses are dependent on loading frequency. For these results, the highest values of CoF do not fall under these maximum tan δ ranges. This indicates that the change in frictional behaviour does not come simply from the hysteretic losses. Maximum CoF values fall around the 1 to 10 Hz mark, this is correlated in the literature with the adhesive component peak [41].

The ranges typically seen for maximum tan δ contribution to friction are close to 1-10m/s [54][40][35], this is very uncommon for the oilfield seal industry, even in dynamic seals. The automobile industry has components that can actually reach these sliding velocities. For example, the tyre friction encountered on the road is modelled around the viscous losses maximum in order to determine safe wet grip conditions. Metal seals in engine pistons can reach speeds greater than 10 m/s, but retractile seals and oilfield O-rings move at much lower speeds.

The difficulty of analysing the adhesional component is not an uncommon one. Tiwari's research from 2018 [41] uses experimental data from total friction values and then assumes the remainder of this force to be entirely arises from the shear forces caused by adhesional behaviour. Equation 52 shows how using the viscoelastic contribution from the Persson model, the shear forces $\tau_f(v)$ from the adhesional contribution are simply the difference between the experimentally obtained total friction, and the modelled hysteretic contribution at that particular velocity. This assumption shows that there is no expectation of wear contribution at this velocity. The research also assumes that the effects of cohesion (called shearing transfer film in the publication) occurs only at the highest of velocities, as shown in figure 5.15.

$$\tau_f(v) = p_0\left(\frac{A_0}{A}\right)(\mu(v) - \mu_{visc}(v)) \tag{52}$$

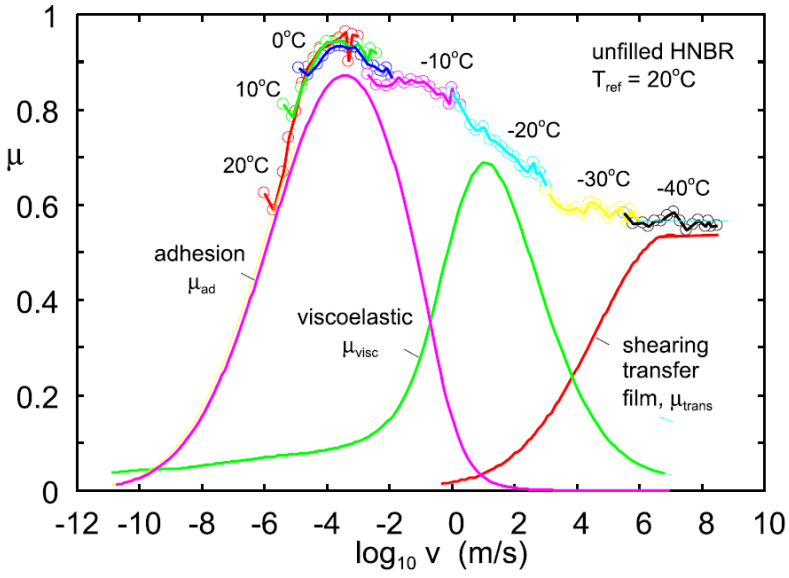

Figure 5.15: Master curve of friction coefficient data for a HNBR compound. Taken from [41]

Both Persson and Kluppel theories use some form of friction experimental data to determine the frictional model. Using Thirion's theory from eq. 29 we can obtain a simplified version of frictional models for our dataset using coefficients C_A and b. The necessary constants that are required to fit the data are presented in Tables 5.2-5.5.

Table 5.2: HNBR 75 mathematical fit for equation 50

HNBR 75			
Temp (°C)	Freq	Ca	B
20	3.67	0.167	-0.5255
	11.01	0.1035	-0.383
	22.02	0.114	-0.6171
	36.7	0.0741	-0.4694
	110.1	0.05212	-0.7711
	220.2	0.05212	-0.7711
60	8.28	0.1349	-0.5842
	11.01	0.1993	-0.7125
	27.59	0.1241	-0.5242
	36.7	0.1993	-0.6138
	220.2	0.07585	-0.5527
120	11.01	0.1349	-0.6426
	36.7	0.1163	-0.5396
	220.2	0.08238	-0.4433

Table 5.3: HNBR 90 mathematical fit for equation 50

HNBR 90			
Temp (°C)	Freq	Ca	B
20	2.76	0.1739	-0.5614
	3.67	0.2079	-0.6285
	8.28	0.1727	-0.5053
	11.01	0.1432	-0.537
	22.02	0.1046	-0.5294
	36.7	0.08371	-0.5183
	110.1	0.08535	-0.6961
	220.2	0.0825	-0.7285
60	8.28	0.2499	-0.6016
	11.01	0.1859	-0.6658
	27.59	0.1634	-0.5885
	36.7	0.1919	-0.6979
	220.2	0.1392	-0.9748
120	8.28	0.3829	-0.7927
	11.01	0.1367	-0.5148
	27.59	0.1847	-0.5931
	36.7	0.1279	-0.5418
	220.2	0.09191	-0.5873

Table 5.4: FKM 75 mathematical fit for equation 50

FKM 75			
Temp (°C)	Freq	Ca	B
20	8.28	0.06733	-0.2872
	11.01	0.08167	-0.3844
	36.7	0.05961	-0.3916
	220.2	0.03855	-0.3565
60	8.28	0.107	-0.5679
	11.01	0.1019	-0.4394
	36.7	0.0961	-0.4948
	220.2	0.04628	-0.4756
120	8.28	0.267	-0.9305
	11.01	0.197	-0.7915
	36.7	0.1846	-0.7317
	220.2	0.06162	-0.3433

Table 5.5: FKM 90 mathematical fit for equation 50

FKM 90			
Temp (°C)	Freq (Hz)	Ca	B
20	11.01	0.1818	-0.5825
	36.7	0.1259	-0.5609
	220.2	0.07744	-0.5246
60	8.28	0.2502	-0.5415
	36.7	0.2964	-0.8749
	220.2	0.144	-0.8147
120	8.28	0.319	-0.7583
	11.01	0.3464	-0.7307
	36.7	0.3217	-0.7809
	220.2	0.2124	-0.9332

Currently, most rubber friction models require some form of rubber friction testing; they are not comprised of independently measured physical parameters alone. In order to observe the effects of frictional models, chapter 6 has different models of rubber friction applied to finite element analysis modelling. Once the effects of industry standard models are compared to experimentally tested data, we can observe the importance of using an appropriate characterisation of elastomer frictional behaviour in practice.

Even though the theories of Persson (Eq. 37) and Klüppel (Eq. 41) have not yet been tested at extreme pressures and temperatures, there is always an interest to review how well these models would fit, with both individuals being leading researchers in the field. To use the best-case scenario, both theories were tested at the lowest pressure levels from

experiments (2.07 MPa) and temperature (20°C). Figures 5.16 and 5.17 show the output of both theories, although their peak region for adhesional friction is in the "correct" range (between 10 and 100 Hz.) when compared to figure 5.13, their values are simply too high. The values of $P(q)$ from Persson's theory, would assume a constant growth of the surface contact area with pressure. In a road-tyre interface this could be the case, but with smooth, lubricated surfaces, there is a limit to the maximum contact area one could reach. Given that silicone oil is not compressible, an increase in pressure will only affect the area of contact so much. The Persson $P(q)$ is also used as the contact area variable for Klüppel's theory, causing the same issue of overestimating the adhesional contribution. There is also the question of taking experimental values from literature, but there simply was not the opportunity (either time or resources) to obtain the values for the HNBR 75 rubber. Therefore, Thirion's method is still preferred provided that the testing equipment is available.

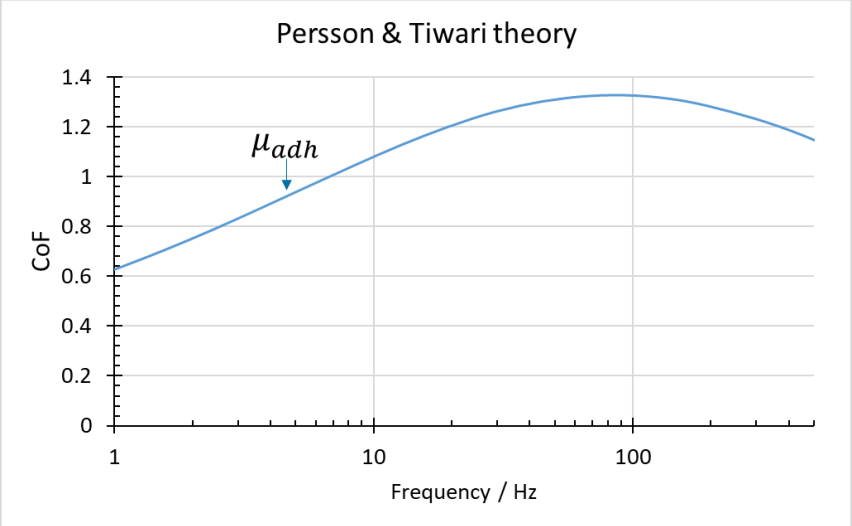

Figure 5.16: 2.07 MPa and 20°C model result for HNBR 75 using Persson's theory of adhesional friction.

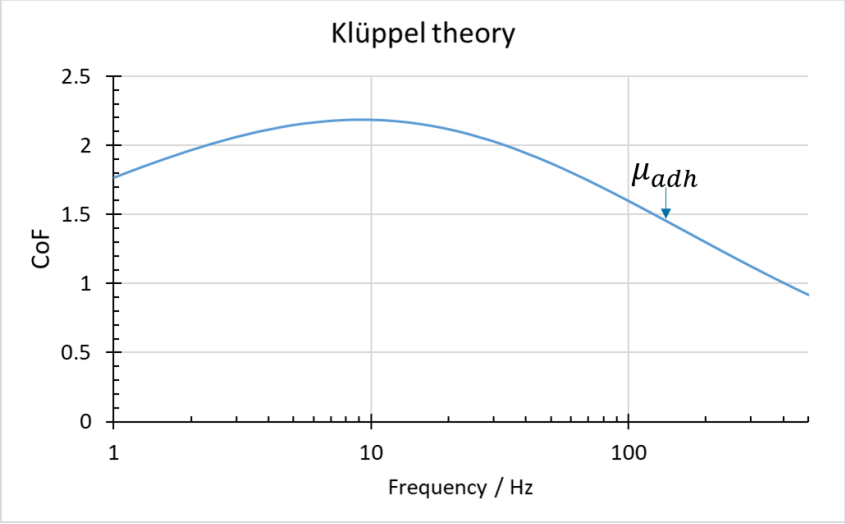

Figure 5.17: 2.07 MPa and 20°C model result for HNBR 75 using Klüppel's theory of adhesional friction.

For Persson's theory, $r(0)$ = 1 x 10^9 m, $\Delta\gamma$ = 0.1 J.m^2 [40] and for Klüppel, V_c= 0.1 cm/s, $\tau_{s,0}$ = 0.65 MPa [39]. For the hysteretic values, only Persson was used because of the problems with Greenwood & Williamson theory, the PSD approach was then used for both contact areas. The γ factor in the $S(q)$ was still used as 0.5 (as per their recommendation). Figure 5.18 shows the hysteretic contribution according to Persson's theory.

Although the results are within the range of values that match our experimental outputs, the total contribution from both $\mu_{adh} + \mu_{hyst}$ goes above the test results. Most experiments from Persson and Klüppel assume little to no adhesional contribution when lubricated. This was also the case in our experiments. Only at the highest of temperatures, with the thinning of the lubricant could we observe some form of increase in friction. In research prior to this, most authors would simply subtract the hysteretic component from the total friction and obtain the adhesional value. In this case, the contribution from the hysteresis model still needs a bit more to reach the frictional values obtained in experiments. It was in the interest of the researcher (and the sponsor) to try and derive this value using purely physical properties of the rubber. Even so, it would be best for cases of lubricated friction against very smooth surfaces, to focus on hydrodynamic losses, more so than adhesional friction.

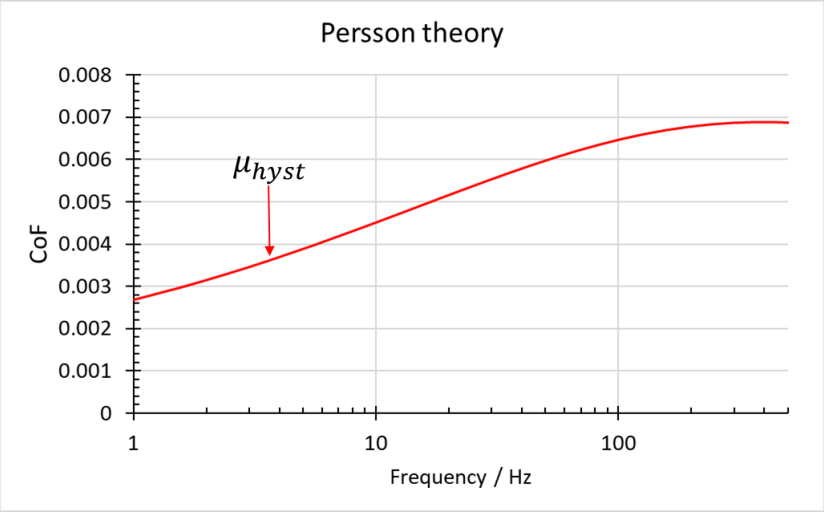

Figure 5.18: 2.07 MPa and 20°C model result for HNBR 75 using Persson's theory of hysteretic friction

The low values of friction can be mostly attributed to good lubrication. When it comes to seal setting and dynamic seals, low coefficient of friction values are desirable. Improved durability of seals and energy efficiency during movement are of paramount importance in engineering. Although for very high temperatures and pressures, liquid lubricants tend to be replaced by solid ones[98] it appears that for the combination of steel and rubber, a liquid lubricant seems to be enough to maintain low friction coefficients. Not only because it cleaves the contact of the polymer chains to the substrate, but because it modifies the substrate itself. Once lubricant comes into contact with a rough surface, the main roughness

scales are still present, but the micro-roughness levels can disappear [101]. This is the lubricant filling out the small gaps on the micro-roughness level.

Research of lubricating conditions for soft materials is of great interest, not only for sealing industry, but for biomaterials as well. The rheological effects of the polymer also come into play when it comes to film thickness and dry contact area. Even then, since the localised deformations change with fluid filling of the surface roughness, the lubricant itself will affect the viscous losses of the rubber, complicating the calculation of hysteretic losses.

These results were initially not focused on the lubricant itself, but from the results, it is clear that follow up studies looking at the effects of different lubricants with varying viscosities would complement the current conditions. [101][101]

FEA modelling has become a staple in the industry, with much attention focused on the strain energy density behaviour of the elastomers. To better observe how relevant frictional behaviour is for seals, chapter 6 deals with various examples using industry standard values compared to models that use these experimentally determined values for the HNBR and FKM materials.

6. Validation of Friction Models used in Engineering Design.

Finite element analysis modelling packages such as Abaqus that can be used to model the interaction between different parts of an engineering system, require an interactional behaviour description between the surfaces of the modelled bodies. Often simple limiting conditions are adopted in the industry such as modelling the tangential behaviour assuming either a frictionless condition or by adopting a fixed penalty condition. From the data presented in this thesis, these types of simplification are now known to be wrong. Even with significant lubrication, there can be no frictionless interaction with these types of highly filled elastomer sealing materials due to their viscoelastic losses. A fixed penalty is unrealistic, as was shown from the high pressure / high temperature testing data presented in Chapters 2 and 5. It is apparent that an oversimplification of frictional behaviour significantly limits the accuracy of any model predicting the frictional forces during seal setting or sliding motion for example. There are also other implications to using unrealistic frictional behaviour in the model. Not only are the resulting stresses resulting from this misrepresentation of the tangential behaviour wrong, but also there is a cross over impact on the normal stresses at the interface being wrong which then makes the generated stress contour maps inaccurate. This would suggest that models such as those that are attempting to predict failure or the onset of a leak path, which are particularly susceptible to large changes in outcomes dependent upon relatively small changes in the predictive stresses, are all likely to be subject to large errors.

Typically, fixed coefficient of frictions or models that are linearly changing the behaviour are adopted in the industry [90][56]. This chapter examines the consequences of this common mistake. The effect changing the coefficient of friction (CoF) models is presented on the different outputs that are calculated using FEA models of in-service sealing applications. The model adopted for this investigation examined the normal contact pressure of a deformable rubber seal in contact with a rigid surface contrasting the outputs of a pressure-dependent CoF with models that have simplified fixed CoF interactions.

6.1 The Different Models

Using the same dimensions from the rig dimensions and a HNBR75 material model (a very common O-ring used in oilfield seals) Fig. 6.1 shows a diagram with a schematic of the different friction models that were tested. The pressure dependent coefficient of friction tapers off at a value close to 0.13. This model is contrasted with a model that uses a fixed coefficient of friction that has the final value of 0.13. Also tested were models that use fixed CoFs of 0.2 and 0.3, since both of these are widely adopted currently in the industry for simulations [4]

The same simulation outlined in Chapter 4 was used to obtain the normal force which

does not change significantly with changing coefficient of friction (Fig. 6.2). Three levels of fluid pressure were used to observe these changes: no fluid pressure injected, 1.38 MPa and 3.45 MPa injected. Although these are extremely low pressures for the oilfield industry, there are certain working tools that function within this range. There is also the importance of seal setting in non-pressurised and under hydrostatic pressure on surface safety valves. Without any fluid pressure injected, there is still a baseline contact pressure that arises from the mechanical response of simply compressing the O-ring as it is located into the gland. At the highest levels of pressure (>70MPa) the effect of the elastomer stress response to strain is irrelevant. The purpose of this section is to observe how different frictional behaviour can affect non-frictional outputs, since friction is inversely proportional to load, harder elastomers will reach the plateau region much faster. In order to observe low pressure regions (high disparity between fixed and pressure dependent models) and high pressure regions (plateau region of pressure dependent models), a soft elastomer was selected (HNBR75) and pressurised until well above the plateau region.

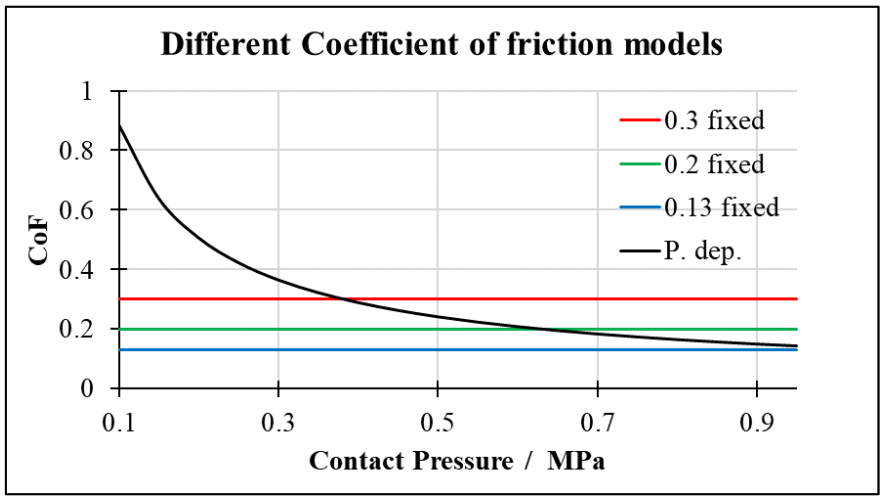

Fig. 6.1: Schematic diagram of the four coefficients of friction tested for the FEA models.

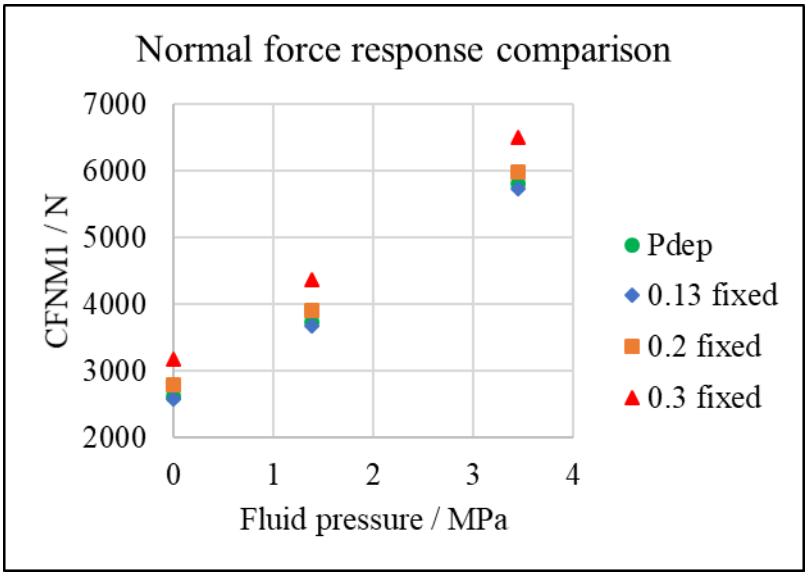

Fig. 6.2: The normal force output CFNM1 from the O-ring setting simulation. Three different coefficients of friction were each used to analyse the force response.

6.2 Contact Pressure Changes

Figure 6.3 shows the visualisation of the FEA simulation results for the O-ring setting and pressurisation steps. We can observe how the higher fixed coefficients of friction have much larger contact pressure (CPRESS in Abaqus output) responses. This change in pressure response is of great significance when trying to design effective seals.

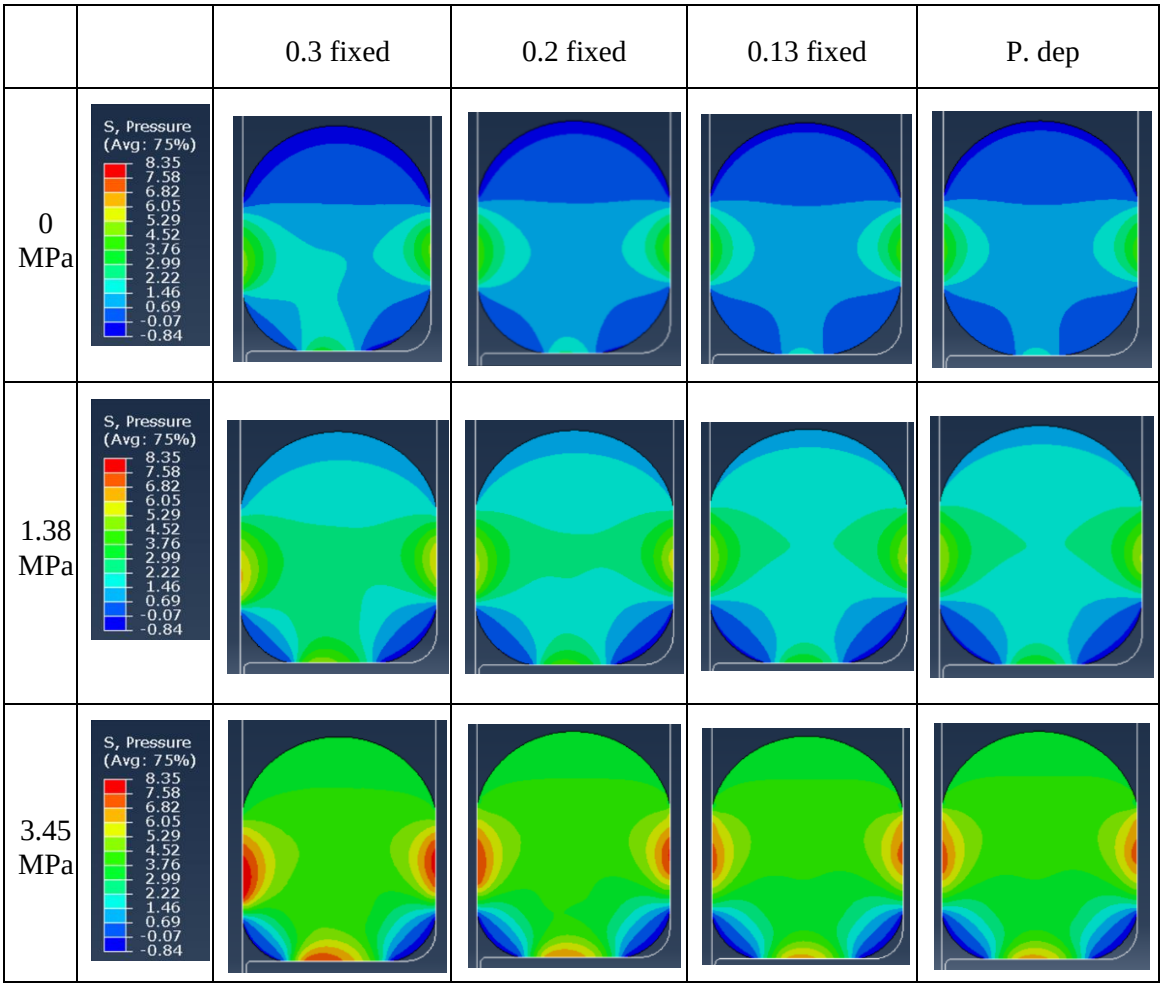

Figure 6.3: Comparison of contour maps of the contact pressure with different CoF models in a circular symmetric round O-ring seal. S, Pressure is the pressure in response to strain in the nodes, expressed in MPa, not to be confused with contact pressure (CPRESS) with is only present in the surface contact nodes.

Seals are intended to stop fluid exchange between regions by having a contact pressure that is above the pressure of the fluid. Observing figure 6.3 shows how an overestimation of friction could impact on the assumption of a properly working seal. In practice, both the average contact pressure, along with lower tangential forces, are factors that determine how well the seal functions.

A more precise look at the differences in contact pressure on the inner contact surface (to the left in each pot), is shown as the magnitude of the contact pressure against the length of contact. In Fig. 6.3, the 0.2 and 0.3 fixed coefficients of friction have a larger contact pressure all along the contact area. The difference in magnitude is proportionally smaller at the higher levels of fluid pressure, since the incompressibility of the rubber causes the

transmission of pressure to be less dependent on the detailed mechanical response. A comparison between the pressure dependent CoF model and the fixed 0.13 coefficient of friction, highlights that both outputs of contact pressure across the interface are similar. If the final high pressure plateau value of the pressure dependent coefficient of friction is known and is used for simplicity or to reduced computational effort, as a fixed CoF, there does not seem to be a large difference in the calculated contact pressure output.

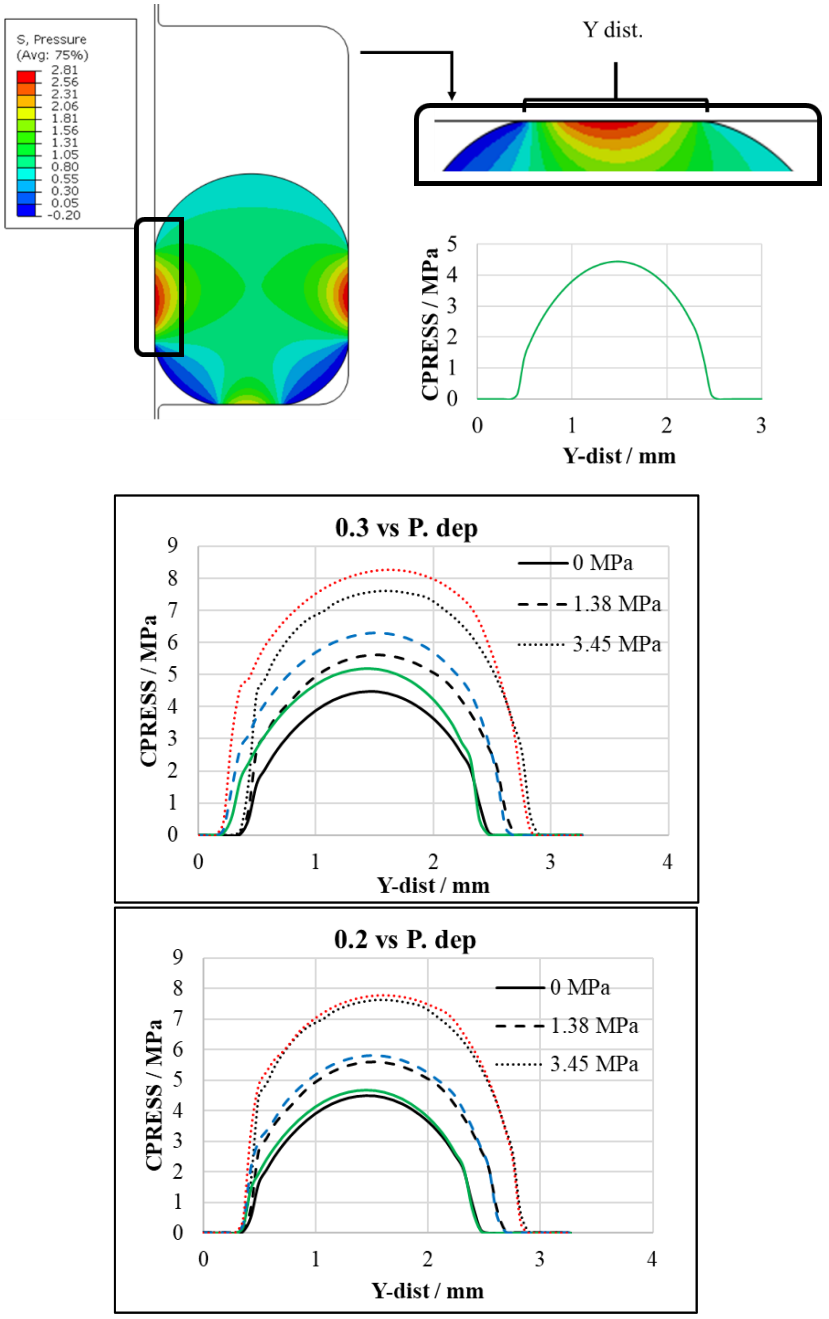

Fig. 6.4: Diagram of the area where Contact Pressure (CPRESS) output comes from in the FEA analysis (top), the length of contact changes with increasing pressure, as observed on all graphs. Comparison of contact pressure response for different coefficients of friction compared to experimentally determined ones. Fixed coefficients are presented in colour and pressure dependent ones in black.

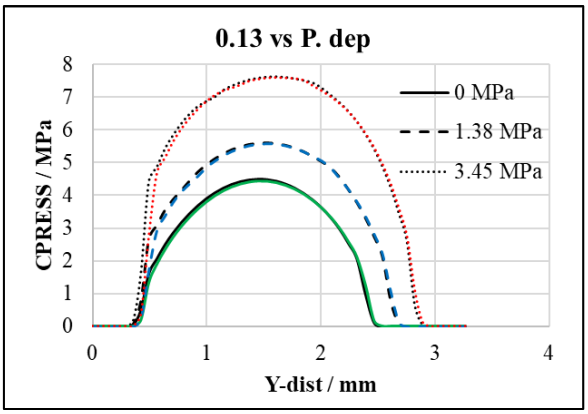

Fig. 6.4(cont): Diagram of the area where Contact Pressure (CPRESS) output comes from in the FEA analysis (top), the length of contact changes with increasing pressure, as observed on all graphs. Comparison of contact pressure response for different coefficients of friction compared to experimentally determined ones. Fixed coefficients are presented in colour and pressure dependent ones in black.

6.3 Strain Energy Density Changes

Strain energy density (SENER in Abaqus output) plots are often used to help identify crack initiation and crack growth criterion in sealing systems[57]. SENER is measured per unit volume in the nodes, to avoid outputting mesh size dependent values. After computing the stress values, an average of neighbouring integration nodes is the output for the element. When the relative difference between the node and its neighbouring elements is greater than a certain percentage value, the vales are not averaged. This averaging takes place before computing the scalar values for stress, so it does not change the simulation output, simply how the values are observed in the user interface. A 75% is the default value for Abaqus, which yields a smooth transition between nodes.

The local deformation of rubber seals is also of great importance in these failure prediction models. For these reasons the strain energy density plots were chosen as the second variable to examine the effect of varying the CoF model. Figure 6.5 shows strain energy density contours from FEA for the different CoF models. The strain energy calculated in the seal is more concentrated with a CoF of 0.3 that with the other friction models.

		0.3 fixed	0.2 fixed	0.13 fixed	P. dep.
0 MPa	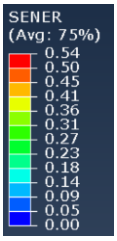	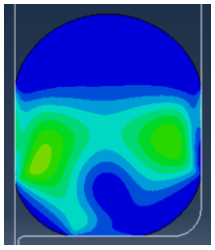	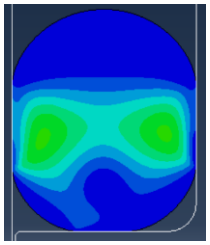	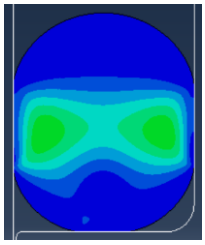	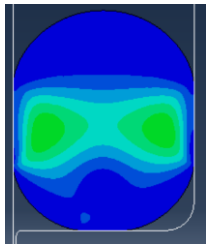
1.38 MPa	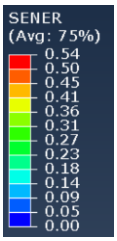	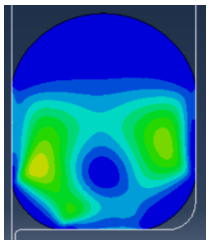	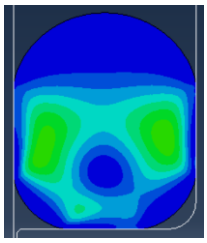	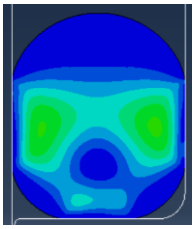	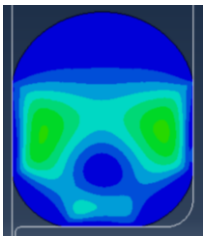
3.45 MPa	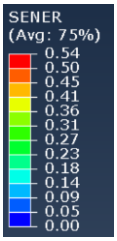	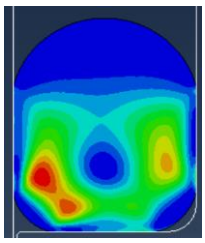	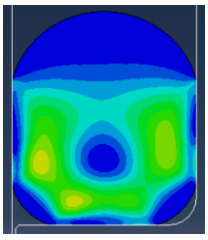	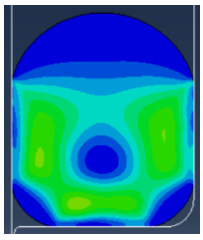	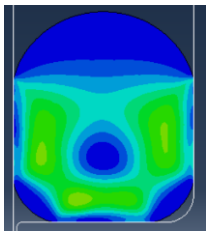

Fig. 6.5: Comparison of contour maps of the strain energy with different CoF models

To illustrate the effect of strain energy density, graphs of strain energy density were produced. These stresses were mapped onto the undeformed geometry of the O-ring cross section. This effect can be highlighted by plotting these contours across a straight line radiating from the centre of the O-ring that goes through the zone of maximum strain energy. This allows an easy comparison of the differences in these contour plots between models that used different CoFs.

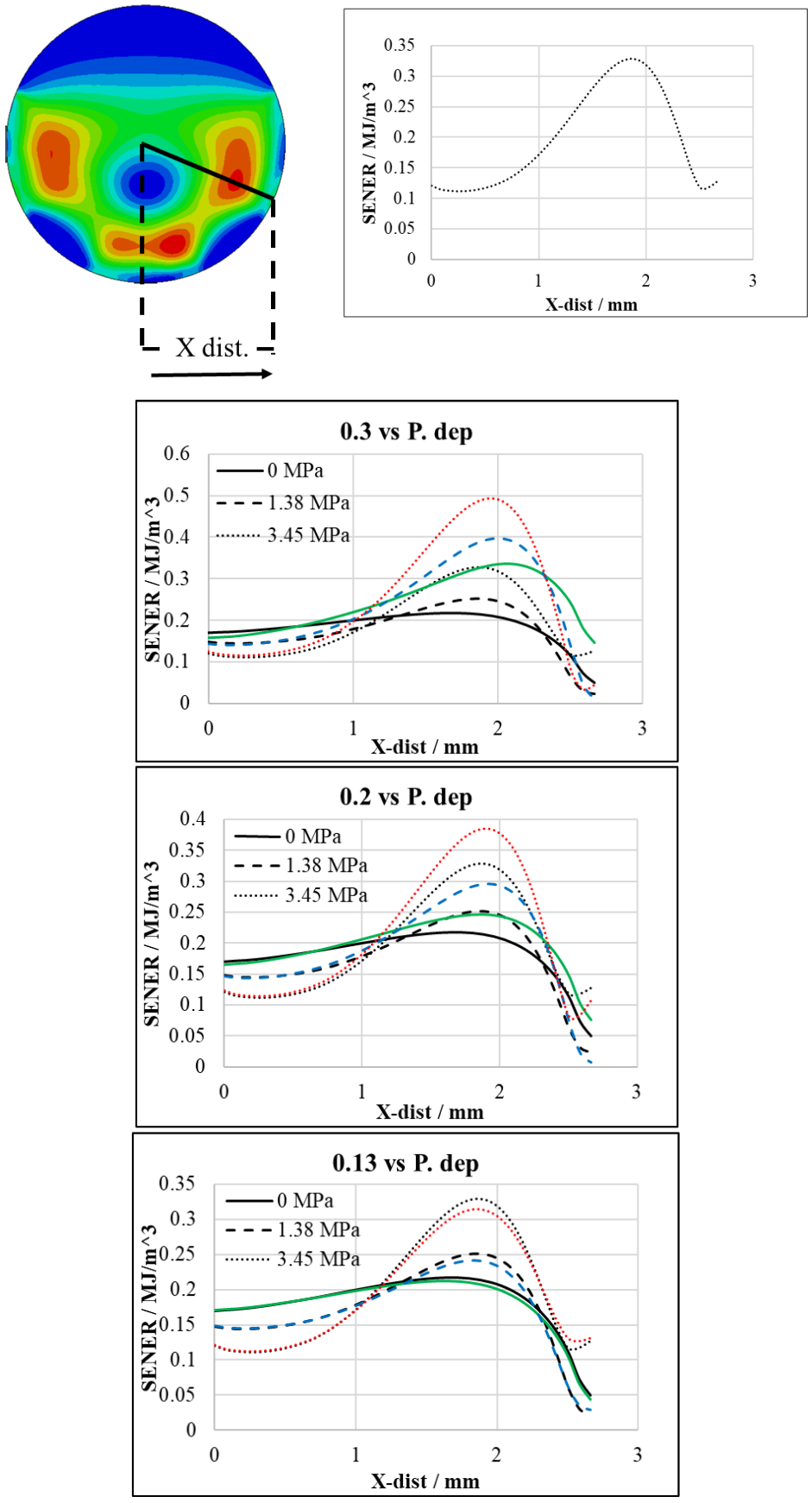

Fig. 6.6: Diagram showing the guideline across which SENER is measured from the FEA analysis (top); the angle and position of this line does not change across models or CoF changes. Comparison of strain energy response for different coefficients of friction compared to experimentally determined ones. Fixed coefficients are presented in colour and pressure dependent ones in black.

Unlike the contact pressure plots, the differences in strain energy density increase when the pressure increased. Not only does the magnitude increase, but the sharpness (or shape) of the curve does as well, indicating a higher concentration of strain energy near the extrusion gap of the gland by changing the friction models. A higher concentration of strain energy could be indicative of the origin of a crack. Once this strain energy reaches the maximum allowable that is observed in crack growth analysis of rubber[4] models would indicate failure of the material. If the coefficient of friction is overestimated, then one could also overestimate material failure, suggesting that strain energy concentration is higher than what it should be, this can cause over-engineering of the seals, along with increased costs when trying to increase compound mechanical properties or resistance to the environment.

One interesting aspect to the contact pressure analysis was how close the model was between the fixed coefficient of friction with a value of 0.13 taken from the plateau value of the pressure dependent function and the values obtained from the model using the full pressure dependent terms. Both lines are similar both in shape and value.

6.4 On the Changes of Shape During Setting

After observing the effects of inaccurate CoF of two non-tangential variables, it is clear how the study of contact interactions is key to obtaining key contour outputs for sealing rubber applications. It is also clear that if contact pressure, whether from mechanical response or fluid pressurisation, is well above the region when the CoF is highly pressure dependent, then a fixed model is realistic when it comes to the studied variables.

However, moments where the seal is not to be so heavily compressed, such as in seal setting and positioning might cause a greater difficulty to the designer. In these applications, the pressure dependent models have a much higher initial CoF than the typical fixed value models. To investigate this further, the setting of an S-shaped in low strain conditions (10%) was modelled, and changes observed in the shape with varying coefficients of friction. The reason for low strains is twofold; first, dynamic seals operate in a very small strain range in the industry (10-15%). Secondly, low strains have the highest disparity of frictional response when it comes to pressure dependent behaviours, making this model a worst-case scenario.

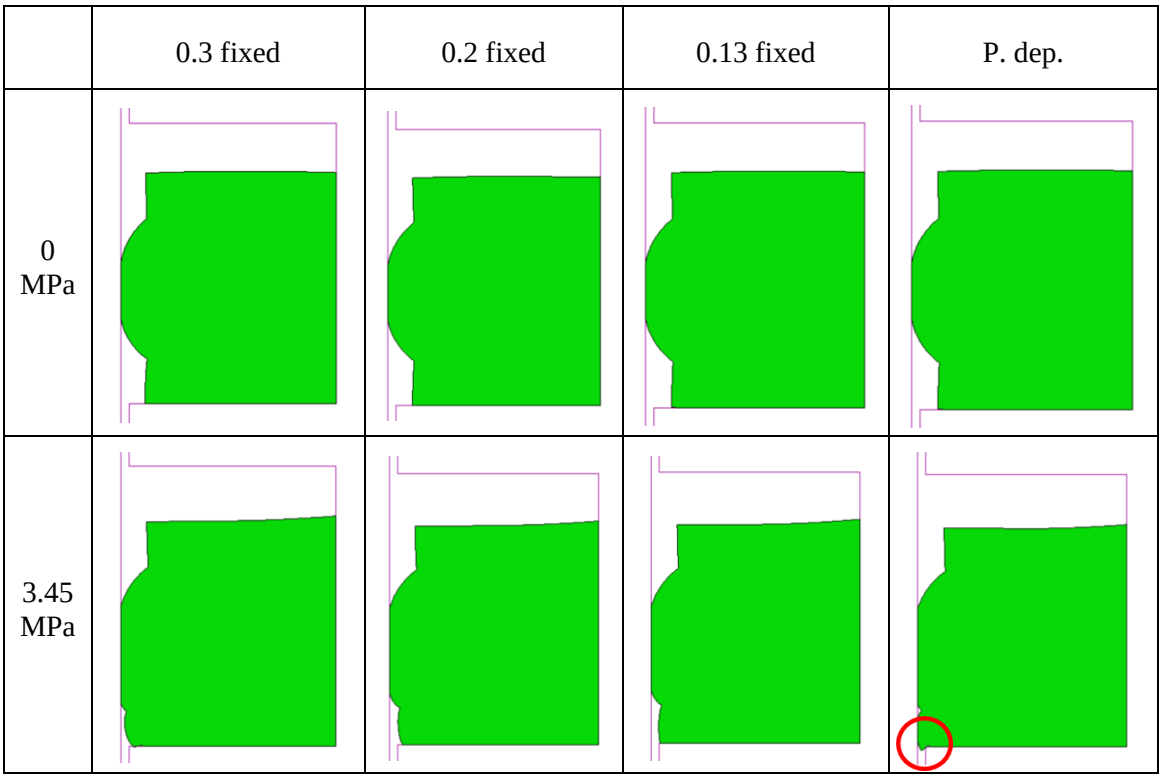

Fig. 6.7: S-shaped seal setting at different coefficients of friction and pressure levels. These are simply plots that allow the observation of the deformed shape of the seal itself. An HNBR 75 material model at 20°C was used to perform the FEA. Red circle shows possible extrusion place.

Figure 6.7 illustrates the changes in seal shape with changing pressure. The same FEA model for an HNBR 75 material was used for an S-shaped seal that is set by a downward sliding piston. If the seal is an axi-symmetric O-ring, there are no real significant effect resulting from rotational changes as the geometry is rotationally symmetric, unless the rotation is uneven around the symmetry of the seal and creates additional shear forces. When we use a seal that is not symmetrical across the Y axis, then significant changes in the deformed profile result can be observed.

During setting, the low-pressure levels cause the CoF to be greater for the pressure dependent model, generating extra drag downwards as the seal is set in place. With the additional drag at the start of the set, once the pressure is increased and frictional response drops, the sides in contact with the gland can slide more easily, causing the pressure dependent model to extrude in the bottom left corner. We notice that none of the fixed friction level other seals have this indication of extrusion. If a fixed coefficient of friction model were to be used here, the possible failure of the seal during setting would not be observed.

HNBR 75 was the only material used for these analyses, mainly for its propensity to failure, as shown in experiments. The purpose of these simulations is to observe possible effects of “standard” CoF settings for rubber materials, its disadvantages and pitfalls not commonly observed during simulation for seals during setting in the industry. Other

materials such as HNBR 90 and FKM 90, were not analysed in the same manner, since these extrusion failures were not present during testing and are not as likely and were not present for most of the tests. In no way is this a declaration that using imprecise CoF models is acceptable for harder materials, the intent is to direct attention to non-tangential forces analysis, and how they are affected by frictional behaviour.

A pressure-dependent coefficient of friction model is always desired. Computational or time limitations may not allow for full pressure dependent model applications. If the critical situation is the fully pressurised dynamic behaviour, a fixed CoF value could replace the pressure dependency as long as speed, lubrication and surface roughness are maintained, and higher-pressure conditions are the only ones that generate interest. But this can only be done if there is a previous characterisation of the material behaviour in its entirety (temperature, velocity, roughness and lubrication). So, although there are work arounds for modelling, there are no work arounds for characterisation.

6.5 Simulation Guidelines

Chapter 4 introduces how Abaqus/Standard modelling is used to analyse the stress response of a compressed seal. To do this analysis an axisymmetric O-ring 2D profile was used to model the elastomer seal between a sleeve gland and the piston that engages it. Once fully engaged and positioned, the seal was pressurised from the top and the force responses were analysed. For all the examples described in this section, a 90D (Shore A) HNBR material model is used. The Yeoh strain energy function coefficients are given in table 3.1 (temperature = 20°C). Although the Yeoh model provided a good fit to the uniaxial tension testing over a wide range of strain, in the limited small strain compression range of the seal (less than 13% compression) then a Neo-Hookean model could also be used.

All simulations performed in this research were comprised of three steps. The initial step allows the initial contact between the elastomer and the gland surface to be resolved without any of the bodies moving. The second step allows the central piston to engage with the seal and compresses it into the gland to form a seal. Finally, the third step introduces the fluid pressure using a penetration method between the O-ring and the gland to simulate fluid injection.

To constrain the rigid body motion of the free solid elastomer seal from bouncing off the analytical rigid surfaces that were used to model the piston and the sleeve, a node on the centre of the axisymmetric body of the elastomer was fixed in all directions for the initial step. Figure 6.8 shows the assigned master and slave surfaces used in each simulation. Analytical rigid surfaces can only be assigned master surface properties. The fixed point at the centre of the O-ring is also highlighted in the figure. For surface interaction properties, the entire circular cross section of the O-ring is the slave surface.

The surface contact properties required to represent the frictional interaction between two bodies can be found in the “tangential behaviour” section of the Abaqus software.

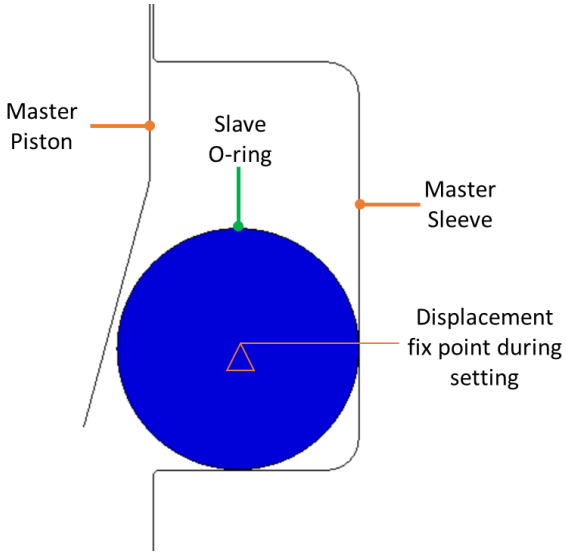

Figure 6.8: Initial conditions for surfaces (master/slave) for both the O-ring and the rigid sections of the rig. The fixed point in the centre of the O-ring helps maintain stability during the initial step contact resolution.

Figure 6.9 highlights the selection of the contact-pressure-dependent data. This could be further specialised by using temperature-dependent data as an alternative to simply changing the model for different temperature simulations. Field variable option is also available for this interaction. With field variables, users can define changes between steps for specific variables, this can also reduce the number of models required for testing.

With all surfaces described, the compression step takes place by holding the sleeve in place whilst lowering the piston. During this step, the velocity of the piston is not important as all the hysteretic and stress relaxation effects are neglected because we are only interested in the elastic response of the O-ring towards the piston in order to obtain the resulting normal forces.

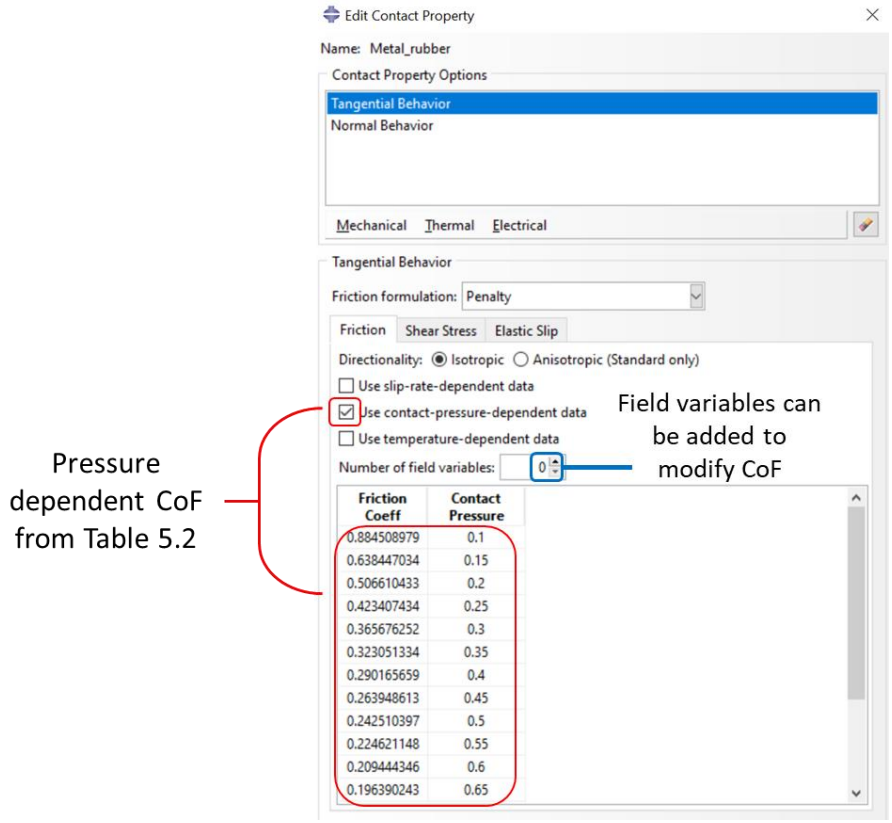

Figure 6.9: Contact property section of tangential behaviour between surfaces. Contact-pressure-dependent data showed the best results in all cases. Temperature dependency can be used to save time and field variables can be used to mark changes in temperature as steps progress.

Once the piston is engaged, Abaqus' fluid pressure penetration contact interface is used to simulate pressurisation of the seal. At this point, the only interest is to observe the mechanical changes in the seal, so all other fluid properties are ignored. Abaqus performs fluid pressure penetration between two contacting surfaces. Figure 6.10 highlights the surface selection, both for the slave and the master surface. Figure 6.11 shows the pressure interactions applied to these surfaces.

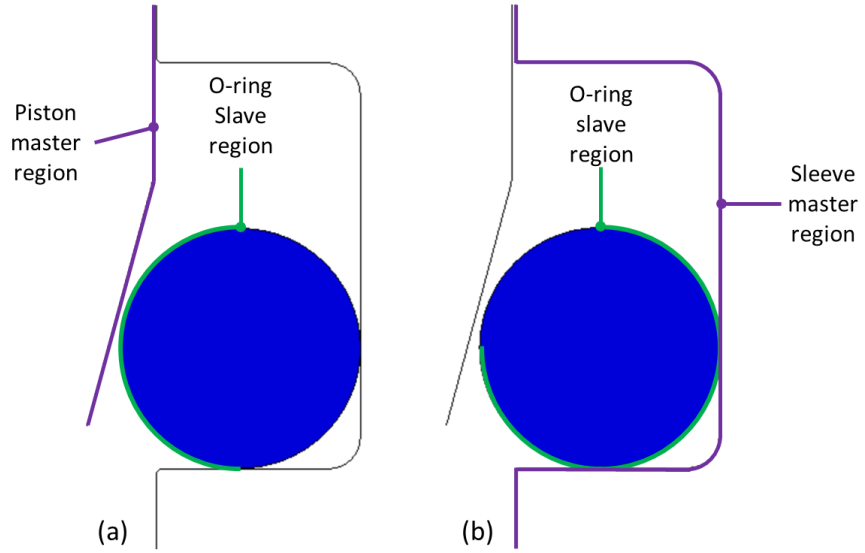

Figure 6.10: Surface selection for Pressure penetration method. Both slave surfaces share the same injection point.

Fluid injection occurs at the slave surface at a single point, then travels through the nodes until it encounters the master surface. At this point, the fluid is trapped, and the O-ring becomes pressurised. Because the fluid penetration surfaces do not overlap each other, the total fluid pressure is simply whatever is applied at each point, if they were to overlap, the pressure would have to be cut by half, to account for their pressure being applied twice.

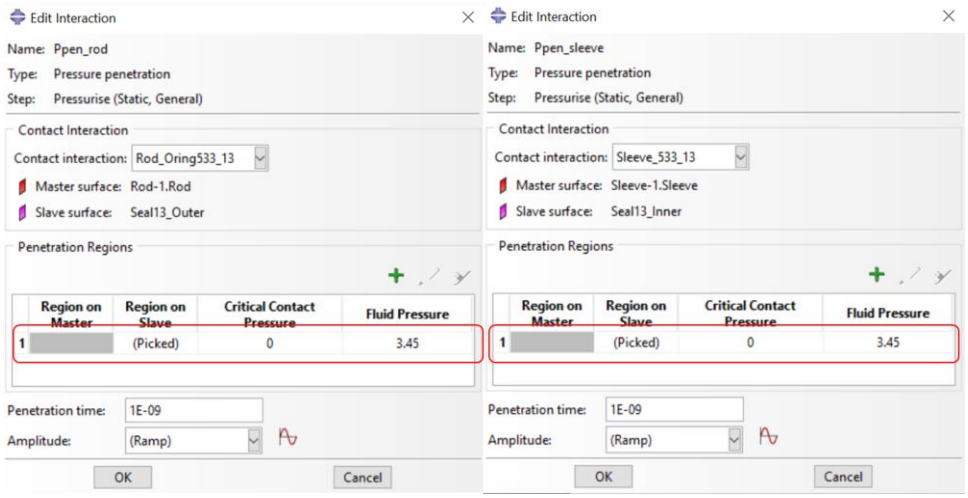

Figure 6.11: Pressure penetration parameters used in the experiments. Applied fluid pressure is 3.45 MPa (500 psi) on both halves of the seal.

Pressure penetration method can be used to check for seal failure, using a critical contact pressure where the node detaches from the surface if the fluid pressure becomes larger than the contact pressure. This feature was not used, because the analysis only needs to know the mechanical response to the fluid pressurisation.

After the step is finalised, the force response on the piston analytical surface is used as the normal force. Pressure profiles and strain energy density responses are all taken after the third step has finished.

7. Conclusions and Outlook

7.1 Frictional Theory

The understanding of rubber friction is a complicated matter, as there is no single variable that cause it to increase or decrease irrespective of secondary conditions, so statements such as “friction always increases with increasing temperature” need to be evaluated carefully. The competing factors of various contribution may cause the rubbers to maintain similar frictional behaviour under different conditions.

Observing and accounting for rubber frictional forces can be a complicated task when it comes to seals. As seals are commonly placed in tightly packed spaces, to replicate sealing environments whilst using measurement equipment can be a challenging endeavour. Even after obtaining the resulting drag forces from seal movement, and assuming that the entirety of drag comes from a friction contribution, the end result is simply the total friction that the seal undergoes.

Attempting to model what ratio of the total frictional forces comes from either the elastomer mechanical properties, the surface interaction, and the lubricant viscosity is undoubtedly the most complex part of rubber friction. The importance of understanding the contribution from each component is what allows engineers to design equipment and seals (especially dynamic ones) to either reduce or increase the friction. A reduction in friction might mean longer lifecycle for components, but it also means a reduced grip for example with tyres. The balancing of these two situations is what drove this investigation into rubber friction and all of its causes, to be examined again more carefully.

The most commonly known model for rubber friction contributions come from Persson[37] and Klüppel [35]. Both theories agree on the hysteretic effect that the internal friction comes from the filler network interactions. Couple the dynamic mechanical behaviour of the elastomer with the localised frequency of deformation, and both theories reach similar results, albeit their description of the local deformation might differ slightly due to the nature of surface analysis (PSD to HDC plus modified Greenwood and Williamson[88]).

When it comes to the adhesional component, there are several theories that attempt to describe it. Attempts to model the adhesional component the same way as crack propagation in viscoelastic solids has been suggested. Where the observation of a critical velocity (where shear forces reach a maximum) is what determines the peak of the adhesional component [39]. Even with the knowledge of crack growth behaviour in elastomers, experimental friction data is used to observe the critical velocity component. Other models simply look at the difference between wet and dry testing of frictional behaviour. The assumption on these ones is that the difference between the hysteretic model

is the entirety of the adhesional friction component[52]. But this one also requires the total frictional testing results in order to discriminate between the contributing factors.

The question “how can rubber friction be precisely determined without directly testing for it?” is commonly asked around the industry, whether it is from motorsport companies or from sealing engineers. It is an important question that, at its heart, tries to understand the physical principles that govern frictional behaviour and how it can be modified for specific applications. Chasing an answer for this question is the ultimate goal of understanding rubber friction, and a response to this question is always at the forefront of research for friction specialists.

It is proposed, that rubber modelling cannot be done without experimental testing of frictional behaviour. Dry friction could be determined by the latest of Klüppel’s [52] or Persson’s theories [41] for the hysteretic contribution. Adhesional friction can be determined by using different contact area samples and observing the difference between each sample. If the tests are carried out at slow velocities (< 1 mm/s) then wear and sample heat up would be negligible, eliminating two elements that can affect the measurements. Even in these cases, the surface might be covered by some of the rubber’s volatiles, lubricating it, and causing lower friction in subsequent tests. The use of virgin surface samples would also be positive for experimental solution of rubber friction determination.

Lubricants generate an extra layer of complexity; it is commonly thought that lubricants simply eliminate the adhesional component to friction. Whilst this is true to an extent, the lubricant itself generates a form of drag that comes from lubricant viscosity and can “change” the surface roughness by fully covering the micro-roughness scale. Currently, there are some modelling techniques [98] that could obtain the contribution of this fluid drag during lubricated motion.

The combination of dry testing, along with fluid mechanics simulation could solve the problem of rubber friction in a modelling complemented experimental way.

That being said, are there many other properties that do not have that same line of questioning. To hear “how can rubber uniaxial tension and compression behaviour be precisely determined without testing for it?” is extremely unlikely. Part of this is because there are many applications that require the strain energy density function to be determined, and the universality of uniaxial testing machines within universities and research laboratories. Although the response to the original question, of determining friction solely from physical parameters, is important, one must concede for the necessity of friction testing equipment under field conditions in order to better understand rubber components. The initial part of this thesis is dedicated to the development of this testing machinery.

7.2 Rig Design

A fully functional friction test methodology that works under hydrostatic pressure conditions was developed and validated. The necessity of the novel testing rig arose mainly from the requirement of high pressure testing under fully submerged conditions for O-ring seals. Although the testing methods has issues (as outlined in chapter 4) when it comes to setup, it is easily connected to standard Instron tension testing machines and fit within an oven. Handling the rig was also easily done, although a heavy setup, the actual change of seals and the quick connections, make it an experiment that could easily be taught to technicians. In terms of safety, the pressurised annulus was designed to hold less than 100 ml of fluid, in case there is any seal failure, so that any expelled volume would not be a grave danger to operators, and it would not have a major environmental impact.

Results were in accordance with that suggested from comparable data, where available, from the literature. This testing approach opens up several possibilities for characterising a wide range of behaviours and dependencies as the rig worked up to 35 MPa pressurisation and was able to operate at high temperatures as well. The pressure dependent behaviour known for decades was replicated here, indicating that the functioning principle of the rig (to observe, characterise and describe friction behaviour) was appropriate. Velocity dependent effects were also replicated similar to other data from the latest scientific literature, such as the low frequency adhesional max peak and the drop at the higher velocities which are still below the maximum viscous loss point. In terms of the surface effects acting on the seal's behaviour, since the surface profile was done on a piston instead of the sleeve for ease of analysis, various types of surface material and surface finish can be easily analysed by simply changing the piston. Surface roughness measurement adopted a measure that was more complicated than what is commonly used in the industry (Ra). An appropriate surface roughness and surface profile reading can help a great deal when it comes to predicting the effects of the dynamic mechanical properties of the elastomer. The effect of surface roughness for this particular set of experiments was marked by a difference in the horizontal dimension descriptor, instead of the more industry known vertical descriptor (Ra). Figures 5.13 and 5.14 show the effect of velocity when related to surface roughness in terms of local deformation rates. As the frequency increases (as is the case for shorter horizontal dimension value) the friction decreases as well, for all the samples studied.

O-ring size selected was an industry standard which means a wide range of different elastomer materials are available for further investigation as well. Not only does this allow relevant commercially available materials to be evaluated but also the large size of the seals makes it easy to install and test for equipment operators.

Overall, the design of the rig exceeded the initial expectations in terms of testing range,

for temperature and pressure; universality of connection with common Instron attachments; capability to provide seal friction drag data from a direct measurement; availability of various commercially available materials, and safety requirements in case of failures. The rig is now in possession of the sponsoring company who use it to perform friction testing data for their seal materials.

In terms of improvement for the rig, future designs should consider difficulties from this research such as:

- A direct measurement of the force values instead of using finite element analysis to resolve the normal load values. This could be done by means of pressurised paper of appropriate range. A flexible load cell that can cover the gland of the O-ring is also an acceptable option in terms of pressure mapping, this can then be used to further corroborate any FEA models that are tested.
- Place two more ports (above and below) the main pressure injection port. At the moment, the rig can only test for pressurised section-into-atmospheric pressure section. Differentially pressurised areas would give an even deeper understanding of seal interactions in practice. One could then compare a change of 10 MPa against atmosphere vs. 10 MPa against 20 MPa. These conditions are common in the field.
- Higher drain capacity to reduce the drag that lubrication passing through the top tube may generate in both directions. The calculations had the additional complication resulting from the drag calculation when the silicone oil was going through the pipes. Some frictional effects may have been hidden during that jump in vertical forces, larger cross section of fluid drain would reduce this additional contribution to the force and help speed up data processing.
- Thermocouple insertion points along the sleeve/glands can provide real time data of energy losses in the form of frictional heating, helping create a validation model for the hysteretic losses. This would also help with the preparation time for each test, since it marks the point where both the O-rings and the lubricant reach the desired test temperature.
- A replica of the rig could be done in hard, transparent epoxy to test for lower pressure levels, this would allow a direct measure of the nominal contact area to be made. The surfaces could even be modified to show the real contact area by colour maps if image recording software of sufficient quality was available.

7.3 Experiment Results

After analysis of all experiments and data collection, the opportunity to observe frictional behaviour at high pressure levels gives a better understanding of the validity of the current frictional theories that were originally designed around tyre friction. Initially, as tyre grip studies were the focus of rubber friction research, the concept of maximum penetration of rubber into the substrate as pressure levels got higher does not have a “threshold”. For high levels of pressure in submerged environments, this point where the contact area stops increasing with increasing pressure, was not determined. The quick drop in CoF with increasing pressure make it very clear that the adhesional component of friction simply does not increase noticeably with increasing pressure. This suggests that the

contribution from adhesional friction will reach a maximum at a certain level of pressure, using equation 53:

$$\mu_{adh}\left(\frac{A}{A_0}\right) = \begin{cases} \mu_{adh} = \frac{\tau_f}{p_0}\frac{A}{A_0}, \ \sigma < \sigma_{\max} \\ \mu_{adh} = c_A \times \mu_c, \ \sigma \geq \sigma_{\max} \end{cases} \quad (53)$$

Where σ_{max} is the threshold for pressure where the area stops increasing, μ_c is a maximum value of friction for the adhesional component, and c_a is a velocity dependent constant, just as equation 29. In fact, Eq. 29 can be modified to match this theory by simply adding the constant in the numerical fit and making the pressure dependant term an exponentially decaying factor.

Small changes in surface roughness can have a noticeable effect on the frictional behaviour of rubbers. Two polished steel surfaces, seemingly identical can produce different friction measurements, this can actually be accounted for by using profilometry and analysing rubber friction from a frequency point of view. Once the effects of horizontal dimensions are accounted for, or translated into frequency, the results from both pistons can be placed in a single figure and the trends are similar to literature results [41]. Although this is expected since the vertical dimensions remained the same for both pistons, to observe changes at such a small scale is further validation of the theories of rubber frictional behaviour in the adhesional zone.

7.4 Model Validation

With the output of the models evaluated under different conditions, it was clearly observed that a pressure dependent friction coefficient had different output results to all of the fixed coefficient ones. Even assuming that inaccuracy in tangential forces is the most obvious result of inadequate friction models, other variables are also affected.

The contact pressure of the seal against the surface must be greater than the fluid exerts on the seal, or otherwise there will be a leak. All fixed friction coefficients show an overestimation of the contact pressure, wrongly assuming a possible good seal where there might not be. Not only contact pressure is presented, but also strain energy. When fixed CoF models are used with the plateau region of the pressure dependent behaviour as their value, the contact pressure and strain energy outputs of the model, are almost identical to the pressure dependent ones. In terms of industry usage, this could simplify a lot of the calculations for elastomer seal friction behaviour. What should not be discarded is the possibility of failures during setting of seals, as extrusion and deformation of seals is a very real possibility.

For most seals, there will not be a complete disengagement from the surface, more like movement along it for dynamic seals. In the case of seals that do actually engage in this type of mechanical behaviour, then the setting phase is the most critical one. Most failures

that occurred during the experiments for this research, would be instantly noticeable if they occurred during setting. Figure 6.7 shows that even for the case of a fixed friction coefficient that matches the plateau region of the pressure dependent one, there is still a lower amount of deformation for the fixed one. Since during setting, there is a very low amount of pressure applied to the elastomer, the frictional forces are very large. If the seal's shape is directional in any way, high initial friction during setting can lead to high-strain conditions at the extrusion gap, which can lead to premature seal failure.

In ideal conditions, a pressure dependent coefficient must be used to satisfy the entire behaviour of the seal during setting and lifecycle. Chapter 6, however, outlines the possible "shortcuts" that can be taken which still allow for acceptable results in certain cases.

Overall, the research project presented in this thesis provided a better insight to frictional behaviour, not only from a research standpoint, but also an engineering one. Section 7.1 discusses the necessity for experimental testing in order to generate friction models, and chapter 6 speaks of the necessity to move away from the industry "standard" CoF values for rubber. This is the main industrial and engineering outlook that is projected from the work.

In terms of research and academic outcomes, the influence that lubricant properties play in rubber friction experiments. Some previous research simply assumes that lubricant eliminates adhesional contributions and nothing more. Very similar results were observed at high pressure and high temperature testing for all elastomers, indicating that even with different surface and mechanical properties, fluid drag contributes to a large portion of the frictional values. The viscous segment of the unified theory of rubber friction can be minimised with either high temperatures or low viscosity lubricant, but it sometimes is erroneously neglected. The author also made this mistake during the initial design of experiments of this work.

Finally in terms of material results, it was observed that: under lubricated conditions of smooth(polished) surfaces at high temperature and high pressure, the biggest modification to rubber friction behaviour is not elastomer type. The highest contributing factor is surface roughness and velocity. Elastomer properties come into play mostly as capacity to maintain seals without extrusion or crack initiation, this includes not only mechanical resistance, but also chemical and environmental resistance.

8. References

[1] Strobl, G.R., 1997. The physics of polymers (Vol. 2, p. 83). Berlin: Springer.

[2] Bower, D.I., 2003. An introduction to polymer physics.

[3] Hancock T., 1857. Personal Narrative of the Origin and Progress of the Caoutchouc or India-rubber Manufacture in England. Longman, Brown, Green, Longmans, & Roberts. London, UK.

[4] Windslow, R.J. 2018. Computational Modelling of Fracture Processes in Elastomeric Seals. PhD Thesis, Queen Mary University of London.

[5] Treloar, L.R.G., 2005. Physics of Rubber Elasticity (Oxford Classic Texts in the Physical Sciences). Oxford University Press.

[6] Bukhina, M.F. and Kurly and, S.K., 2007. Low-temperature behaviour of elastomers (Vol. 31). Brill.

[7] Young, R.J. and Lovell, P.A., 2011. Introduction to polymers. CRC press.

[8] Doolittle, A.K. and Doolittle, D.B., 1957. Studies in Newtonian flow. V. Further verification of the free‐space viscosity equation. Journal of applied physics, 28(8), pp.901-905.

[9] Cohen, M.H. and Turnbull, D., 1959. Molecular transport in liquids and glasses. The Journal of Chemical Physics, 31(5), pp.1164-1169.

[10] Williams, M.L., Landel, R.F. and Ferry, J.D., 1955. The temperature dependence of relaxation mechanisms in amorphous polymers and other glass-forming liquids. Journal of the American Chemical society, 77(14), pp.3701-3707.

[11] Plazek, D.J., Choy, I.C., Kelley, F.N., von Meerwali, E. and Su, L.J., 1983. Viscoelasticity and tearing energy of fluorinated hydrocarbon elastomers. Rubber chemistry and technology, 56(4), pp.866-882.

[12] Grosch, K.A., 1963. The relation between the friction and visco-elastic properties of rubber. Proceedings of the Royal Society of London. Series A. Mathematical and Physical Sciences, 274(1356), pp.21-39. [1]

[13] James, H.M. 1943. “Theory of the Elastic Properties of Rubber”. Journal of Chemical Physics, 11, 455.

[14] Flory, P.J. & J. Rehner, J. 1943. “Statistical Mechanics of Crosslinked Polymer Networks”. The Journal of Chemical Physics, 11 (11), 521.

[15] Treloar, L.R.G., 1943. “The Elasticity of a Network of Long-Chain Molecules. I.” Transactions of the Faraday Society, 39, 36-41.

[16] Kuhn, W. 1936. “Beziehungen zwischen Molekulgrosse, statistischer Molekulgestalt und elastischen Eigenschaften hochpolymerer Stoffe”. Kolloid-Zeitschrift.

[17] Rivlin, R.S. 1948. “Large Elastic Deformations of Isotropic Materials. I. Fundamental Concepts”. Philosophical Transactions of the Royal Society of London. Series A, Mathematical and Physical Sciences, 240 (822), 459-490.

[18] Yeoh, O.H. 1990. “Characterization of Elastic Properties of Carbon-Black-Filled Rubber Vulcanizates” Rubber Chemistry and Technology, 63 (5), 792-805.

[19] Kubo, M.T., Rojas, M.L., Miano, A.C. and Augusto, P.E., 2019. Rheological Properties of Tomato Products

[20] Mullins, L. 1950. “Thixotropic Behavior of Carbon Black in Rubber”. Journal of Physical and Colloid Chemistry, 54 (2), 239-251. (reprinted in Rubber Chem. & Tech., 23 (4), 733-743).

[21] Diani, J., Fayolle, B. and Gilormini, P., 2009. A review on the Mullins effect. European Polymer Journal, 45(3), pp.601-612.

[22] Payne, A.R. 1962. “The Dynamic Properties of Carbon Black Loaded Natural Rubber Vulcanizates. Part II”. Journal of Applied Polymer Science, 6 (21), 368-372. (reprinted in Rubber Chem. & Tech., 36 (2), 444-450).

[23] Wang, M.J., 1999. The role of filler networking in dynamic properties of filled rubber. Rubber

chemistry and technology, 72(2), pp.430-448.

[24] Roland, C.M., 2011. Viscoelastic Behavior of Rubbery Materials. OUP Oxford.

[25] Da Vinci, L., 1894. Codex atlanticus. Biblioteca Ambrosiana, Milan, 26(1).

[26] Coulomb, C.A., 1821. Théorie des machines simples en ayant égard au frottement de leurs parties et à la roideur des cordages. Bachelier.

[27] Smith, R.H., 2008. Analyzing friction in the design of rubber products and their paired surfaces. CRC press.

[28] Thirion, P., 1946. Les coefficients d'adherence du caoutchouc. Rev. Gene. Caout. Vol 23. pp 101-106.

[29] Schallamach, A., 1952. The load dependence of rubber friction. Proceedings of the Physical Society. Section B, 65(9): 657.

[30] Hertz, H., 1881. On the contact of elastic solids. Z. Reine Angew. Mathematik, 92, pp.156-171.

[31] Schallamach, A. 1963. Abrasion pattern on rubber, Rubber Chem. Technol. 63, 320-327

[32] Mullins, L., 1969. Softening of rubber by deformation. Rubber chemistry and technology, 42 (1), pp.339-362.

[33] Persson, B.N., 1998. On the theory of rubber friction. Surface science, 401(3): 445-454

[34] Gabriel P. 2010. Investigation and modelling of rubber friction. Queen Mary University of London.

[35] Klüppel, M. and Heinrich, G., 2000. Rubber friction on self-affine road tracks. Rubber chemistry and technology, 73(4), pp.578-606.

[36] Cugliari, J., 2021. Investigation of contact mechanics and friction of rubber compounds by experimental techniques and numerical simulations (Doctoral dissertation, Hannover: Institutionelles Repositorium der Leibniz Universität Hannover).

[37] Persson, B.N., 2001. Theory of rubber friction and contact mechanics. The Journal of Chemical Physics, 115(8), pp.3840-3861.

[38] Genovese, A., Farroni, F., Papangelo, A. and Ciavarella, M., 2019. A discussion on present theories of rubber friction, with particular reference to different possible choices of arbitrary roughness cutoff parameters. Lubricants, 7(10), p.85.

[39] Lorenz, B., Oh, Y.R., Nam, S.K., Jeon, S.H. and Persson, B.N.J., 2015. Rubber friction on road surfaces: Experiment and theory for low sliding speeds. The Journal of chemical physics, 142(19), p.194701.

[40] Persson, B.N.J. and Brener, E.A., 2005. Crack propagation in viscoelastic solids. Physical Review E, 71(3), p.036123.

[41] Tiwari, A., Miyashita, N., Espallargas, N. and Persson, B.N., 2018. Rubber friction: the contribution from the area of real contact. The Journal of chemical physics, 148(22), p.224701.

[42] Barquins, M., 1992. Adherence, friction and wear of rubber-like materials. Wear, 158(1-2), pp.87-117.

[43] Busse, L. «Investigation, Prediction and Control of Rubber Friction and Stick-Slip: Experiment, Simulation, Application,» Gottfried Wilhelm Leibniz Universitat Hannover, 2012 PhD Thesis.

[44] Milanese, E., Brink, T., Aghababaei, R. and Molinari, J.F., 2019. Emergence of self-affine surfaces during adhesive wear. Nature communications, 10(1), pp.1-9.

[45] Torbruegge, S. and Wies, B., 2015. Characterization of pavement texture by means of height difference correlation and relation to wet skid resistance. Journal of Traffic and Transportation Engineering (English edition), 2(2), pp.59-67

[46] Gredig, T., Silverstein, E.A. and Byrne, M.P., 2013. Height-height correlation function to determine grain size in iron phthalocyanine thin films. In Journal of Physics: Conference Series (Vol. 417, No. 1, p. 012069). IOP Publishing.

[47] Persson, B.N., Albohr, O., Tartaglino, U., Volokitin, A.I. and Tosatti, E., 2004. On the nature of surface roughness with application to contact mechanics, sealing, rubber friction and

adhesion. Journal of physics: Condensed matter, 17(1), p.R1.

[48] Parker O-ring Handbook, 2018.

[49] Galland, O. Holohan, E. van Wyk de Vries, B. and Burchardt, S. 2015 Laboratory modelling of volcano plumbing systems: a review. Advances in Volcanology. Springer Berlin Heidelberg. 1-68

[50] Hohenberger, T.W., Windslow, R.J., Pugno, N.M. and Busfield, J.J., 2019. A constitutive model for both low and high strain nonlinearities in highly filled elastomers and implementation with user-defined material subroutines in ABAQUS. Rubber Chemistry and Technology, 92(4), pp.653-686.

[51] Matsuda, K., Hashimoto, D. and Nakamura, K., 2016. Real contact area and friction property of rubber with two-dimensional regular wavy surface. Tribology International, 93, pp.523-529.

[52] Klüppel, M., Möwes, M.M., Lang, A., Plagge, J., Wunde, M., Fleck, F. and Karl, C.W., 2016. Characterization and application of graphene nanoplatelets in elastomers. Designing of Elastomer Nanocomposites: From Theory to Applications, pp.319-360.

[53] Carbone, G., Lorenz, B., Persson, B.N. and Wohlers, A., 2009. Contact mechanics and rubber friction for randomly rough surfaces with anisotropic statistical properties. The European Physical Journal E, 29(3), pp.275-284.

[54] Tiwari, A., Dorogin, L., Tahir, M., Stöckelhuber, K.W., Heinrich, G., Espallargas, N. and Persson, B.N., 2017. Rubber contact mechanics: adhesion, friction and leakage of seals. Soft Matter, 13(48), pp.9103-9121.

[55] Schallamach, A., 1952. The load dependence of rubber friction. Proceedings of the Physical Society. Section B, 65(9), p.657.

[56]https://www.parker.com/literature/O-Ring Division Literature/Static Files/frictionestimation.pdf

[57] Elmukashfi, E., 2021. An experimental method for estimating the tearing energy in rubber-like materials using the true stored energy.

[58] TW Hohenberger. 2022. Prediction of Leakage for High Pressures Elastomeric Seals. PhD thesis. Queen Mary University of London. London.

[59] Hohenberger, T. Lan, W. Jin, H. Pugno, N. & Busfield, J.J.C. 2020. “Numerical leak prediction of elastomeric seals”. In 25th International Conference on Fluid Sealing, Manchester, UK, March 4th–5th, 2020. Ed. A. Bickley. BHR Group, Bedfordshire, UK.

[60] Tolpekina, T.V. and Persson, B.N.J., 2019. Adhesion and friction for three tire tread compounds. Lubricants, 7(3), p.20.

[61] Tiwari, A., Tolpekina, T., Benthem, H.V., Gunnewiek, M.K. and Persson, B.N.J., 2021. Rubber adhesion and friction: role of surface energy and contamination films. Frontiers in Mechanical Engineering, p.114.

[62] Persson, B.N. and Scaraggi, M., 2014. Theory of adhesion: Role of surface roughness. The Journal of chemical physics, 141(12), p.124701.

[63] Dalvi, S., Gujrati, A., Khanal, S.R., Pastewka, L., Dhinojwala, A. and Jacobs, T.D., 2019. Linking energy loss in soft adhesion to surface roughness. Proceedings of the National Academy of Sciences, 116(51), pp.25484-25490.

[64] Tiwari, A., Miyashita, N. and Persson, B.N.J., 2021. Rubber Wear and the Role of Transfer Films on Rubber Friction on Hard Rough Substrates. Tribology letters, 69(2), pp.1-12.

[65] Clement, F., Bokobza, L. and Monnerie, L., 2005. Investigation of the Payne effect and its temperature dependence on silica-filled polydimethylsiloxane networks. Part I: Experimental results. Rubber chemistry and technology, 78(2), pp.211-231.

[66] Clément, F., Bokobza, L. and Monnerie, L., 2005. Investigation of the Payne effect and its temperature dependence on silica-filled polydimethylsiloxane networks. Part II: Test of quantitative models. Rubber chemistry and technology, 78(2), pp.232-244.

[67] Peterson, E.W., 2014. Tire-Road Friction Coefficient Estimation Using a Multi-scale, Physics-based Model (Doctoral dissertation, Virginia Tech).

[68] Jacobs, T.D., Junge, T. and Pastewka, L., 2017. Quantitative characterization of surface topography using spectral analysis. Surface Topography: Metrology and Properties, 5(1), p.013001.

[69] Pöschl, M., Vašina, M., Zádrapa, P., Měřínská, D. and Žaludek, M., 2020. Study of carbon black types in SBR rubber: Mechanical and vibration damping properties. Materials, 13(10), p.2394.

[70] Wagner, M.H., 1976. Analysis of time-dependent non-linear stress-growth data for shear and elongational flow of a low-density branched polyethylene melt. Rheologica Acta, 15(2), pp.136-142.

[71] Parker Hannafin Corp., 2021. "Selecting the Right O-Ring Seal Squeeze Ratio". http://blog.parker.com/selecting-the-right-o-ring-seal-squeeze-ratio. Accessed Sep. 18th, 2021.

[72] Smith, M 2009, ABAQUS/Standard User's Manual, Version 6.9. Dassault Systèmes Simulia Corp, Providence, RI.

[73] Lorenz, B.& Persson, B.N.J. 2010. "Leak rate of seals: Effective-medium theory and comparison with experiment". The European Physical Journal E, 31 (2), 159-167.

[74] Lorenz, B. & Persson, B.N.J. 2009. "Leak rate of seals: Comparison of theory with experiment". Europhysics Letters, 86 (4), 44006.

[75] Yanes, E.F. Busfield, J.J.C. Pugno, N. Manson, R. Chen, H.L. & Ramier, J. 2019. "Application of Rubber Friction to FEA Models of Rubber Sealing". In Constitutive Models for Rubber XI, Proceedings of the 11th European Conference on Constitutive Models for Rubber, Nantes, France, June 25-27, Eds: B. Huneau, J.-B. Le Cam, Y. Marco, & E. Verron. CRC Press, Boca Raton, Florida.

[76] Chandrasekaran, V.C., 2010. Rubber as a construction material for corrosion protection: a comprehensive guide for process equipment designers. John Wiley & Sons.

[77] Datta, R.N., 2002. Rubber curing systems (Vol. 12). iSmithers Rapra Publishing.

[78] Wolf, H., 1936. Rubber: a story of glory and greed (No. 678 W65).

[79] Lorenz, B., Persson, B.N.J., Fortunato, G., Giustiniano, M. and Baldoni, F., 2013. Rubber friction for tire tread compound on road surfaces. Journal of Physics: Condensed Matter, 25(9), p.095007.

[80] Tolpekina, T.V., Pyckhout-Hintzen, W. and Persson, B.N.J., 2019. Linear and nonlinear viscoelastic modulus of rubber. Lubricants, 7(3), p.22.

[81] De, S.K. and White, J.R. eds., 2001. Rubber technologist's handbook (Vol. 1). iSmithers Rapra Publishing.

[82] Mark, J.E., Erman, B. and Roland, M. eds., 2013. The science and technology of rubber. Academic press.

[83] Gent, A.N., 2012. Engineering with rubber: how to design rubber components. Carl Hanser Verlag GmbH Co KG.

[84] Gent, A.N., 1958. On the relation between indentation hardness and Young's modulus. Rubber Chemistry and Technology, 31(4), pp.896-906.

[85] Gent, A.N., 1964. Elastic stability of rubber compression springs. Journal of Mechanical Engineering Science, 6(4), pp.318-326.

[86] Gent, A.N. and Hamed, G.R., 1977. Peel mechanics of adhesive joints. Polymer Engineering & Science, 17(7), pp.462-466.

[87] Almqvist, A., Campana, C., Prodanov, N. and Persson, B.N.J., 2011. Interfacial separation between elastic solids with randomly rough surfaces: comparison between theory and numerical techniques. Journal of the Mechanics and Physics of Solids, 59(11), pp.2355-2369.

[88] Greenwood, J.A. and Williamson, J.P., 1966. Contact of nominally flat surfaces. Proceedings of the royal society of London. Series A. Mathematical and physical sciences, 295(1442), pp.300-319

[89] Gent, A.N., 1958. On the relation between indentation hardness and Young's modulus. Rubber Chemistry and Technology, 31(4), pp.896-906.

[90] Bird, J.O. and Chivers, P.J., 2014. Newnes engineering and physical science pocket book. Newnes.

[91] Moore., DF 1972. The Friction and Lubrication of Elastomers. DF Moore. Pergamon, Oxford. 1972. 288 pp.

[92] Le Gal, A. and Klüppel, M., 2007. Investigation and modelling of rubber stationary friction on rough surfaces. Journal of Physics: Condensed Matter, 20(1), p.015007.

[93] Kobatake, T., Kodama, K., Hayashi, S. and Yoshioka, A., 1997. Improvement of low-temperature flexibility of hydrogenated nitrile—butadiene rubber. *Rubber chemistry and technology*, *70*(5), pp.839-854.

[94] Severe, G. and White, J.L., 2002. Transition behavior of hydrogenated acrylonitrile-butadiene rubber. *Kautschuk Gummi Kunststoffe*, *55*(4), pp.144-144.

[95] Starkova, O. and Aniskevich, A., 2010. Poisson's ratio and the incompressibility relation for various strain measures with the example of a silica-filled SBR rubber in uniaxial tension tests. *Polymer Testing*, *29*(3), pp.310-318.

[96] Dapp, W.B., Lücke, A., Persson, B.N. and Müser, M.H., 2012. Self-affine elastic contacts: percolation and leakage. *Physical review letters*, *108*(24), p.244301.

[97] Putignano, C., Afferrante, L., Carbone, G. and Demelio, G.P., 2013. A multiscale analysis of elastic contacts and percolation threshold for numerically generated and real rough surfaces. *Tribology International*, *64*, pp.148-154.

[98] Vakis, A.I., Yastrebov, V.A., Scheibert, J., Nicola, L., Dini, D., Minfray, C., Almqvist, A., Paggi, M., Lee, S., Limbert, G. and Molinari, J.F., 2018. Modeling and simulation in tribology across scales: An overview. *Tribology International*, *125*, pp.169-199.

[99] Putignano, C., Carbone, G. and Dini, D., 2015. Mechanics of rough contacts in elastic and viscoelastic thin layers. *International Journal of Solids and Structures*, *69*, pp.507-517.

[100] Putignano, C., Reddyhoff, T. and Dini, D., 2016. The influence of temperature on viscoelastic friction properties. *Tribology International*, *100*, pp.338-343.

[101] Whitehouse, D.J. and Archard, J.F., 1970. The properties of random surfaces of significance in their contact. *Proceedings of the Royal Society of London. A. Mathematical and Physical Sciences*, *316*(1524), pp.97-121.

Appendix A: An HDC Matlab Code

```
function HDC(A)
%HDC = Height Difference Correlation Function
%   This function will take the difference of squares between 2 points
%   of the raw profilometry data. It will average the difference using
%   one size of horizontal separation, then it will increase that
%   separation and do it again, until a maximum horizontal value is
%   achieved.
i=1;x=1;j=i; % just simple counters to loop matrix position
d=1.25;  % d is the horizontal sampling of the profilometer, in this case
            % it is 1.25 um.
matsize = size(A); % Now we detect the total size of the matrix to see
                % how big a counter we need.
C=zeros(size(A));
s=matsize(1,1);
for j=1:10
for x=1:s-1
for c=1:s-x
B(c,j) = (A(c+x,j)-A(c,j))^2; % actual HDC operation occurs here.
%B=transpose(B);        % Matlab by default uses rows instead of columns
end                    % columns are easier to visualise.

d=x*0.00000635;         % here we increment the horizontal position by
                    % one unit.
C(i,j)=mean(B(:,j));    % the C matrix is the resulting matrix, with the
C(i,2)=d;               % mean of the HDC on column 1, and lambda on 2.
i=i+1;
end
end
N = zeros(matsize(1,1),1);
N = C(:,1);
M = movmean(N,2);       % smoothing line
n = C(:,2);
N = C(:,1);
plot(n,M);
title('Height difference correlation function')
ylabel('HDC (\lambda) / mm^{2}')
xlabel('\lambda / \mum ')
set(gca, 'YScale', 'log')  %changing to log scale
set(gca, 'XScale', 'log')
end
```